Buckling of Conical-Cylindrical Shells in Launch-Vehicle Applications

Rudd, M.T.

DOI
10.4233/uuid:3d624499-7557-44f7-8b41-f347c69fbc93

Publication date
2026

Document Version
Final published version

Citation (APA)
Rudd, M. T. (2026). *Buckling of Conical-Cylindrical Shells in Launch-Vehicle Applications*. [Dissertation (TU Delft), Delft University of Technology]. https://doi.org/10.4233/uuid:3d624499-7557-44f7-8b41-f347c69fbc93

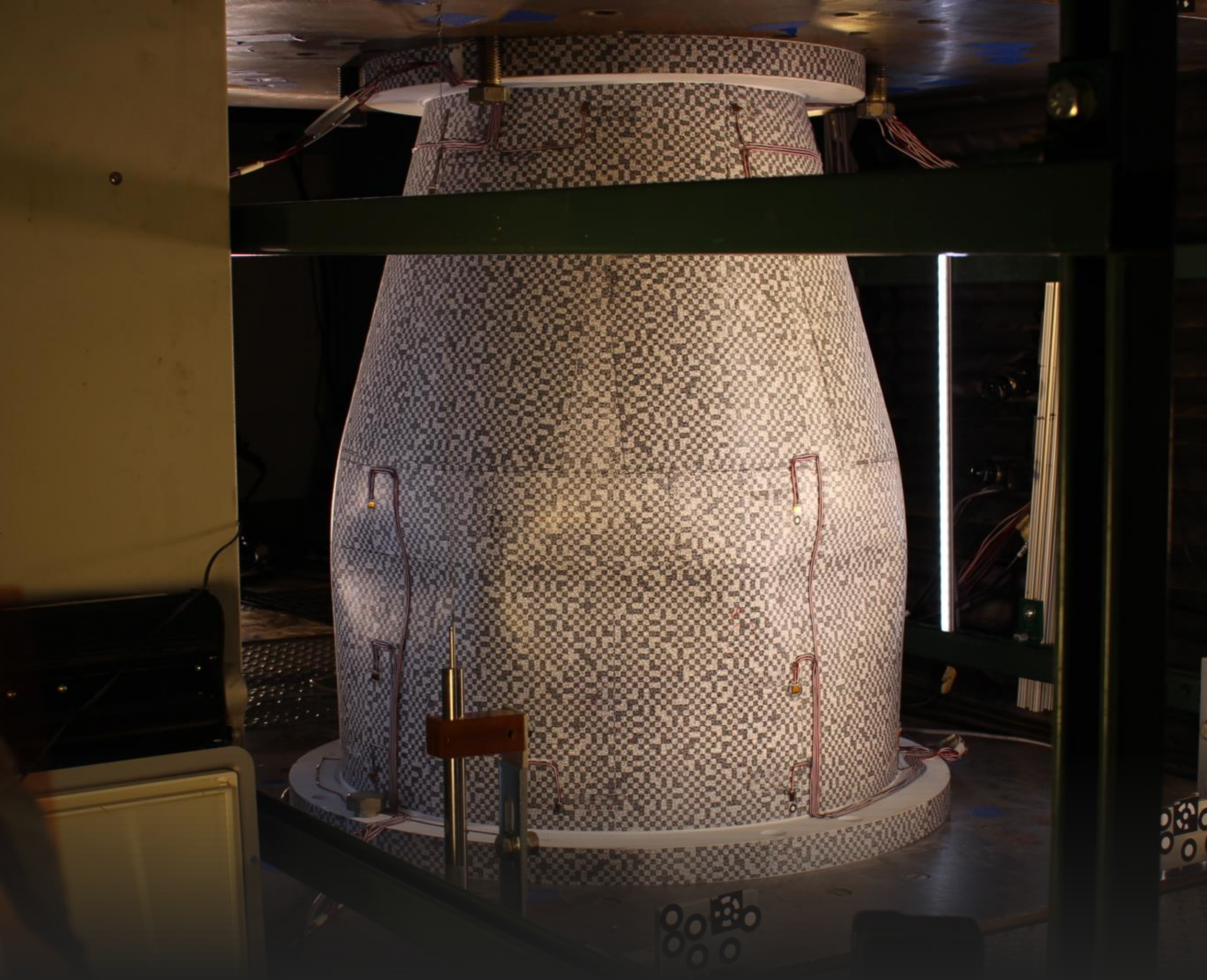

BUCKLING OF CONICAL-CYLINDRICAL SHELLS IN LAUNCH-VEHICLE APPLICATIONS

MICHELLE TILLOTSON RUDD

BUCKLING OF CONICAL-CYLINDRICAL SHELLS IN LAUNCH-VEHICLE APPLICATIONS

BUCKLING OF CONICAL-CYLINDRICAL SHELLS IN LAUNCH-VEHICLE APPLICATIONS

Dissertation

for the purpose of obtaining the degree of doctor
at Delft University of Technology
by the authority of the Rector Magnificus Prof. dr. ir. T. H. J. J. van der Hagen
chair of the Board for Doctorates,
to be defended publicly on
Monday 26 January 2026 at 15:00 o'clock

by

Michelle Tillotson RUDD

Masters of Engineering in Structural Engineering,
Lehigh University, Bethlehem, Pennsylvania, United States
born in Midland, Michigan, United States.

This dissertation has been approved by the promotors.

Composition of the doctoral committee:

Rector Magnificus,	Chairperson
Prof. dr. C. Bisagni,	Delft University of Technology, *promotor*
Dr. S. Turteltaub,	Delft University of Technology, *promotor*
Independent members:	
Prof. dr. -Ing. R. Degenhardt,	University of Bremen / DLR, Germany
Prof. dr. C.A. Featherston,	Cardiff University, United Kingdom
Prof. dr. .ir M. Langelaar,	Delft University of Technology
Prof. dr. .ir F.C. Vossepoel,	Delft University of Technology
Dr. B. Giovanardi,	Delft University of Technology, *reserve member*
Other member:	
Dr. M.R. Schultz,	NASA Langley Research Center

Keywords: Buckling, conical-cylindrical shells, thin-walled, composite, finite element modeling, imperfections, experimental, launch vehicles, knockdown factors, sensitivity analysis, polynomial chaos expansion

Printed by:

Front & Back:

ISBN 000-00-0000-000-0

In memory of Jeffery P. Norris.

CONTENTS

LIST OF FIGURES

LIST OF TABLES

SUMMARY

LAUNCH VEHICLES and payload adapters are mainly composed of thin-walled cylindrical shells and conical shells, where conical shells are necessary when transitioning from a larger to a small diameter. These thin-walled shell structures are constructed with metallic or composite materials. Mass is a critical factor in the design and operation of launch vehicles, so it is desirable to save as much mass as possible on primary (core stage, interstage) and secondary structures (payload adapters). This objective can be achieved by maximizing the radius-to-thickness ratio in conical and cylindrical shell structures. However, structures with high radius-to-thickness ratios are usually more susceptible to buckling failure. Traditionally, conical and cylindrical shells are designed and analyzed as independent structures. State-of-the-art manufacturing and numerical methods also allow designers to consider novel shapes and joints to save mass and increase volume, for example, combining the conical and cylindrical shells in a single integrated structure. By combining these two sections with a seamless toroidal transition, designers can remove the heavy, stiff interface ring that often connects the two independent structures, which potentially saves mass. An example of this type of integrated structure is the NASA Universal Stage Adapter.

Demonstrating the ability to successfully predict the buckling behavior of integrated conical-cylindrical shells is a critical step in the development of buckling design guidelines for this class of structures. Although there are numerous papers documenting the test and analysis correlation of conical and cylindrical shells separately, there is a limited number of research papers specifically related to the test and analysis of an integrated conical-cylindrical shell under axial compression. Furthermore, a modeling methodology has yet to be proven to predict the buckling behavior of these integrated shell structures.

To address this need, a buckling analysis methodology was developed which successfully predicted the buckling behavior of a composite cylindrical shell with a non-traditional composite layup. The methodology was further applied to an integrated conical-cylindrical composite shell. The finite element model included as-built geometric imperfections and thickness variations, and a geometrically nonlinear analysis was used to predict the buckling behavior for both the cylindrical and the conical-cylindrical shells. A composite conical-cylindrical shell was designed, built, and tested until buckling. The observed buckling behavior was in good agreement with the predicted behavior. Since the test specimen buckled elastically, it could be reused for further testing. The specimen was modified with additional composite plies that were added to the transition region. The same finite element modeling approach was also used to successfully predict the buckling of the composite conical-cylindrical shell with the modified design. This additional test provided further validation of the modeling methodology.

After validation, the modeling methodology was used to investigate whether the current buckling design methodology for conical and cylindrical shells can be applied to integrated conical-cylindrical shells. This begins with comparing the buckling response of conical and cylindrical shells, and how they compare with the buckling response of an integrated conical-cylindrical shell using an eigenvalue analysis (buckling equation) and a geometrically nonlinear analysis (implicit quasi-static analysis). The buckling behavior and imperfection sensitivity of the conical-cylindrical shell was used to assess the traditional buckling design methodology. It was determined that the traditionally recommended knockdown factors may not be conservative for conical-cylindrical shells in some cases. It was also discovered that the effects of geometrical nonlinearity may be more influential than imperfections for conical-cylindrical shells, which is contrary to the case of the individual components.

To help quantify the relative importance of various design parameters, a Polynomial Chaos Expansion was employed to express the critical buckling load of a conical-cylindrical shell as a function of the shell thicknesses, cone angles, transition geometry and axial stiffness. Polynomial Chaos Expansion was also used to highlight differences in the predicted buckling loads obtained from a buckling eigenvalue analysis and a geometrically nonlinear implicit dynamics analysis. Isotropic and composite shells were considered separately. Due to its capacity to successfully predict the buckling load of a conical-cylindrical shell, the Polynomial Chaos Expansion of the buckling load may be a useful design tool during launch vehicle sizing studies, as it may limit the number of finite element analyses required, particularly in the early design stages.

This research aimed to present the fundamental buckling behavior of conical-cylindrical shells through numerical and experimental means. This led to the conclusion that the traditional buckling design approach for cone and cylinders is not appropriate for conical-cylindrical shells. Additionally, it may be more mass efficient to design a conical-cylindrical shell that has a lower buckling capability because it is less sensitive to imperfections. The recommendations provided are based on experimentally validated data and observations, which provides credibility to the conclusions and recommendations.

SAMENVATTING

Lanceervoertuigen en ladingadapters bestaan voornamelijk uit cilindrische en conische dunwandige constructies. Deze dunwandige constructies zijn gemaakt van metalen of composietmaterialen, en conische constructies zijn nodig bij de overgang van een grotere naar een kleinere diameter. Massa is een kritische factor in het ontwerp en de werking van lanceervoertuigen, dus het is wenselijk om zoveel mogelijk massa te besparen op primaire (kernfase, tussenfase) en secundaire constructies (ladingadapters). Dit doel kan worden bereikt door de straal-tot-dikteverhouding in conische en cilindrische constructies te maximaliseren. Constructies met een hoge straal-tot-dikteverhouding zijn echter meestal gevoeliger voor knikfalen. Traditioneel worden conische en cilindrische dunwandige constructies ontworpen en geanalyseerd als onafhankelijke delen. State-of-the-art productie- en numerieke methoden stellen ontwerpers ook in staat om nieuwe vormen en verbindingen te overwegen om massa te besparen en volume te vergroten, bijvoorbeeld door de conische en cilindrische constructies in één geïntegreerde constructie te combineren. Door deze twee secties te combineren met een naadloze toroïdale overgang, kunnen ontwerpers de zware, stijve interface-ring verwijderen die vaak de twee onafhankelijke delen verbindt, wat mogelijk massa bespaart. Een voorbeeld van dit type geïntegreerde constructie is de NASA "Universal Stage Adapter".

Het aantonen van het vermogen om het knikgedrag van geïntegreerde conisch-cilindrische dunwandige constructies succesvol te voorspellen, is een cruciale stap in de ontwikkeling van knikontwerprichtlijnen voor deze klasse constructies. Hoewel er talloze artikelen zijn die de test- en analysecorrelatie van conische en cilindrische dunwandige constructies afzonderlijk documenteren, is er een beperkt aantal onderzoeksartikelen die specifiek betrekking hebben op de test en analyse van een geïntegreerde conisch-cilindrische dunwandige constructies onder axiale compressie. Bovendien moet er nog een modelleringsmethodologie worden bewezen om het knikgedrag van deze geïntegreerde dunwandige constructies te voorspellen.

Om aan deze behoefte te voldoen, werd een knikanalysemethodologie ontwikkeld die het knikgedrag van een samengestelde cilindrische dunwandige constructie met een niet-traditionele composietlay-up succesvol voorspelde. De methodologie werd verder toegepast op een geïntegreerde conisch-cilindrische samengestelde dunwandige constructie. Het eindige-elementenmodel omvatte äs-built"geometrische imperfecties en diktevariaties, en een geometrisch niet-lineaire analyse werd gebruikt om het knikgedrag voor zowel de cilindrische als de conisch-cilindrische dunwandige constructies te voorspellen. De samengestelde conisch-cilindrische dunwandige constructie werd getest tot knik, en het waargenomen knikgedrag kwam goed overeen met het voorspelde gedrag. Omdat het testmonster elastisch knikte, kon het worden hergebruikt voor verdere tests. Een aangepast monster werd gemaakt met extra composietlagen die werden toegevoegd aan het overgangsgebied. Dezelfde eindige-elementenmodelleringsaanpak voorspelde ook succesvol het knikken van de samengestelde conisch-cilindrische dunwandige con-

structie met het aangepaste ontwerp. Deze aanvullende test zorgde voor verdere validatie van de modelleringsmethodologie.

Na validatie werd de modelleringsmethodologie gebruikt om te onderzoeken of de huidige knikontwerpmethodologie voor conische en cilindrische dunwandige constructies kan worden toegepast op geïntegreerde conisch-cilindrische dunwandige constructies. Dit begint met het vergelijken van de knikrespons van een conische en een cilindrische dunwandige constructie, en hoe deze zich verhoudt tot de knikrespons van een geïntegreerde conisch-cilindrische dunwandige constructie met behulp van een eigenwaardeanalyse (knikvergelijking) en een geometrisch niet-lineaire analyse (impliciete quasi-statische analyse). Het knikgedrag en de imperfectiegevoeligheid van de conisch-cilindrische dunwandige constructie werden gebruikt om de traditionele knikontwerpmethodologie te beoordelen. Er werd vastgesteld dat de traditioneel aanbevolen knockdownfactoren in sommige gevallen mogelijk niet conservatief zijn voor conisch-cilindrische dunwandige constructies. Er werd ook ontdekt dat de effecten van geometrische niet-lineariteit invloedrijker kunnen zijn dan imperfecties voor conisch-cilindrische dunwandige constructies, wat in strijd is met het geval van de individuele componenten.

Om het relatieve belang van verschillende ontwerpparameters te helpen kwantificeren, werd een zogenaamde "Polynomial Chaos Expansion"(polynomiale chaos-expansie) gebruikt om de kritische knikbelasting van een conisch-cilindrische dunwandige constructie uit te drukken als een functie van de schaaldiktes, kegelhoeken, overgangsgeometrie en wapeningsniveaus. Polynomiale chaos-expansie werd ook gebruikt om verschillen in de voorspelde knikbelastingen te benadrukken die werden verkregen uit een knikeigenwaardeanalyse en een geometrisch niet-lineaire impliciete dynamische analyse. Isotrope en samengestelde dunwandige constructies werden afzonderlijk beschouwd. Vanwege het vermogen om de knikbelasting van een conisch-cilindrische dunwandige constructie succesvol te voorspellen, kan de polynomiale chaos-expansie van de knikbelasting een nuttig ontwerpinstrument zijn tijdens de dimensioneringsstudies van lanceervoertuigen, omdat het het aantal vereiste eindige-elementenanalyses kan beperken, met name in de vroege ontwerpfasen.

Dit onderzoek had als doel het fundamentele knikgedrag van conisch-cilindrische dunwandige constructies te presenteren door middel van numerieke en experimentele methoden. Dit leidde tot de conclusie dat de traditionele knikontwerpbenadering voor kegels en cilinders niet geschikt is voor conisch-cilindrische dunwandige constructies. Bovendien kan het massa-efficiënter zijn om een conisch-cilindrische dunwandige constructie te ontwerpen die een lager knikvermogen heeft, omdat deze minder gevoelig is voor onvolkomenheden. De verstrekte aanbevelingen zijn gebaseerd op experimenteel gevalideerde gegevens en observaties, wat geloofwaardigheid verleent aan de conclusies en aanbevelingen.

1

INTRODUCTION

LAUNCH vehicles and payload adapters are mainly composed of thin-walled cylindrical shells and conical shells. Cylindrical shells are quite common for primary launch vehicle structures, such as the core stage on NASA's Space Launch System, and conical shells can be used when transitioning from a larger diameter to a smaller diameter, such as the Launch Vehicle Stage Adapter (Figure 1.1). Mass is a premium resource on launch vehicles, so it is desirable to save as much mass on primary (core stage, interstage) and secondary structures (payload adapters) by optimizing the radius-to-thickness ratio. Therefore, these structures usually have high radius-to-thickness ratios, which make them more susceptible to buckling.

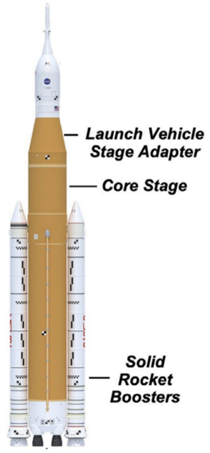

Figure 1.1: The NASA Space Launch System Block 1 Configuration.[1]

State-of-the-art manufacturing and numerical methods also allow designers to consider more nontraditional shapes to save mass and increase volume, for example, combining the conical and cylindrical shells in a single unitized structure. By combining these two sections with a seamless toroidal transition, designers can remove the heavy, stiff interface ring that often connects the two independent structures, which potentially saves mass. An example of this type of combined structure is the NASA Universal Stage Adapter[2], Figure 1.2, and the Système de Lancement Double Ariane (Sylda) on the Ariane 5 and the Vega Secondary Payload Adapter [3].

Figure 1.2: The NASA Universal Stage Adapter in the test stand at Marshall Space Flight Center. [4]

1.1. MANUFACTURING COMPOSITE STRUCTURES USING AUTOMATED FIBER PLACEMENT

Composite material systems (unidirectional fibers and fabric) and manufacturing methods, such as automated fiber placement, have enabled the construction of launch vehicle structures with doubly curved components such as a conical-cylindrical shell with a toroidal transition and ogive payload fairings. Fabricating these structures generally involves laying down composite plies on the surface of a mandrel that matches the contour of the final piece of hardware. An example of automated fiber placement (AFP) is shown in Figure 1.3. Figure 1.3a shows a detailed view of the robot head and identifies the spools of preimpregnated carbon fiber unidirectional tape. The tape is preimpregnated with a resin system which is then fed into the roller. The specified number of plies fed through the roller is referred to as a course. The heater warms up the tape to increase the tackiness to ensure better adhesion to the tool surface. Figure 1.3b shows the AFP robot laying the first facesheet ply on a cylindrical 2.4-m-diameter mandrel. The robot can be programmed to maintain a constant fiber angle along a doubly curved or conical section. The commercial software used to program the robot also allows the operator to specify the amount of ply overlap between adjacent courses.

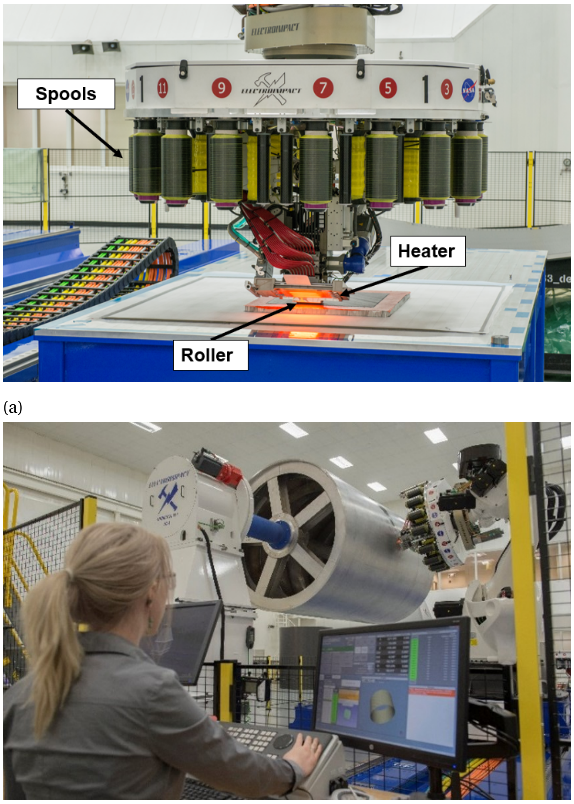

(a)

(b)

Figure 1.3: Automated Fiber Placement Robot at Marshall Space Flight Center: a) Detailed view of the robot head; b) laying the first ply on a cylindrical mandrel.

1.2. TRADITIONAL BUCKLING DESIGN APPROACH FOR LAUNCH-VEHICLE SHELL STRUCTURES

In the traditional design of launch-vehicle shell structures, the buckling capability is determined by multiplying the critical buckling load, as obtained from a linear eigenvalue analysis, by a knockdown factor. Buckling knockdown factor (KDF) recommendations for cylindrical and conical shells are published in NASA SP-8007 and NASA SP-8019, respectively, which were published in the late 1960s. At the time, the buckling load was determined using closed-form solutions or a simplistic numerical model. The knockdown factor is used to account for the differences between the experimental buckling load and the calculated linear eigenvalue. For cylindrical and conical shells, the difference between the linear eigenvalue and the tested value is largely attributable to geometric imperfections.

State-of-the-art technology has enabled engineers to develop a methodology to predict the buckling behavior of conical and cylindrical shell structures using finite element analyses that agree well with experimental results. For example, the as-built state of the shell structure can be measured using photogrammetric techniques. The details that define the as-built state include reference-surface geometric imperfection and thickness variations. The measured geometric imperfections and thickness variations can be incorporated into a finite element model. Additionally, the numerical methods in finite element commercial software enable high-fidelity analyses that include the large displacements and rotations that occur during a buckling failure. Incorporating as-built measurements in a geometrically nonlinear finite element analysis has also been used to demonstrate the over-conservativeness of the traditional buckling guidelines. However, there is little research on the buckling of conical-cylindrical shells, and, therefore, there are no buckling design recommendations for combined conical-cylindrical shells with a toroidal transition even though they are currently being utilized by the aerospace industry.

1.3. RESEARCH OBJECTIVE

The aim of this research is to provide buckling design recommendations for conical-cylindrical shells for launch-vehicle applications. At least two main criteria must be met before design guidance can be recommended. The first is to demonstrate the ability to successfully predict the buckling behavior of conical-cylindrical shells. The validated modeling methodology to predict the buckling behavior of a composite cylindrical shell with a nontraditional layup will be presented and leveraged to predict the buckling of a composite conical-cylindrical shell with and without reinforcement plies in the transition region. The second criterion is to determine whether the current buckling design methodology for conical and cylindrical shells can be applied to conical-cylindrical shells. The validity of using the buckling load (obtained as a linear eigenvalue) multiplied by a recommended knockdown factor from NASA-SP-8007 or NASA-SP-8019 needs to be assessed. To achieve these objectives the primary factors including geometric, design, and analysis methods that affect the buckling behavior and imperfection sensitivity must be understood.

1.4. THESIS OUTLINE

Each chapter presents information pertinent to the main research objective of providing buckling design guidance for conical-cylindrical shells for launch vehicle applications. Each chapter is derived from a published journal publication or is planned to be submitted to a journal, and can be read as a stand-alone document. A literature review is presented in each chapter and references are listed at the end of the thesis in bibliography. Since each chapter is self-standing, important information may be repeated between chapters. A description of the chapters and how they relate to the overall research objective is listed below.

- *Chapter 2* discusses the validated modeling methodology used to predict the buckling behavior of a composite cylindrical shell with a nontraditional layup. The cylindrical shell has been studied in depth, and the modeling methodology has been well documented to accurately predict the buckling response. The details of the finite element model included as-built geometric imperfections and thickness variations, and a geometrically nonlinear analysis was used to predict the buckling behavior. The test setup is described, followed by a comparison between the test data and finite element analysis. A similar modeling approach is to be leveraged to predict the buckling behavior of conical-cylindrical shells.

- *Chapter 3* begins with a numerical investigation comparing the buckling behavior of a conical shell and cylindrical shell, and how it compares with the buckling response of a conical-cylindrical shell. The buckling response and imperfection sensitivity of the conical-cylindrical shell is investigated and the relevance of the traditional buckling design methodology using NASA SP-8007 and 8019 is assessed [5, 6]. The numerical analyses led to the design of a composite conical-cylindrical shell test article to fail in buckling, called 3CHELL (Composite Conical Cylindrical Shell). Using a similar modeling methodology as described for the composite cylinder in Chapter 2, a finite element model that included geometric imperfections and thickness variations was created. The test setup and results are presented, along with a presentation of the test data versus the analysis data.

- *Chapter 4* introduces the effects of adding reinforcement plies to the transition region of a composite conical-cylindrical shell and how it can change the buckling behavior as well as imperfection sensitivity with numerical analyses. The numerical analyses presented interesting results which led to a design modification of 3CHELL. Reinforcement plies were added to the transition region of 3CHELL and was referred to as Re3CHELL (Reinforced Composite Conical Cylindrical Shell). The composite test article Re3CHELL was tested to help validate the modeling methodology for conical-cylindrical shells, but also to confirm the findings from the numerical analyses. A direct comparison was made on buckling behavior between 3CHELL and Re3CHELL.

- *Chapter 5* demonstrates the use of the Polynomial Chaos Expansion to help quantify which variables are the most influential on the buckling response of a conical-cylindrical shell. Polynomial Chaos Expansion was also used to highlight differences in the linear eigenvalue and geometrically nonlinear analyses to predict the buckling behavior for conical-cylindrical shell. Isotropic and composite shells were considered. This polynomial chaos expansion helps validate some of the observations witnessed in the numerical studies presented in Chapter 3 and Chapter 4.

- *Chapter 6* serves as a synthesis of the key findings presented throughout the thesis, contextualizing them within the broader framework of launch-vehicle structural design. Future research topics are presented based on these conclusions.

2

ANALYSIS AND VALIDATION OF A SCALED, LAUNCH-VEHICLE-LIKE COMPOSITE CYLINDER UNDER AXIAL COMPRESSION

LAUNCH-VEHICLE *structures, such as payload adapters and interstages, are increasingly designed and constructed using composite materials due to their high stiffness- and strength-to-weight ratios. Therefore, it is important to develop a validated finite element modeling methodology for designing and analyzing composite launch-vehicle shell structures. This can be achieved, in part, by correlating high-fidelity numerical models with test data. Buckling is often an important failure mode for cylindrical shells, and the buckling response of such structures is also often quite sensitive to imperfections in geometry and loading. Hence, it is crucial to understand the model parameters and details required to accurately predict the buckling load and behavior of composite cylindrical shells, especially if the shell is buckling critical. The inclusion of as-built features, such as radial imperfections, thickness variations, and loading imperfections can help improve the correlation between test and analysis. To demonstrate such an approach, a validated modeling methodology that was used to predict the buckling behavior of a scaled component for a launch-vehicle-like structure is presented, and results from the model are compared with experimental results. The modeling approach presented herein was used to successfully predict the buckling behavior.*

This chapter has been adapted from Rudd M.T., Eberlein D.J., Waters W.A., Gardner N.W, Schultz M.R, Bisagni C., “Analysis and Validation of a Scaled, Launch-Vehicle-Like Composite Cylinder under Axial Compression,” Composite Structures, Vol. 304, Part 1, 2023, 116393. https://doi.org/10.1016/j.compstruct.2022.116393.

2.1. INTRODUCTION

Launch-vehicle designs regularly incorporate thin-walled cylindrical shell structures. The use of composite materials to construct these structures, such as payload adapters and interstages, has become more common in recent years. When axially compressed, thin-walled shells are highly susceptible to global buckling, which results in a sudden loss in load-carrying capacity under axial compression. It is well-known that the buckling behavior is highly dependent on sources of variations from theoretically ideal shells. These variations may include, but are not limited to, radial geometric imperfections, thickness variations, and loading nonuniformity. Thus, these variations can make it difficult to predict the buckling load, even with state-of-the-art analysis tools. Therefore, it is important to have an experimentally validated modeling methodology to provide confidence in the predicted buckling behavior of a composite cylinder. A validated finite element methodology can be used to assess the sensitivity of the shell to imperfections and may also be used to assess new design approaches for buckling-critical launch vehicle structures.

Before advances in computer simulations, researchers relied on analytical methods to predict buckling loads of composite cylinders. Koiter [7] noted that the inclusion of radial imperfections was important when predicting the buckling load of a composite cylinder. To predict the buckling load before the test, researchers such as Bert, et al. [8], Card [9], Tennyson and Muggeridge [10], and Herakovich [11] measured the amplitude of the radial geometric imperfections of test articles. An assumed shape of this amplitude was then incorporated into the analytical solution as a prebuckling deformation in order to best predict the buckling load.

Unlike analytical methods, a greater level of detail can easily be included in finite element models (FEMs) to more closely represent as-manufactured physical composite structures. Hilburger and Starnes [12] used the general-purpose finite element code STAGS (Structural Analysis of General Shells) to predict the buckling performance of four composite cylinders. Validation tests, or tests conducted to validate the FEM, enabled the authors to investigate significant details, such as radial geometric imperfections, ply gaps, thickness imperfections, shell-end geometric imperfections, nonuniform loading, and elastic boundary conditions. Khakimova, et al. [13] included fiber volume fraction, in addition to radial imperfections and thickness variations, in finite element models. They also showed that the predicted buckling load converged to the tested buckling load by increasing the level of as-built details in their models.

Incorporating the as-built details of a composite cylinder into the FEM is important, but it is also necessary to understand how analysis parameters such as element type, mesh size, and the analysis solver influence the predicted buckling behavior. To address this uncertainty, Bisagni [14] conducted an extensive numerical study using the general-purpose finite element code, Abaqus. This study was completed before testing a carbon fiber reinforced polymer (CFRP) cylinder with a layup of [0/45/-45/0]. In this investigation, Bisagni performed linear eigenvalue, nonlinear Riks, and implicit dynamics (under quasi-static conditions) buckling analyses. The author noted that there were negligible differences between the Riks and dynamic solutions with respect to the quasi-static nonlinear response. In addition, a mesh convergence study was performed using the four-node shell element with reduced integration (S4R). The outcomes of this assessment led the author to use the S4R element with a mesh size of 0.6 elements/degree around the circumference and to use the dynamic solver. Priyadarsini, et al. [15] completed a similar study and determined that that same element type, mesh density, and solver were adequate to assess the buckling behavior of four identical CFRP laminate specimens with a layup of [0/45/-45/0]S . Ghalghachi, et al. [16] completed five buckling tests with five glass fabric reinforced polymer cylindrical shells. Ghalghachi, et al. used the same program and S4R element as Bisagni and Priyadarsini, et al., but used the Riks method to investigate the buckling behavior. The aforementioned authors studied constant-stiffness cylinders, while other researchers have developed FEMs with similar model parameters to investigate the buckling behavior of variable stiffness composite cylinders and composite cylinders with cutouts [17, 18, 19, 20, 21].

Finite element models validated by testing have provided researchers with enhanced confidence in their numerical tools to develop probabilistic-based design approaches for buckling-critical composite cylinders. Degenhardt, et al. [22] used a validated high-fidelity model to perform a Monte Carlo simulation that addressed the sensitivities to imperfections. From that simulation, they determined the buckling knockdown factor — used in design to account for differences between test and analysis — for a composite cylinder with a radius/thickness ratio of 500 could be increased from the recommended knockdown factor calculated using NASA-SP-8007 [5]. Schillo, et al. [23] tested eleven nominally identical layups and developed a validated model to identify the influence of uncertainties for a reliability-based design approach.

In addition to probabilistic approaches, other researchers have identified the benefits of using validated models to develop new buckling knockdown factors. After validating a finite element model with testing, Hühne, et al. [24] proposed a less conservative lower bound buckling knockdown factor methodology using the single perturbation load approach (SPLA). These factors have the potential to be less conservative than those recommended for the empirical design approach in NASA-SP-8007, which may lead to mass savings of thin-walled shell structures made from composites. Similar to the SPLA, Wagner, et al. [6] determined the single boundary perturbation approach (SBPA) can also potentially provide less conservative buckling knockdown factors using a validated FEM.

The NASA Shell Buckling Knockdown Factor Project (SBKF) had the objective of aiding in the development of design-specific knockdown factors for launch vehicles by developing a validated modeling methodology using scaled sandwich composite cylindrical shells. Schultz, et al. [25] suggested that new knockdown factors could save 4% to 19% areal mass for sandwich composite launch vehicle structures. Four 2.4 m diameter sandwich composite cylinders were tested by NASA researchers as part of an effort to validate a finite element analysis approach to predict the buckling behavior. The buckling loads were predicted within 7% of the experiments [26, 27, 28].

In the present chapter, the authors demonstrate a modeling methodology that successfully predicted the buckling behavior of a scaled launch vehicle-like composite cylindrical shell. It is herein referred to as NASA-Delft Laminate 1 (NDL-1) with a layup based on a novel scaling methodology [29]. The goal of the scaling methodology is to produce a smaller-scale, solid laminate design which can mimic the buckling behavior of a large-scale launch vehicle sandwich-composite buckling-critical composite shell. While this methodology has been demonstrated analytically and numerically, it is of interest to validate experimentally that the designs produced by the scaling methodology are buckling critical since the stacking sequences produced are nontraditional. Before the test, a detailed study was performed to determine the most appropriate model parameters. The high-fidelity model included details such as radial imperfections and thickness variations measured using a structured light scanning optical measurement system [30]. The material properties of the laminate were characterized by coupon testing. A detailed assessment is presented that compares the predicted prebuckling, buckling, and post-buckling radial displacements with low-speed and high-speed digital image correlation. Specifically, the chapter describes in detail the buckling propagation over the 16.3 milliseconds captured by the high-speed cameras as compared to the finite element analysis. The level of detail and modeling approach presented in this paper can be applied to large-scale buckling-critical composite launch vehicle structures.

The NDL-1 test article design and manufacturing is presented in Section 2.2. A summary of the as-built geometric imperfections and details of the finite element model used for pretest predictions are described in Section 2.3 and Section 2.4, respectively. The experimental setup is covered in Section 2.5. The results and discussion of Section 2.6 includes a comparison of the pretest predictions and post-test analysis correlation.

2.2. TEST ARTICLE DESIGN AND MANUFACTURING

The test article, NDL-1, was manufactured from a carbon fiber-epoxy material system and had a nominal diameter of 800 mm, a nominal height of 1200 mm, and a layup in the acreage region of $[23/0/-23]_{4s}$. The acreage layup was determined by a novel scaling methodology and was designed to fail in buckling. The analytical scaling methodology was used to determine a reduced-scale composite cylinder design that has a buckling behavior similar to a full-scale sandwich composite cylinder. This was achieved by matching the nondimensional parameters of the scaled design to the full-scale design [29]. The NDL-1 solid laminate design is a scaled-down version of the 2.4 m diameter sandwich composite cylinder, CTA8.1, which was designed and tested as a part of the SBKF [26]. The resulting designs from the scaling process are not constrained to common layup orientations, such as 0, 45, and 90 degrees, hence an unconventional design with angles of +/- 23 degrees could also be considered.

The laminated composite cylindrical shell, NDL-1, was fabricated with 12.5-mm-wide unidirectional (UD) tows of Hexcel IM7/8552-1 (190 gsm), each 0.175 mm thick [31]. The in-plane elastic moduli E_{11} and E_{22} (with 1 and 2 representing, respectively, the 0 and 90 degree UD fiber angles), the in-plane shear modulus (G_{12}), and the in-plane Poisson's ratio (ν_{12}) for IM7/8552-1 lamina are listed in Table 2.1 [32]. Reference [31] provided failure stresses; therefore, failure strains were calculated assuming linear elastic behavior using the documented moduli and failure stresses. These failure stresses and calculated failure strains are reported in Table 2.2. The calculated strains were then used to confirm the buckling failure of NDL-1.

The test article was fabricated using the advanced fiber placement robot at the NASA Marshall Space Flight Center (MSFC) Composites Technology Lab. To manufacture the $[(23/0/-23)]_{4s}$ acreage layup, the unidirectional plies were laid on the outer surface of an aluminum cylindrical mandrel in the desired fiber orientation. The 0-degree direction is parallel to the longitudinal axis and the 90-degree direction is oriented circumferentially,

Table 2.1: Nominal lamina properties of Hexcel IM7/8552-1 composite.

0-degree modulus E_{11} (GPa)	90-degree modulus E_{22} (GPa)	Shear modulus G_{12} (GPa)	Poisson's ratio ν_{12} (-)
140.9	9.72	4.69	0.356

Table 2.2: Documented B-basis laminate failure stresses and calculated failure strains.

Direction	Failure stress (MPa)	Calculated failure strain ($\mu\varepsilon$)
0-degree Compressive	1731	-12,280
90-degree Tensile	64	6584

or in the hoop direction. Additional plies, referred to as padups, were added at the ends of the test article to assist with load introduction. The test article weighed 20.68 kg. Its acreage and padup details are presented in Figure 2.1 and Table 2.3. The padups consist of up to three plies — 90 degree, 45 degree, and -45 degree — that terminate sequentially near the ends. The 90-degree ply was the last ply to be dropped, closest to the midheight, followed by the 45- and -45-degree plies, respectively.

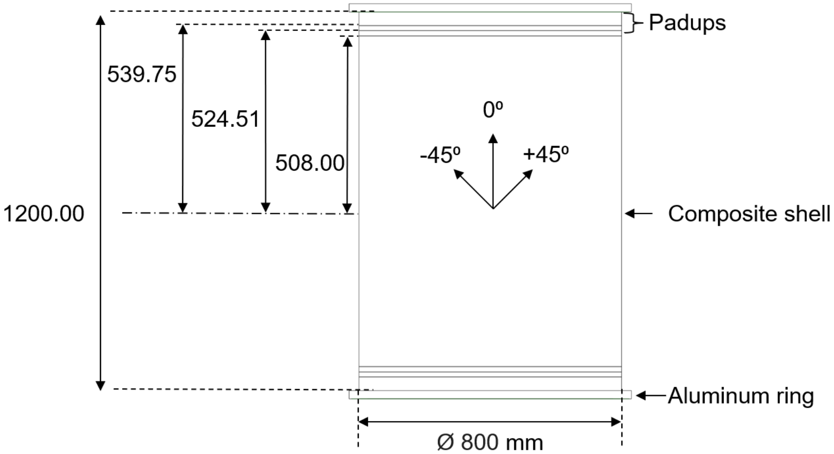

Figure 2.1: NDL-1 geometry. All dimensions in millimeters.

The unconventional layup led to some significant manufacturing challenges. To start with, the laminate had a in-plane Poisson's ratio greater than 1.00. Also, the highly axially stiff layup and its associated coefficient of thermal expansion made it difficult to remove the composite cylinder from the aluminum mandrel; there was minimal clearance between the acreage section and the mandrel. A larger gap was present between the

Table 2.3: Nominal NDL-1 acreage and padup layup details.

Region	Layup	Axial location from midheight (0 mm) of padup termination
Acreage	$[(23/0/-23)]_{4s}$	-
Padup 1	$[(23/0/-23)_{3s}/(23/0/-23/\overline{90})_s]$	+/- 508.00
Padup 2	$[(23/0/-23)_{3s}/\overline{-45}/(23/0/-23/\overline{90})_s]$	+/- 524.51
Padup 3	$[(23/0/-23)_{2s}/(23/0/-23/\overline{45})_s/\text{-}45/(23/0/-23/\overline{90})_s]$	+/- 539.75

mandrel and the test article in the padup regions, potentially due to the presence of 0-degree and 90-degree plies.

After manufacturing, the ends of the composite cylinder were encased in an epoxy grout material to prevent brooming at the ends. In numerical simulations, the effect of the encasing is approximated using clamped boundary conditions. The grout was 25.4-mm thick on each end and extended approximately 22.9-mm away from the inner mold line (IML) and outer mold line (OML) surfaces of the composite cylinder. The innermost and outermost grout surfaces were encased with 6.35-mm thick aluminum rings. The ends of the test article were machined flat and parallel, with the shell exposed on either end to ensure uniform compressive load introduction directly into the test article, Figure 2.2.

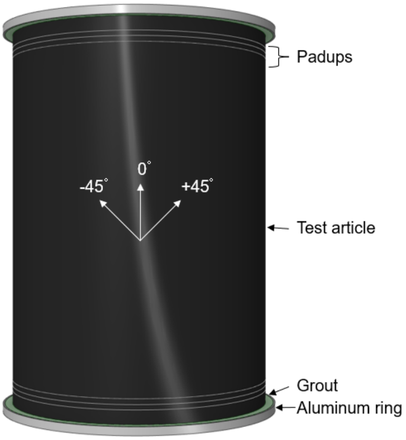

Figure 2.2: 3-dimensional view of NDL-1 Assembly.

2.3. MEASURED GEOMETRIC IMPERFECTIONS

After fabrication, the shape of NDL-1 was measured via structured light scanning to capture the radial position of the IML and OML surfaces. This data represents the as-built geometry of NDL-1. Structured light scanning is a photogrammetric technique that is used to capture the surface of the test article in a three-dimensional space. The IML and OML of the shell were scanned and combined in a single coordinate system to determine the radial location of the shell and the shell -end surfaces, along with thickness variations. The NDL-1 OML and IML radial locations are shown in Figure 2.3a and Figure 2.3b in an unrolled view. The blue colors correspond to a relatively inward position, while the red colors correspond to a relatively outward position. The radial position on the OML ranged from 406.60 mm to 403.58 mm. The radial position of the IML ranged from 401.10 mm to 399.35 mm. The average IML radial position was 400.23 mm and the nominal IML radius was 400 mm. A distinct feature can be observed in the OML and IML data, but it is more prominent in the IML: a band approximately 50 mm wide that extends around the entire circumference of the test article, centered approximately 150 mm above the midheight (0 mm). The aluminum mandrel on which NDL-1 was built was also analyzed with a structured light scanning, and this feature was present in the mandrel data. It was determined that this feature was an artifact of the surface machining process, and it was concluded that it was transferred from the mandrel to the NDL-1 during fabrication. The thickness variations of NDL-1 are presented in Figure 2.3c where the warmer (red) colors correspond to thicker regions and the cooler (blue) colors denote relatively thinner regions. The diagonal pattern in Figure 2.3c matches the 23-degree ply angle and corresponds to ply gaps and overlaps. Note that because structured light scanning output point cloud data, and the OML and IML spatial data points were not spaced at the same radial/circumferential positions precisely, the thickness plot shown in Figure 2.3c was derived by interpolating the OML and IML radial data to a regularly spaced axial and circumferential set. The interpolated IML data was subtracted from the interpolated OML data to give the shell's thickness profile. (The interpolated OML and IML were used in the FEM.)

In addition to the IML and OML surfaces, the top and bottom shell end surfaces of NDL-1, which interface with the load frame, were also scanned. The data from the top shell end surface is plotted in Figure 2.4a, and data from the bottom end surface is plotted in Figure 2.4b. The total variation in the top ring was 0.46 mm. The highest location was approximately 180 degrees from the lowest location. This was similar to the bottom surface, but the bottom surface had a maximum imperfection amplitude of 0.44 mm. Capturing this data is important in assessing the effects of nonuniform loading in the finite element model.

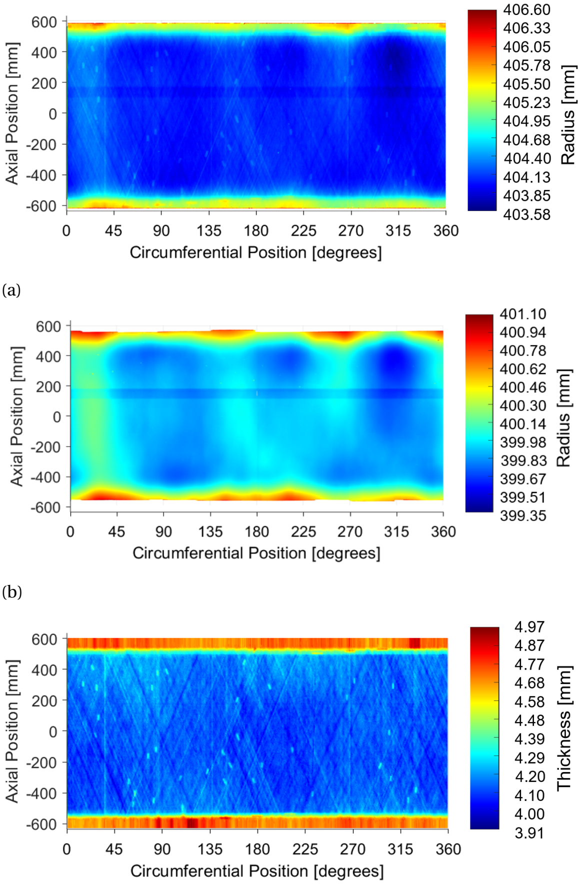

(a)

(b)

(c)

Figure 2.3: NDL-1 radial and thickness imperfections : a) OML radial surface data; b) IML radial surface data ; c) Interpolated thicknesses

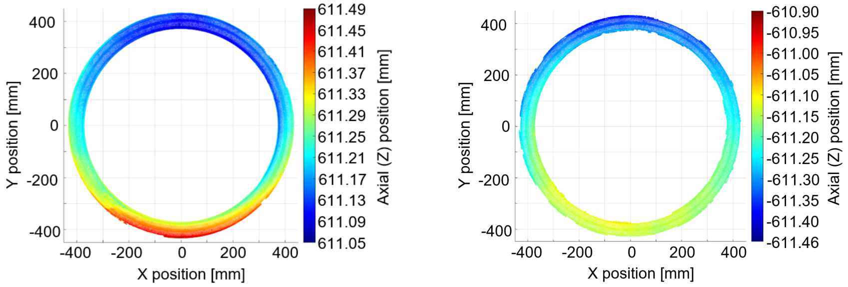

(a)

(b)

Figure 2.4: NDL-1 axial position of a) top and b) bottom shell end surfaces.

2.4. FINITE ELEMENT MODEL AND ANALYSIS

The finite element program used for the pre-test predictions and post-test analysis correlation was Abaqus 2017 [33]. The modeling and analyses were performed at the Delft University of Technology. Prior to developing the finite element model to predict the buckling load and behavior of NDL-1, an investigation was conducted and documented to understand the effect that the element type and mesh size have on the buckling response. Also, this section presents a discussion of the laminate material property characterization that was used in the finite element model for the pre-test predictions and post-test analysis correlation. Finally, parameters of the implicit dynamic analysis used for the predictions are presented.

2.4.1. ELEMENT TYPE AND MESH SIZE SELECTION

A finite element model of the composite test article NDL-1 (with nominal geometry) was used to investigate the predictions obtained from two distinct shell element types, namely (i) the S4R four-node conventional shell element and (ii) the SC8R eight-node continuum shell element. The former uses the midsurface displacements and the transverse section rotations as degrees of freedom, while the latter uses all through-the-thickness displacements as degrees of freedom. Both elements allow transverse shear deformations, and both are suitable for geometric nonlinear problems [32]. In the simulations involving the continuum shell element SC8R element, only one element through the thickness was used.

A mesh convergence study was conducted with both the S4R and SC8R elements by comparing the eigenvalue buckling loads. The results are presented in Figure 2.5 for mesh sizes of 50 mm, 25 mm, 20 mm, 10 mm, 7.5 mm, and 5 mm. This corresponds to approximately 1100, 4500, 7000, 28,000, 50,000, and 112,000 elements, respectively. In the figure, the predicted buckling loads for the S4R and SC8R elements, dashed and solid lines, respectively, begin to converge and plateau at a mesh size of 10 mm (approximately 28,000 elements). Ultimately, a mesh size of 5 mm (approximately 112,000 elements) was selected to better capture the imperfection signatures of the OML and IML. The 5 mm mesh size is approximately 0.7 elements per degree around the circumference.

Both eigenvalue and nonlinear dynamic analyses were performed to assess S4R and SC8R elements with the 5mm mesh size. There is less than a 1% difference between the eigenvalue buckling loads of the S4R and SC8R models, 2284 kN and 2295 kN, respectively. Additionally, the eigenvalue buckling load for both element types are within 1% or less of the analytical buckling load of 2271 kN calculated using Equation 2.1, where N_x is the buckling load per unit length, l is the length of the cylindrical shell, m is the number of axial half-waves, and the matrix A_{ij} corresponds to the laminate stiffness. Matrix A_{ij} is a function of m and n (number of circumferential waves) [5]. The critical number of m and n is 9 and 0, respectively. This was determined by minimizing equation 2.1 with respect to m and n. The buckling mode shapes for the two element types are also very similar for the first mode as seen in Figure 2.6. The predicted buckling loads for each element type for the eigenvalue and nonlinear dynamic analyses are listed in Table 2.4.

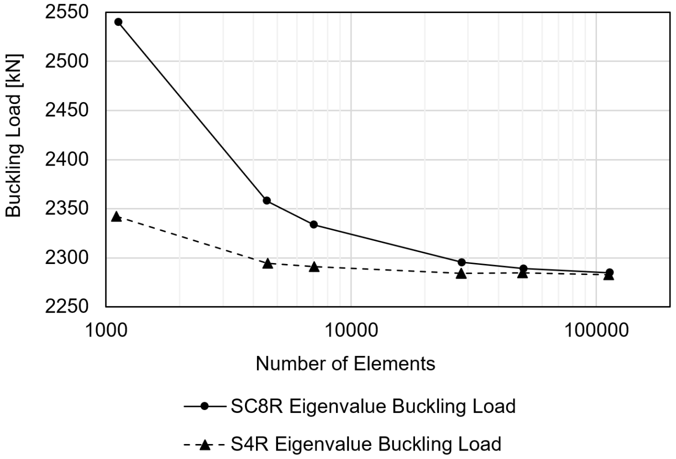

Figure 2.5: The eigenvalue buckling load for S4R and SC8R shell models versus the number of elements.

$$N_x = \left(\frac{l}{m\pi}\right)\frac{\begin{vmatrix} A_{11} & A_{12} & A_{13} \\ A_{21} & A_{22} & A_{23} \\ A_{31} & A_{32} & A_{33} \end{vmatrix}}{\begin{vmatrix} A_{11} & A_{12} \\ A_{21} & A_{22} \end{vmatrix}} \tag{2.1}$$

In addition, the buckling loads predicted from nonlinear dynamic analyses using both element types were nearly identical (1 kN difference, or well within 1%). Given that both element types predicted similar behaviors, the SC8R was selected for compatibility with in-house imperfection-processing software. Nodal coordinates of the SC8R elements were manipulated to match the surface positions of the OML and IML data. Moving the OML and IML nodes accounts for the thickness variations by default. In contrast, S4R elements would have required mid-surfacing the IML and OML data, along with individual element-by-element thickness assignments.

Table 2.4: Buckling loads determined by eigenvalue analysis and nonlinear dynamic analysis for S4R and SC8R elements.

Element	Eigenvalue Analysis [kN]	Nonlinear Dynamic Analysis [kN]
S4R	2284	2193
SC8R	2295	2194
Difference	-0.4%	≈ 0%

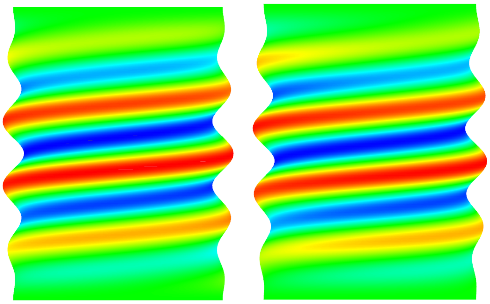
(a) (b)

Figure 2.6: First buckling mode shapes: a) S4R elements; b) SC8R elements.

While the composite cylinder was modeled using SC8R elements, the potting material and aluminum rings were modeled with C3D8 three-dimensional brick elements. A detailed view of the FEM is shown in Figure 2.7. The yellow-orange color corresponds to the continuum shell elements with properties for padup 3. The blue color represents the continuum shell elements with properties for padup 2, the red corresponds to padup 1, and the cyan represents the acreage. The potting is represented by the purple color, and the aluminum rings are gray.

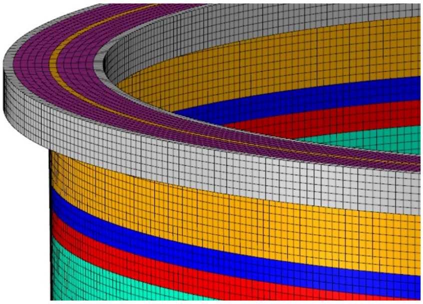

Figure 2.7: FEM details.

2.4.2. MATERIAL PROPERTIES

Laminate coupon testing was completed before the test of NDL-1 to characterize the laminate stiffness of its unconventional layup, $[23/0/\text{-}23]_4s$. Seven tensile coupon specimens, nominally 24.5 mm wide and 4.32 mm thick, were built with the same layup as NDL-1. A summary of the longitudinal laminate modulus (E_{11}), Poisson's ratio, width, and thickness from the seven tested specimens is shown in 2.5. The coupon specimens were 4.3% thicker than the average acreage thickness of the test article. The average cured ply thickness was 0.180 mm for the coupon specimen, and 0.173 mm for the test article. Due to the thickness discrepancy, two different assumptions were made when extrapolating resultant ply properties from the coupon test to the test article and its FEM. The first was that the coupon specimen and test article had the same constant fiber volume fraction. The second assumption was that the number of fibers per unit area was the same in the coupon specimen and the test article. In this case, it was assumed the number of fibers remained constant per unit area, but excess resin bled off during the cure cycle of the test article, thereby causing the thickness discrepancy. The intent of creating two sets of material properties was to bound the response of NDL-1 since there are more potential sources of variation when manufacturing with unidirectional tows.

Table 2.5: Summary of NDL-1 laminate tensile test data.

Specimen Number	1	2	3	4	5	6	7	Mean
Longitudinal modulus [GPa]	107.3	108.7	115.0	109.4	106.1	108.8	105.3	108.7
Poisson's ratio [-]	1.24	1.29	1.29	1.28	1.27	1.31	1.35	1.29
Width [mm]	25.3	25.4	25.4	25.4	25.4	25.4	25.4	25.4
Thickness [mm]	4.32	4.32	4.32	4.34	4.32	4.39	4.32	4.32

Using the data from the tensile tests, the associated local fiber-direction (E_{11}) and transverse (E_{22}) lamina stiffnesses to be used in the FEM of NDL-1 were determined through a virtual coupon test. The nominal tensile specimen was modeled using SC8R elements and the nominal lamina E_{11} and E_{22} properties of Table 2.5 as an initial guess. They are reported in the first row of Table 2.6 for comparison and are called the "nominal properties". The lamina moduli E_{11} and E_{22} were modified in the finite element program until the predicted laminate's overall longitudinal stiffness and Poisson's ratio from the virtual tensile test matched the corresponding mean values from the coupon tests (108.7 GPa and 1.29, respectively) within 1%. Those E_{11} and E_{22} properties, the second row of Table 2.6, satisfy the assumption that the test article and coupon specimens had the same fiber volume fraction.

Table 2.6: Nominal lamina properties of Hexcel IM7/8552-1 composite.

Property Set	E_{11} (GPa)	E_{22} (GPa)	G_{12} (GPa)	ν_{12} (-)
Nominal	140.9	9.72	4.69	0.356
Constant fiber volume fraction	152.2	8.75	4.69	0.356
Constant quantity of fibers	158.7	9.12	4.69	0.356

Two different finite element models were developed, one with the constant-fiber-volume-fraction moduli and one with the constant-quantity-of-fibers moduli. These models will be referred to as the pretest prediction models. The potting was modeled assuming isotropic material properties with an elastic modulus of 7.58 GPa and a Poisson's ratio of 0.3. The aluminum ring was modeled with an elastic modulus of 69.00 GPa and a Poisson's ratio of 0.33.

2.4.3. ANALYSIS

Nonlinear implicit dynamic analyses were performed to predict the pre-buckling, buckling, and post-buckling response of NDL-1 using the constant-fiber-volume-fraction assumption and the constant-quantity-of-fibers assumption. To apply the displacement, a single reference node in the center of the test article at the top was connected to the top edge nodes of the test article, potting, and aluminum ring through tie constraints. The top reference node had all degrees of freedom constrained except for the axial direction. The bottom of the test article was similarly tied to a reference node centered at the bottom edge of the cylinder using the same technique. All degrees of freedom associated with the bottom reference point were fixed.

A total displacement of 2.5 mm was applied to the top reference node at a rate of 2 mm per minute in the axially compressive direction. The total displacement was divided into two steps. The first step, or pre-buckling step, was a dynamic analysis that specified 0.12 seconds for the initial and maximum increment. The second step of the analysis began after a time period of 60 seconds. The load rate remained constant, but the initial and maximum increments were decreased to 0.009 seconds. This defined the buckling phase of the analysis. The larger time step in the prebuckling phase was to increase computational efficiency. The smaller time step was employed during the buckling step to ensure the peak load was captured accurately and to have a detailed understanding of the predicted buckling progression. This combination of steps allowed the analysis to be reasonably computationally efficient, while still obtaining the desired buckling data.

2.5. EXPERIMENTAL SETUP

Test article NDL-1 was tested in axial compression at NASA Langley Research Center using a load frame which is capable of applying up to 3000 kN. In the compression loading set up, the top platen was fixed and the test article was compressed by the bottom platen, actuated by a hydraulic system. The experimental setup is shown Figure 2.8. Three subcritical load sequences — in which failure was not expected — were planned before the final test to failure. The subcritical load sequences consisted of loading NDL-1 in pure axial compression at levels that were 20%, 40%, and 60% of the test article's predicted linear bifurcation load, 2295 kN. A displacement-controlled compression rate of 0.08 mm/min was applied for all load sequences.

Test data was obtained from several instrumentation sources. The load was measured via a load cell. Displacement was measured by six direct current differential transducers (DCDTs) positioned around the load frame, Figure 2.9. Strain was measured with 32 electrical resistance strain gages as shown in Figure 2.10. The OML gauges were odd numbers, and the IML gauges were even numbers. On both the IML and OML surfaces, 12 axially oriented gauges were spaced at 0, 90, 180, and 270 degrees around the circumference with axial positions of -562 mm, 0 mm (midheight), and 562 mm. These gauges were designated with an “A” which references the axial direction. Additionally, four inner and four outer midheight gauges measured hoop strain at 0, 90, 180, and 270 degrees. These gauges were designated with an “H” which references the hoop direction.

Eight digital image correlation (DIC) systems were used to observe the experiment: four low-speed systems and four high-speed systems, with each system comprised two cameras in a stereo configuration. The low-speed data was captured at a rate of 1 frame per

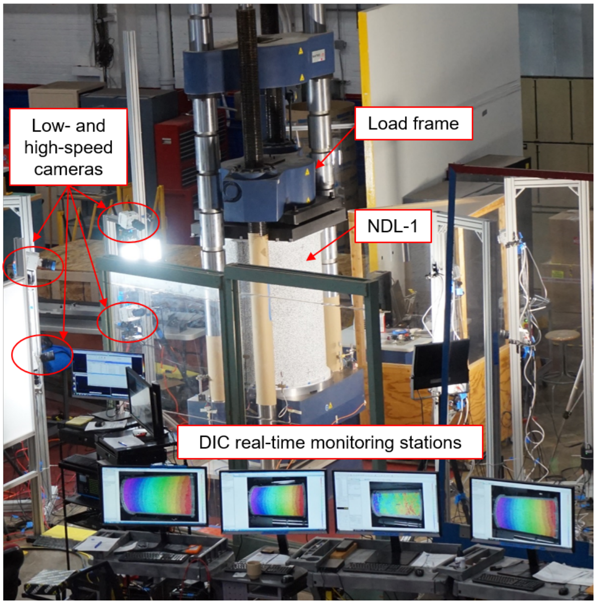

Figure 2.8: NDL-1 experimental setup at NASA Langley Research Center.

second. The lenses and standoff distances were selected such that the system's resolution was optimized for the desired field-of-view, i.e., maximum spatial resolution. The high-speed data was captured at a rate of 20,000 frames per second. The outer surface of the test article, which included the composite cylinder and the aluminum ring containing the potting, had a high-contrasting speckle pattern applied for DIC as seen in Figure 2.8. The ideal speckle diameter for the low-speed system was generally between 4 and 6 pixels. However, the speckle pattern diameter was doubled to 8 to 12 pixels/speckle for the low-speed systems to accommodate the lower resolution of the high-speed cameras, because the latter's chosen resolution was lower than the former's. This translated to a speckle size ranging from 4.5 mm to 6 mm.

Low-speed and high-speed camera pairs were positioned facing the circumferential positions of the shell at 45, 135, 225, and 315 degrees as indicated in Figure 2.11. The fields of view for the DIC systems were centered on the NDL-1 midheight. Low-speed DIC recorded throughout the entire test. Prebuckling radial and axial displacements were generated from this data. High-speed DIC was used to capture the buckling event (initiation and propagation). Real-time monitoring stations were used to observe full-field displacements and strains from low-speed DIC along with load and axial displacements during the test.

The top load platen was balanced to help ensure even load introduction before the first load sequence. The top load platen system consisted of the two black plates located above NDL-1 in Figure 2.8. Between the two plates was a hemispherical joint that was centered in the middle of the plates. To balance the top load platen, the readings for the eight back-to-back strain gauges placed every 90-degrees on the top end of the test article must be within 10% of each other. Virtual extensometers within the DIC software were also utilized to examine the load introduction in areas where strain gages were not present. Based on the virtual extensometer data, the top shell end surface was shimmed between the 210-degree and 315-degree circumferential locations to allow for a more uniform load introduction.

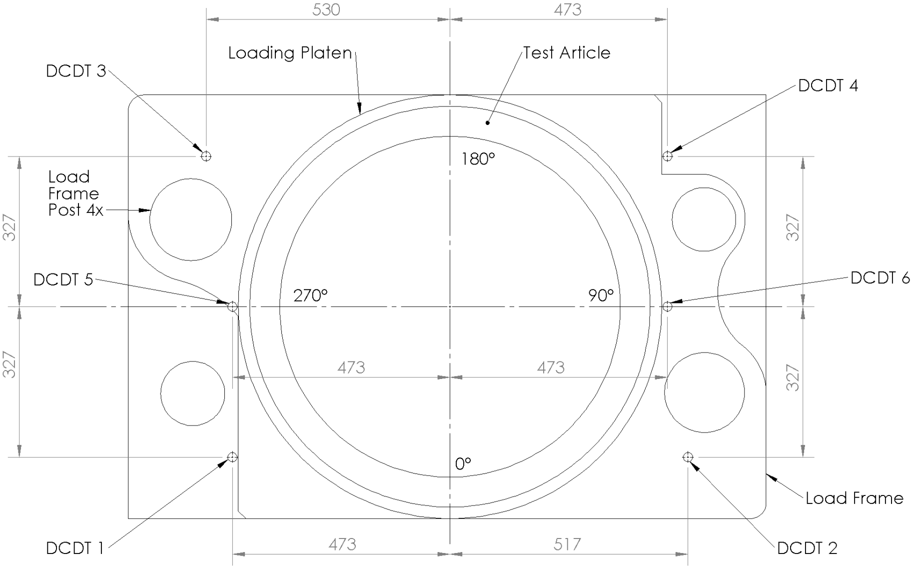

Figure 2.9: Mid-section top-view drawing of the load frame indicating angular locations and DCDT mounting points. All dimensions are in millimeters.

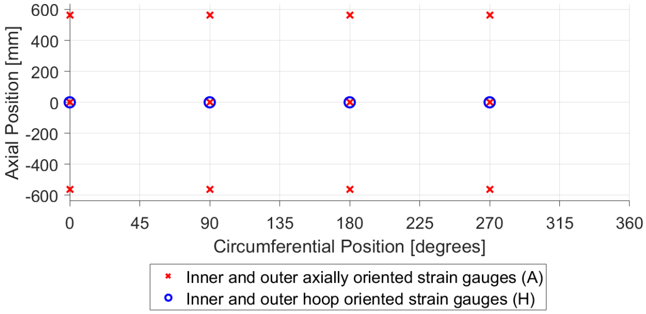

Figure 2.10: Strain gauge locations and orientations on the shell and gauge number.

2.6. RESULTS AND DISCUSSION

A comparison of the data derived from pretest prediction models as described in Section 2.5 and the experimental data is presented. First, a comparison of the load versus axial displacement data is described. Next, the axial and circumferential membrane strains are compared. Then, the radial contour plots generated from the low-speed DIC data are compared against the FEM predictions for the prebuckling response and incipient buckling behavior. Finally, the postbuckling response as measured by the high-speed DIC data is presented.

2.6.1. PRETEST PREDICTION MODELS AND TEST DATA COMPARISON

During the test-to-failure load sequence, NDL-1 failed at a peak load of 2077 kN and a total axial displacement of 2.19 mm. The overall behavior of the test article matched the pretest predictions well for both models, — constant-fiber-volume-fraction and constant-quantity-of-fibers— as seen in the load versus displacement plot of Figure 2.12. The black line corresponds to the test data in which the average axial displacement was derived from the low-speed DIC data. Both pretest prediction models contained the measured radial and thickness imperfections (Figure 2.3), and top and bottom shell surface imperfections (Figure 2.4). The blue line represents the pretest predictions for the material properties assuming a constant fiber volume fraction as described in Section 2.4.2. The orange line represents the pretest predictions using the same measured imperfections but assumes a constant quantity of fibers per unit area. Both models show good correlation, but

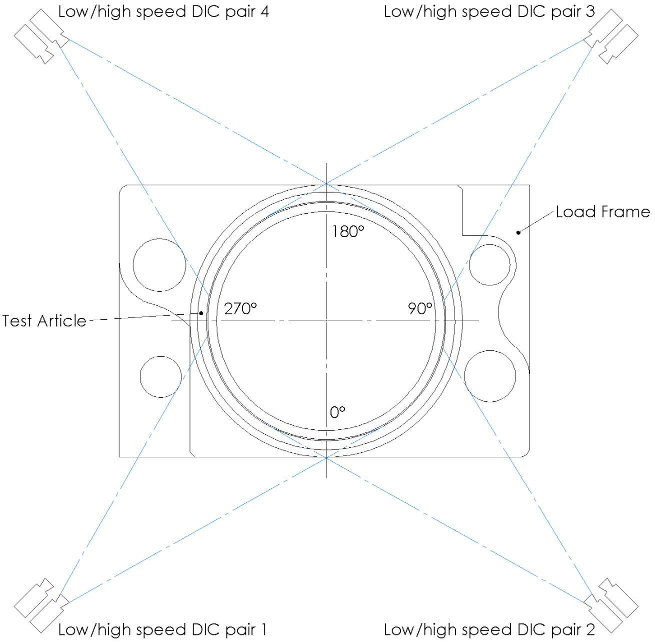

Figure 2.11: Locations of DIC systems. Approximate fields of view are indicated by blue lines.

the constant-fiber-volume-fraction model matches the test data better by predicting a buckling load of 2075 kN, a 0.04% difference from the test. The constant-quantity-of-fiber model predicted a buckling load of 2154 kN, a 3.7% difference. There is a 0.2% difference in stiffness between the constant-fiber-volume-fraction model and the test data, and a 3.7% difference between the stiffness of the constant-quantity-of-fibers model and the test data. Since the constant-fiber-volume-fraction model correlated better, those results are presented herein.

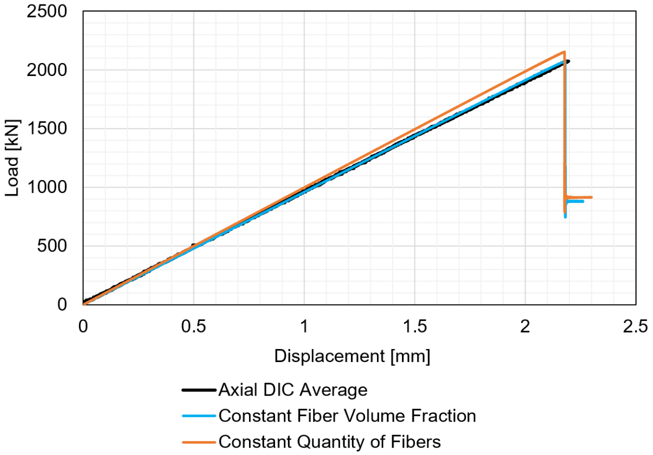

Figure 2.12: Load versus average displacements plot.

The intent of the shims was to improve load uniformity. The influence of the end conditions was assessed by also running a model without the shell end imperfections. There was the difference in end conditions. The responses predicted for models with and without the shell end imperfections were nearly identical. Therefore, a single model, the model with shell-end imperfections, is presented herein. The back-to-back axial (A) membrane strains, or the average strain of the IML and OML gauge, at the top, midheight, and bottom of NDL-1 for the test and FEM, are shown in Figure 2.13a. The measured axial membrane strains remain essentially linear up to the buckling load of 2074 kN. This is also apparent in the FEM data as well. There is more divergence in the membrane strains at the top than there is at the midheight and bottom. The top, +562 mm axial location, axial membrane strains calculated from the test data at buckling at 0-degrees (5A/6A) and 180-degrees (17A/18A) were -1673 $\mu\varepsilon$ and -1704 $\mu\varepsilon$, respectively. The calculated axial membrane strains from the FEM at those locations were -1546 $\mu\varepsilon$ and -1558 $\mu\varepsilon$, respectively, which are 8% less than the predicted values. The axial strains calculated from the test data just prior to buckling for the 90- degree strains (11A/12A) and 270 degrees (23A/24A) circumferential locations were overpredicted by more than 4%. The calculated membrane strain from the test data and from the FEM for gauges 11A/12A were -1504 $\mu\varepsilon$ and -1568 $\mu\varepsilon$, respectively. The calculated axial membrane strains from the test data and predicted strains for 23A/24A were -1473 $\mu\varepsilon$ and -1568 $\mu\varepsilon$, respectively. The higher-than-predicted strains at the 90- and 270-degree circumferential locations indicates potential high spots on the loading surface in those regions. This may be associated with the shims placed between 210- and 315- degrees while balancing the top load platen. It should be noted that these strains are well below the calculated longitudinal compressive failure strain of -12,280 $\mu\varepsilon$ listed in Table 2.2.

It is apparent that the effects of nonuniform loading began to attenuate as the load was distributed down the height of the test article. The percentage difference between the membrane strains calculated from the FEM and from the test data at buckling at the midheight, 0-mm axial position, (Figure 2.13b) are less than at the top. For example, the calculated FEM axial membrane strain at buckling at midheight at the 0-degree circumferential location (3A/4A) and 180-degree (15A/16A) circumferential locations were -1933 $\mu\varepsilon$ and 1941 $\mu\varepsilon$, respectively. These values are approximately 3% less than the calculated axial membrane strains from the test data at buckling, which were -1990 $\mu\varepsilon$ for gauges 3A/4A and -2010 $\mu\varepsilon$ for gauges 15A/16A. As with the top membrane strains, the 0-degree and 180-degree membrane strains were overestimated, and the 90-degree and 270-degree circumferential locations were underestimated. The FEM-calculated membrane strains for gauges 9A/10A were -1932 $\mu\varepsilon$ and 21A/22A was -1908 $\mu\varepsilon$. The membrane strains calculated from test data for those respective locations were -1853 $\mu\varepsilon$ and -1823 $\mu\varepsilon$, which are 5% less than the FEM-calculated axial membrane strains. Also, the strains calculated from the test data at buckling are lower than the calculated compressive longitudinal failure strains listed in Table 2.2.

Similar trends to the top and middle calculated membrane strains are noted when comparing the axial membrane strains from FEM data and test data at the bottom, -562 mm axial position, of NDL-1 (Figure 2.13c) at the buckling load. The calculated predicted strains at buckling for the gauges at 0 degrees (1A/2A) and 180 degrees (13A/14A) were -1588 $\mu\varepsilon$ and -1580 $\mu\varepsilon$. The calculated axial membrane strains from the test data at those respective locations were -1608 $\mu\varepsilon$ and -1617 $\mu\varepsilon$. There was less than a 3% difference between these values. There is also a 3% difference between the calculated strains from FEM and test data for the gauges at 90- and 270-degree circumferential locations (7A/8A and 19A/20A). The membrane strains calculated at the buckling load from FEM data were -1565 $\mu\varepsilon$ and -1562 $\mu\varepsilon$, and the calculated membrane strains from test data at buckling were -1610 $\mu\varepsilon$ and -1606 $\mu\varepsilon$, respectively. These values are also less than the failure strains reported in Table 2.4.

The hoop membrane strains at midheight calculated from the FEM and test data show signs of nonlinearity approaching the peak load, Figure 2.14. This is attributed to the large out-of-plane deformations that occur just prior to and during a buckling event. While a similar curve shape is presented for the measured data and the predicted data, the predicted and measured circumferential strains diverge from the beginning with the predicted circumferential strains typically being less than the observed. The FEM indicates that all calculated membrane hoop strains at 0, 90, 180, and 270 degrees generally have the same slope. This remains true for all membrane hoop strain gauges except for the those determined from gauges 21H/22H at the 270-degree locations. This is consistent with the observation made in the axial membrane data. The maximum predicted membrane hoop strain was 3053 $\mu\varepsilon$ for gauges 3H/4H at the 0-degree circumferential location. The maximum observed membrane hoop strain was 3060 $\mu\varepsilon$ for gauges 15H/16H at the 180-degree circumferential location. These values are also well below the calculated transverse tensile failure strain of 6584 $\mu\varepsilon$, as reported in Table 2.2.

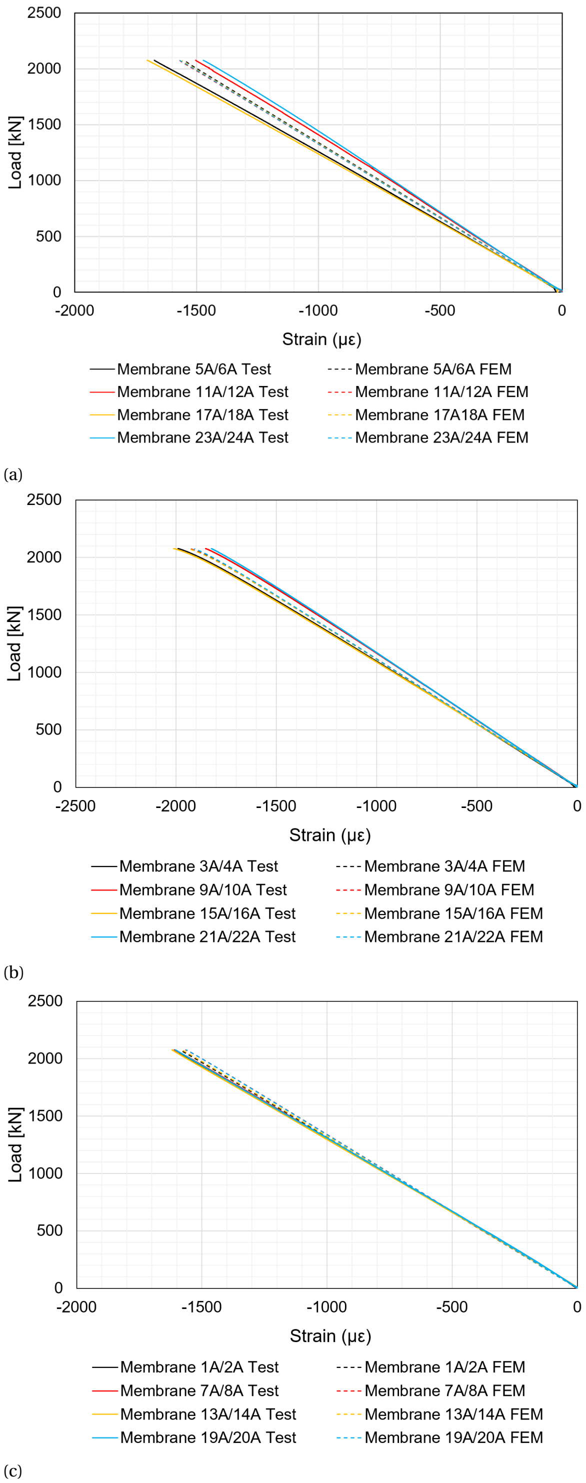

Figure 2.13: Axial membrane strain for the pretest predictions (FEM) and test: a) Top membrane strains; b) Midheight membrane strains; c) Bottom membrane strains.

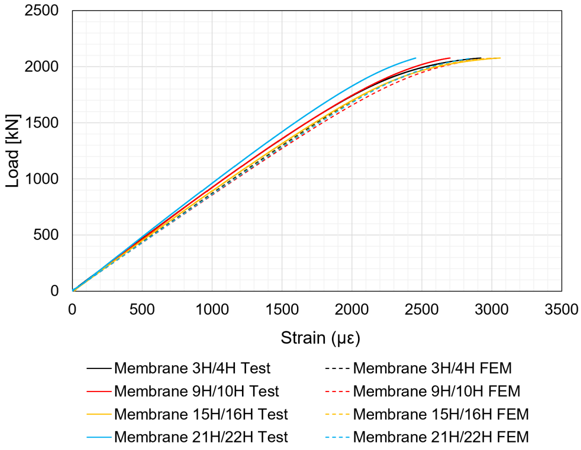

Figure 2.14: Hoop membrane strain for the pretest predictions (FEM) and test.

The radial displacement contours for the test and from the pretest prediction model are presented for the prebuckling, incipient buckling, and postbuckling response. The DIC cameras were not able to measure data over the entire OML because of interference from the load-frame posts; therefore, no full-field strain and displacement data was captured around the 90-degree and 270-degree circumferential locations. The low-speed DIC cameras captured the prebuckling response, while the high-speed DIC cameras captured the bucking and postbuckling response.

The low-speed DIC systems primarily captured the state of the test article prior to and at incipient buckling. Figure 2.15 shows the experimental load versus displacement plot with markers corresponding to 21%, 43%, 64%, 86% and 100% of the experimental buckling load, intervals of 445 kN. These markers relate to Figure 2.16 through Figure 2.20 where the associated radial deformation contours are presented at the specified load levels.

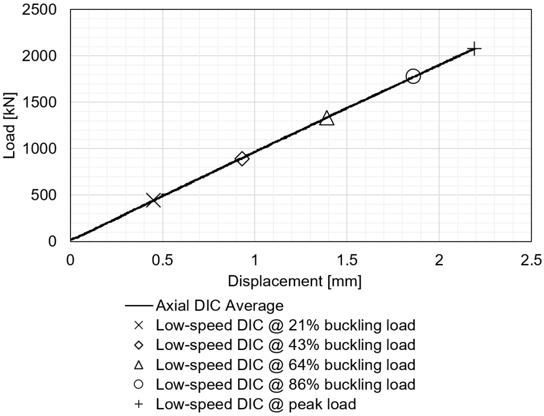

Figure 2.15: Load versus axial displacement from DIC, with markers indicated by symbols corresponding to Figure 2.16 through Figure 2.20.

Starting at a load level of 21% of the experimental buckling load, it can be seen that the test article had a greater radial displacement than what was predicted by the FEM, Figure 2.16. The maximum measured outward radial displacement was 0.45 mm while the predicted was 0.23 mm. The shape of the outward radial deformation in the finite element model was relatively uniform, where the radial deformation predicted in the acreage region ranged from 0.23 mm to 0.21 mm. On the contrary, the test article exhibited an oval-shaped pattern. The maximum outward radial deformation occurred around 22.5-degrees with a magnitude of approximately 0.45 mm. The relative inward deformation exhibited by the test article was -0.22mm. There was no inward radial deformation predicted by FEA. Also, it should be noted that a band appeared between +100 mm and +200 mm in the predicted response, Figure 2.16b. This coincides with the feature on the mandrel in the radial displacements plot in Figure 2.3a and Figure 2.3b , but it does not appear in the test data at this load level, shown in Figure 2.16a.

Trends similar to those observed at 21% of the experimental buckling load were also observed at 43% of the experimental buckling load, Figure 2.17. The outward displacements were underestimated by the model with a predicted maximum displacement of 0.46 mm, but the maximum outward displacement observed was 0.69 mm. The minimum inward deformation is also underestimated because no inward displacement was reported in the FEM data, but the test article maintained its relative inward deformation of -0.22 mm. More distinct circumferential wave features began to develop in the experimental data, which correlates better with the predicted response, but the ovalization was still apparent. The mandrel feature that was observed in the predicted radial deformation plots at 21% of the experimental buckling load, began to appear in the experimental data at 43% of the experimental buckling load.

At 64% and 86% of the experimental buckling load, more defined dimples began to form in both the FEM and experimental data. Most notable was that a band of circumferential waves was witnessed between +100mm and +200 mm, as indicated in Figure 2.18 and Figure 2.19. As the applied load increased, the outward radial deformation increased from 0.70 mm to 0.97 mm in the FEM data. However, no additional inward radial deformation or growth was predicted. With the experimental data, the test article exhibited an increase in outward deformation from 0.99 mm to 1.30 mm. The observed minimum inward deformation remained relatively consistent from 64% to 86%. An inward displacement of -0.27 mm at 64% of the experimental buckling load was noted in Figure 2.18a. The observed inward deformation at 86% of the experimental buckling load was -0.25 mm, Figure 2.19a. No inward deformation was witnessed in the FEM pretest predictions for either load level.

Just prior to buckling, more elements of agreement began to appear between test and analysis with regards to the general shape. Inward dimples started to form and concentrated on the mandrel imperfection feature between axial positions +100 mm and +200 mm, Figure 2.20. The predicted response from the FEM had four dimples spaced 45-degrees apart beginning at 0-degrees between the +100 mm and +200 mm axial positions, which were considered potential failure locations. The test data shows that a single dimple began to dominate the radial deformation plot at the same axial position predicted, +100 mm and +200 mm, at the 200-degree circumferential location. The maximum inward displacement observed in the test was -0.35 mm, while a maximum inward deformation of only -0.04 mm was predicted.

Notably, the growth of the maximum outward radial deformation and minimum inward displacements was relatively consistent between load levels for the experimental data and FEM data. For example, the change in the maximum outward deformation observed in the experimental data between 21% and 43% of the experimental buckling load was 0.23 mm. The test article did not exhibit any change in the inward deformation. Similarly, the difference between the maximum outward deformation in the FEM data from 21% to 43% of the experimental buckling load was 0.24 mm. There was also no predicted change in the minimum inward deformation. From 43% to 64% of the buckling load, the experimental data showed a change in maximum outward deformation and minimum inward deformation as 0.30 mm and -0.05 mm, respectively. For the FEM radial deformations, these same quantities correspond to 0.24 mm and 0.00 mm. The growth in maximum outward displacement from 64% to 84% of the experimental buckling load was 0.31 mm as exhibited by the test article and FEM data showed 0.27 mm. The change in inward radial deformation at the same load level from the experimental data was +0.02 mm and no change in the FEM data. Finally, the growth in maximum displacement from the experimental data from 86% of the experimental buckling load to just before buckling was 0.45 mm as, and 0.36 mm as output by the FEM. The growth of inward deformations as seen in the experimental data was -0.10 mm, and the FEM was -0.04 mm. These subtle changes between load levels are averaged out if one compares the outward radial displacement at 21% of the experimental buckling load and just prior to buckling for the experimental data and the FEM data which is 1.21 mm for both. The overall magnitudes of the radial displacements were not consistent between the experimental data and FEM data, but the overall growth of radial deformations between load steps is similar.

The buckling initiation and post buckling response were recorded with 4-pairs of high-speed cameras with a capture rate of 20,000 frames per second. The buckling propagation can be observed in a series of images from the first high-speed image through 16.3 milliseconds after the first image was taken (Figure 2.21a - Figure 2.21d). Buckling initiated at a dimple centered at about the 200-degree circumferential location with an inward radial deformation of -3.10 mm, as seen Figure 2.21a. According to the images, it took approximately 7.3 milliseconds for the buckling to fully propagate around the circumference of the test article, as shown in Figure 2.21a - Figure 2.21c. In the 7.3 milliseconds from Figure 2.21a - Figure 2.21c, the buckling initiation dimple went from -3.10 mm to -33.25 mm of radial deformation. The pattern observed in Figure 2.21b consists of two axial half waves and seven circumferential full waves. Then the postbuckling pattern transitioned from seven to six circumferential half-waves, Figure 2.21d. As the pattern evolved, the radial displacements grew significantly. The postbuckled equilibrium radial deformation determined from analysis (Figure 2.22) was seven circumferential waves and two axial half-waves, one circumferential wave more than in the final high-speed image (Figure 2.21d).

Posttest inspection of the test article revealed a shallow delamination that was observed approximately at midheight and a circumferential location of 170 degrees. The delamination was approximately 152 mm in length and 51 mm in width as indicated by the red outline in Figure 2.23. The delamination is believed to have occurred during the dynamic buckling event at an inflection point between the inward dimple where buckling initiated and the adjacent outward dimple as seen in Figure 2.21a. The angle of the delamination is +23-degrees, which is the angle of the outer most ply. The difference between the predicted and observed postbuckling behavior may be attributed to the delamination. The delamination caused a localized stiffness differential that was not accounted for in the FEM. Though NDL-1 was designed to fail in buckling, this should be confirmed especially with the damage observed after failure. The axial strain and hoop strain at the failure location derived from DIC is plotted in Figure 2.24a and Figure 2.24b. The axial strain in the center of the dimple, where buckling initiated, was -2617 $\mu\varepsilon$ at the buckling load. The hoop strain in the center of dimple, where buckling initiated, was 860 $\mu\varepsilon$ at buckling. These values are significantly less than the calculated compressive failure strain of -12,280 $\mu\varepsilon$ and tensile strain of 6584 $\mu\varepsilon$ (2.2). Based on maximum strain criterion, it is concluded that the test article failed in buckling rather than due to strength failure.

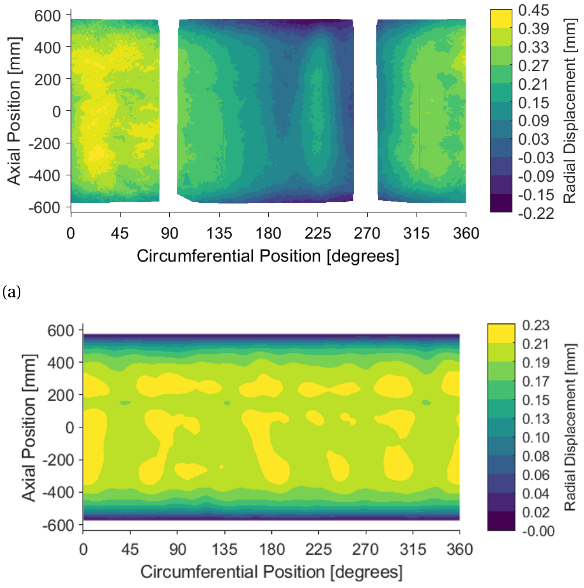

(a)

(b)

Figure 2.16: Radial displacement at 21% of the experimental buckling load: a) Experimental data ; b) FEM data

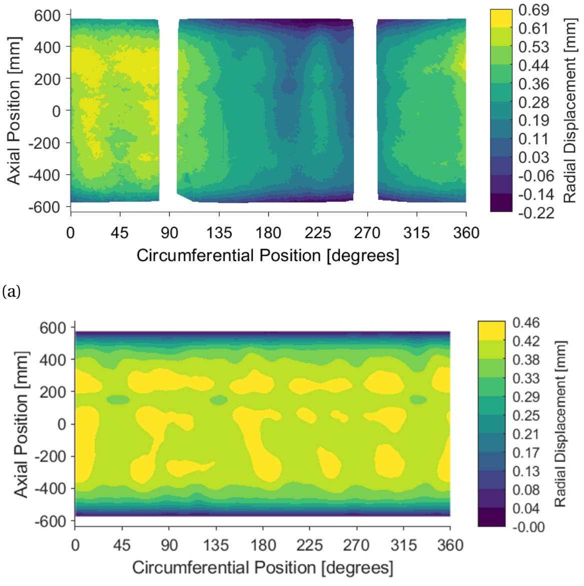

(a)

(b)

Figure 2.17: Radial displacement at 43% of the experimental buckling load: a) Experimental data ; b) FEM data

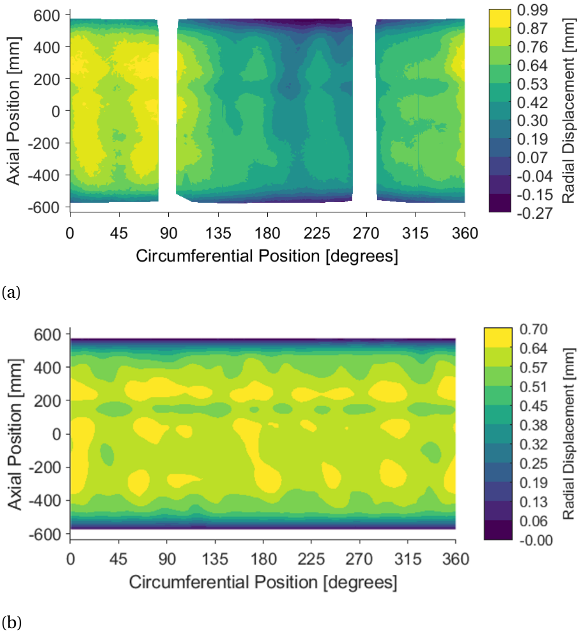

(a)

(b)

Figure 2.18: Radial displacement at 64% of the experimental buckling load: a) Experimental data ; b) FEM data

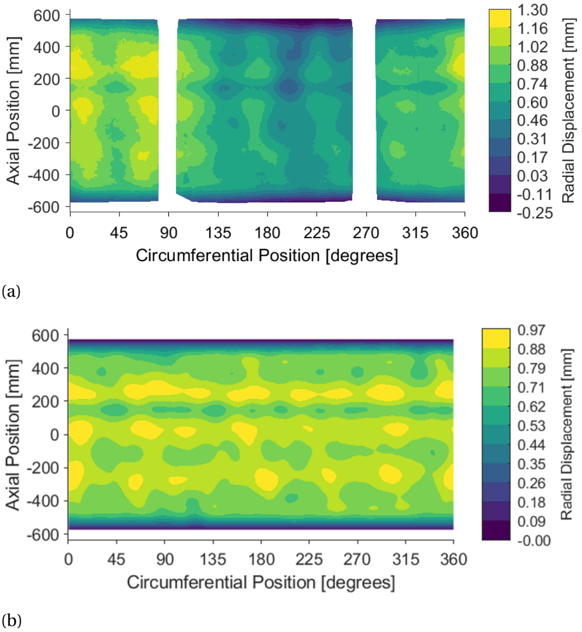

(a)

(b)

Figure 2.19: Radial displacement at 86% of the experimental buckling load: a) Experimental data ; b) FEM data

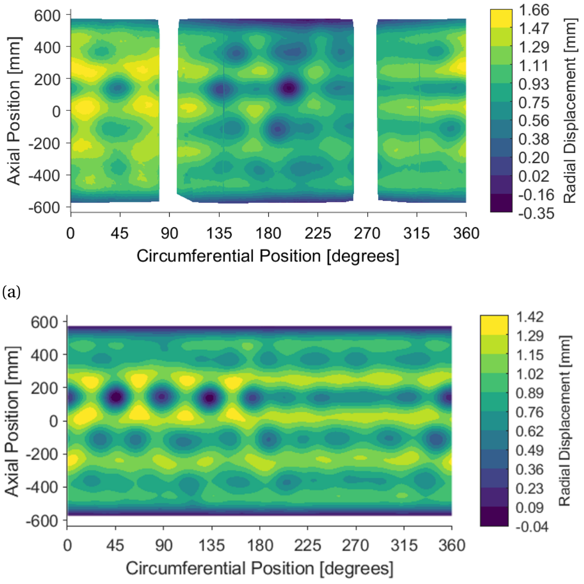

(a)

(b)

Figure 2.20: Radial displacement immediately prior to the experimental peak load: a) Experimental data ; b) FEM data

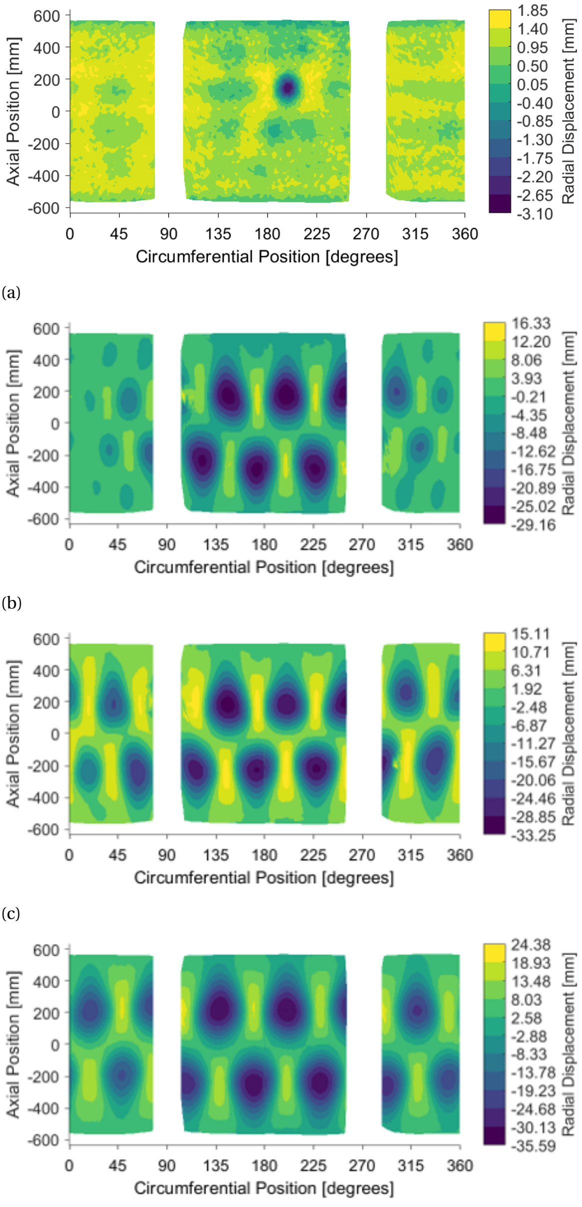

(a)

(b)

(c)

(d)

Figure 2.21: Buckling propagation measured by high-speed camera: a) First high-speed image ; b) 5.1 milliseconds after first image; c) 7.3 milliseconds after first image; d) 16.3 milliseconds after first image

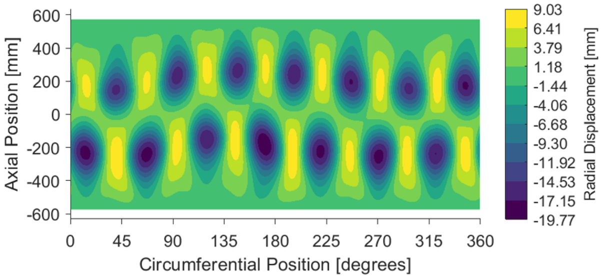

Figure 2.22: Predicted postbuckled radial deformation from analysis.

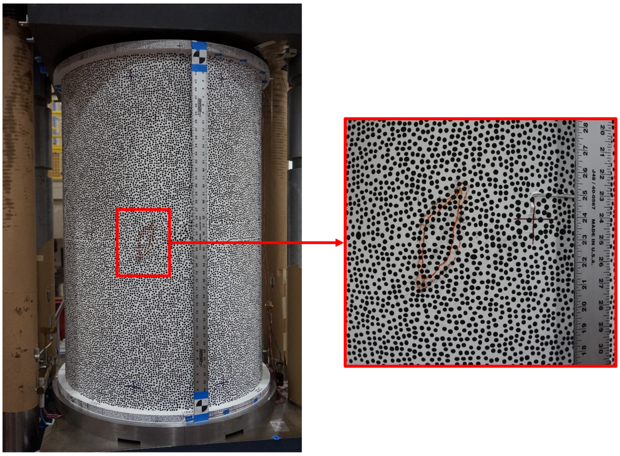

Figure 2.23: NDL-1 damage.

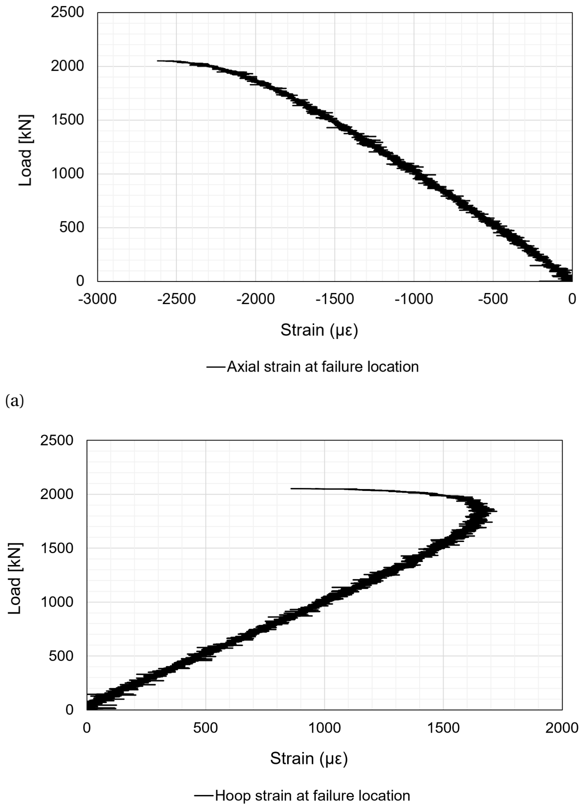

(a)

(b)

Figure 2.24: DIC derived strains in the center of the buckling initiation location: a) Axial strain ; b) Hoop strain.

2.6.2. POSTTEST MODEL CORRELATION

While the correlation between the pretest prediction model and the test data was very good, specifically the stiffness and predicted buckling load being within 1%, an additional posttest investigation was completed to determine other variables that may have affected the predicted buckling initiation site. A significant amount of data has been collected on the as-built configuration of NDL-1, such as radial imperfections, thickness variations and shell-end imperfections. There are other possible sources of variation that could not be quantified prior to test. For example, this may include nonuniform loading due to the test frame.

The axial displacements measured just prior to buckling derived from the DIC data at 45, 135, 225, and 315 degrees yielded that the axial displacement at these locations varied from 2.17 mm to 2.21 mm. From these values, a best-fit plane showed a slight tilt toward the 151-degree circumferential position with an associated maximum axial displacement of 0.021 mm at the shell edge. This corresponds to a rotation of 0.003 degrees of the best-fit plane towards the 151-degree circumferential location. To account for this in the FEM, the top reference node was rotated to 0.003 degree from 0 degree linearly over the course of the aforementioned initial prebuckling step, along with the original imposed axial displacement. The rotation was then held constant at 0.003 degree through and after buckling.

The inclusion of the load imperfection changed the buckling load and predicted buckling initiation site. As a result of the tilt, the predicted buckling load was reduced from 2075 kN to 2061 kN. Recall that the experimental load was 2074 kN, which means the adjustment did not improve the prediction of the buckling load with respect to the experimental load. The radial deformations between the models with and without the tilt show a similar global pattern, but the predicted dimple location changed. In the pretest predictions, Figure 2.20b, four distinct dimples were centered about the +150 mm axial position starting from 0-degree circumferential position and repeating every 45-degrees with the last dimple at 135-degrees. The prebuckling pattern from the model with the plane-tilt model is similar, but a single, more prominent dimple formed in the same axial position at 135 degrees, Figure 2.25. The predicted buckling initiation site was at the same axial position as the two analyses, but the model still was not able to predict the experimental buckling initiation site centered at 200 degrees.

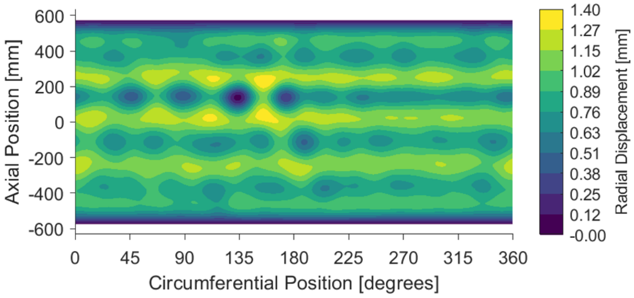

Figure 2.25: Radial displacement just prior to buckling with loading imperfection.

The load imperfection included in the posttest analysis did not resolve the discrepancy in the radial deformations. One possible explanation for the difference in radial deformation may possibly be attributed to the change in the radial geometric imperfections of the test article from when it was measured after manufacturing, as-manufactured imperfections, to when it was installed in the load frame, as-installed imperfections. It has been shown (References [23] and [24]) that significant changes in the predicted buckling behavior may be found when the as-installed imperfections were included in the FEMs and compared with the predicted behavior when the as-manufactured (before installation in the test facility) imperfections were included in the FEMs. The full shape of NDL-1 could not be measured in the test frame because the test-frame posts prevented access to sections of the test article.

2.7. CONCLUSION

Validated finite element models are important for designing buckling-critical launch-vehicle structures, and have been used in the past to perform sensitivity studies and develop new buckling knockdown factor approaches to reduce the mass of launch vehicle components. The objective of this work was to demonstrate that the scaling methodology was successful in determining a design that would ensure buckling prior to material failure, and to present a modeling methodology to successfully predict the buckling behavior of a scaled, launch-vehicle-like composite cylinder called NDL-1. The finite element modeling approach presented was validated experimentally. The model parameters, the inclusion of as-built details, test and analysis correlation, and a posttest investigation were discussed.

The model parameter study conducted prior to testing was used to determine that the SC8R element performed similarly to the S4R element in analyzing the buckling behavior of a composite cylindrical shell. It was also determined, that while the 10-mm element size was acceptable, a smaller mesh size of 5 mm would better capture NDL1's imperfection signature measured by structured light scanning, including a prominent feature on the mandrel that transferred to the cylinder during fabrication. The model included features such as measured radial imperfections, thickness imperfections, and shell-end imperfections. In addition, laminate coupon testing was used to develop finite element model lamina properties to best characterize the laminate stiffness.

The results of the finite element model (FEM) correlated well with the experimental results. The FEM-predicted buckling load was within 0.04% of the experimental buckling load and the predicted stiffness was within 1% of the experimentally measured stiffness. It is speculated that details such as the as-installed imperfection shape could have influenced the shape and magnitudes of the radial deformations. While the magnitudes were quite different, the rate of change of the inward and outward deformation was similar between the finite element model and test. Buckling did initiate in the test at the same axial location as predicted with the FEM, which corresponded to the localized mandrel feature. However, the circumferential location of the buckling initiation site was different between the prediction and test. It was shown with posttest test-analysis correlation that the circumferential buckling initiation site was sensitive to sources of nonuniform loading. The experimental postbuckling behavior was similar to that of the FEM, but damage that occurred during the buckling event may have influenced the experimental postbuckling behavior. Damage was not considered in the FEA, and this discrepancy was deemed a potential source of deviation in postbuckling observations between test and FEM.

The finite element model presented was shown to produce accurate predictions for the buckling load and stiffness of the scaled, launch-vehicle-like composite shell. The predicted prebuckling, incipient buckling, and postbuckling radial deformations had elements of agreement when compared to the measured radial deformations. Therefore, it is suggested that a similar modeling approach can be employed for other large-scale composite cylindrical shell structures.

3

ANALYSIS AND TESTING OF A LAUNCH-VEHICLE-LIKE COMPOSITE CONICAL-CYLINDRICAL SHELL

LAUNCH-VEHICLE shell structures, which can be composed of both cylindrical and conical sections, are known to be susceptible to buckling due to their large radius-to-thickness ratios. Advancements in composite manufacturing and numerical methods have enabled designers to consider more nontraditional shapes, such as connecting the conical and cylindrical sections with a toroidal transition to create a single-piece conical-cylindrical shell. This single-piece construction eliminates the need for a stiff, heavy interface ring between sections and has the potential to reduce mass. To better understand the buckling behavior of a composite conical-cylindrical shell, a lab-scale article was designed, fabricated, and tested. A finite element model of the test article, which included the actual thickness variations and radial imperfections, was created prior to test. The test article buckled elastically at 251.8 kN, approximately 8.8% higher than the predicted buckling load of 231.4 kN. Because the test article buckled elastically, the buckling test was repeated. The measured buckling load from the second test was within 1% of the first. Continued research in conical-cylindrical structures has the potential to expand the design space for launch-vehicle structures and lead to improved designs and reduce mass.

This chapter has been adapted from Rudd MT, Schultz MR, Bisagni C, Buckling behavior of Conical- Cylindrical Shells and "Design Considerations for Launch-Vehicle Structures," AIAA Scitech Forum 2024, AIAA Paper 2024-0034 and Rudd MT, Schultz MR, Bisagni C, “Analysis and testing of a launch-vehicle-like composite conical-cylindrical shell”, AIAA Journal, vol. 62, no. 9, pp. 3526–3543, 2024.

3.1. INTRODUCTION

Launch-vehicle designs based on traditional manufacturing methods typically use heavy circumferential rings to join conical and cylindrical structures. Advances in composite manufacturing, such as automated fiber placement (AFP), and numerical tools, such as high-performance finite element codes, enable aerospace engineers to consider alternative designs. These designs may include the combination of conical and cylindrical components to create a unitized conical-cylindrical shell with a toroidal transition for launch-vehicle structures and payload adapters. This unitized configuration would eliminate the need for interface rings, and can potentially lead to significant mass savings. Examples of this type of unitized construction are the SLS Universal Stage Adapter (USA), which is currently under development, the Système de Lancement Double Ariane (Sylda) on the Ariane 5, and Vega Secondary Payload Adapter.

Empirically-based design factors, or knockdown factors, are often used to ensure adequate margin to prevent global buckling. Such empirically-based buckling knockdown factors for cylinders are published in NASA SP-8007 [6] along with recommendations for developing analysis-based knockdown factors. NASA SP-8007 was originally published in 1965 and much of the experimental data presented was based on experimental results from as early as the 1920s with little or no data from composite shells. Researchers widely agree that current design parameters are often excessively conservative, motivating efforts to investigate the buckling behavior of composite cylindrical shells in launch-vehicle applications to reduce mass. For example, Hilburger and Starnes [34] used high-fidelity models to predict the buckling response of composite shells to better understand the sensitivities of these structures to geometric imperfection because the current guidelines were known to be overly conservative. More recently, Takano, et al. [35], tested composite cylindrical shells with a large radius-to-thickness ratio. The published experimental results for composite cylinders had only extended to a radius-to-thickness ratio of 500, while Takano, et al. [35] tested shells with a ratio equal to 848. Rudd, et al. also tested a composite cylindrical shell and developed a high-fidelity finite element model (FEM) including geometric imperfections to predict the buckling and post-buckling behavior to validate a numerical methodology with application to the design of launch vehicles as reported in [36] and Chapter 2. Also, Hartwich, et al. [37] published experimental data about how different manufacturing methods and boundary conditions can affect the buckling results of composite shells. Wagner, et al. [38] have also contributed to the body of knowledge pertaining to the buckling of composite cylinders to improve the designs of launch vehicle structures by suggesting approaches to determine lower-bound knockdown factors [38].

The European Union and NASA have launched major initiatives to reduce excessive conservatism in buckling design guidelines [39]. In 2012 the New Robust DESIgn Guideline for Imperfection Sensitive COmposite Launcher Structures (DESICOS) project was established. A goal of the DESICOS project was to determine analysis methods to confidently provide less conservative, lower-bound knockdown factors for the design of composite cylindrical launch-vehicle structures. The DESICOS researchers used analytical, numerical, experimental, and probabilistic techniques. The NASA Shell Buckling Knockdown Factor project has published a series of papers documenting the test and analysis of 2.4-m-diameter composite sandwich cylindrical shells with the intent to help define a modeling methodology to develop design-specific knockdown factors for composite sandwich cylindrical shells [26, 27, 28]. In summary, researchers have cited the need to further investigate the buckling behavior of composite cylindrical shells to improve the design of these structures for aerospace applications.

A reasoning similar to the one indicated above drives the investigation of composite cones. A monograph with design recommendations for the buckling of thin-walled conical shells, NASA SP-8019 [5], was published shortly after NASA SP-8007. NASA SP-8019 recommends using a buckling knockdown factor of 0.33 for thin-walled conical shells, and has similar shortcomings as NASA SP-8007. The guidance given in SP-8019 was based on much less data than the guidance in SP-8007 for cylindrical shells. Therefore, researchers have started building a knowledge base for the buckling of conical shells that is similar to cylindrical shells. For example, Tong [40] published experimental results on the buckling of nine carbon-fiber-reinforced-plastic and nine glass-fiber-reinforced-plastic conical shells with the aim of adding to the limited amount of research available at that time. Goldfeld and Arbocz [41] studied the imperfection sensitivity of laminated conical shells. Khakimova, et al.'s [42], developed high-fidelity FEMs to predict the buckling behavior of three carbon-fiber-reinforced-polymer conical shells; these FEMs included features such as midsurface radial imperfections and thickness data. The goal of Khakimova, et al. [43] research was to address the fact that composite materials were not included when developing NASA SP-8019. In support of the DESICOS project, Ambrovich, et al. [44], tested two cylindrical and two conical shells. More recently, Sleight, et al. [45] documented the results from an imperfection sensitivity study for conical sandwich-composite structures for launch vehicle . One of the main objectives for each of the cited papers is to address the need for more research for buckling critical composite conical shells to improve future launch vehicle and payload adapter designs.

The buckling behavior of conical-cylindrical shells has been studied by researchers using numerical and semi-analytical methods, but the research was primarily aimed at civil engineering and piping applications. Wunderluich, et al. [46], developed a semi-analytical approach to perform a nonlinear static and dynamic analysis of isotropic pressure vessels. In their research, Wunderluich, et al. [46] investigated toriconical shells, meaning either a conical or spherical end, connected to a cylindrical base with a toroidal segment between. Anwen [47] published a paper on the buckling of a conical-cylindrical structure with a toroidal transition segment, but assumed isotropic material properties and only considered external pressure loading. To date, Patel, et al. [48], and Singh and Patel [49] have published research on the buckling and post-buckling characteristics of composite conical-cylindrical shells subjected to torsion, external pressure, axial compression, and thermal loading. Interrogated in their research were the effects of layup, cone angle, and axisymmetric imperfections, but they did not consider a toroidal transition, and the boundary conditions assumed were more in line with the civil engineering and piping applications. Zarei and Rahimi [50] published a study regarding the buckling resistance of joined composite conical-cylindrical shells, but again toroidal transitions were not considered, and they focused on lateral pressure loading.

Minimal experimental data has been published for conical-cylindrical structures, and the majority of the data is related to metallic structures. Hu and Raney [51] tested a metallic conical-cylindrical shell to validate their analytical models for vibration response, but not global buckling. Bushnell and Galletly [52] and Zhao [53] tested to failure structures similar to those of Hu and Raney [51] under internal pressure to validate finite element methodologies. Chronopoulos, et al. [54], developed a numerical model to predict the vibroacoustic response of a composite conical-cylindrical-conical shell, which was a scaled-down Sylda on the Ariane 5.

More generally, the conical-cylindrical shell shape can be classified as a shell of revolution or shell with variable curvatures. There have been a numerous publications dedicated to numerical and analytical methods to determine the buckling load of shells of revolutions and shells of variable curvature. For example, Marguerre [55] published a NASA technical memorandum on the stability of variable curvature shells. Also, a series of NASA contractor reports with analysis methods for stress and stability for shells of revolution were published where the imperfection sensitivity under external pressure was studied (see [56, 57, 58]), and though the structural application is different, the geometry is similar. Also, Tornabene and Viola [59] and Tornabene, et al. [60], researched the response of functionally graded doubly-curved shells, specifically, the static response and free vibration. More recently, Zingoni and Enoma [61] studied the strength and stability of spherical-conical shells, which would be pressurized and used in underwater applications.

The common goal for research published to date on the buckling behavior of composite cylindrical and conical shells is addressing the lack of data available for these structures by publishing numerical and experimental test results. It has been realized that this data is vital to improve launch-vehicle and payload adapter designs. The application of unitized composite conical-cylindrical shells has potential to improve the mass efficiency of launch-vehicle primary and secondary structures by eliminating the need for the heavy interface rings that traditionally join the cylindrical and conical portions. To make this unitized conical-cylindrical shape a common design solution, it is necessary to have experimental data on the buckling of composite conical-cylindrical shells. Therefore, a composite conical-cylindrical shell was designed, built, and tested in axial compression until buckling failure with the objective of influencing and improving the designs of future aerospace structures.

A numerical study investigating the buckling behavior and imperfection sensitivity of a conical, cylindrical, and combined conical-cylindrical shell is presented in Section 3.2.The results of the numerical studies informed the layup and geometry of a composite conical-cylindrical shell test article, which was designed to fail in buckling. The corelation of the test data and analysis is discussed in detail in Section 3.3.The results are summarized in Section 3.4.

3.2. NUMERICAL STUDY ON THE BUCKLING BEHAVIOR OF A CONICAL, CYLINDRICAL, AND CONICAL-CYLINDRICAL SHELL

The linear and nonlinear analyses were completed using the general-purpose finite element software, Abaqus [62]. A mesh convergence study was used to determine that a mesh element size of approximately 5 mm with the four-node reduced-integration shell element (S4R) was sufficient to capture the buckling behavior for all geometries presented. The Lanczos solver was utilized for the eigenvalue analyses and an implicit dynamic nonlinear solver was used to capture the prebuckling and buckling behavior in the nonlinear analyses. The top and bottom edges of the shells had all degrees of freedom fixed, except for the translational degree of freedom at the top edge, which allowed for axial displacement.

An aluminum alloy cone with a semi-vertex angle of 15 degrees, a centerline radius of 400 mm, a height of 600 mm, and a wall thickness of 1.43 mm was considered, as shown in Figure 3.1a. The critical buckling load, obtained as the lowest eigenvalue of the buckling equation for the geometry with an elastic modulus of 71.0 GPa and a Poisson's ratio of 0.33, was 542.4 kN. The eigenmode shape associated to the lowest eigenvalue is presented in Figure 3.1b. Eigenvalue analyses are relatively inexpensive from a computational point of view, but a computationally intensive geometrically nonlinear analysis can provide a better understanding of the buckling behavior of thin-walled shell structures. The predicted nonlinear buckling load of the isotropic cone geometry was 497.8 kN. That is, the influence of the geometrically nonlinear response reduced the buckling load by 8% as compared to the eigenvalue analysis (buckling equation). The predicted deformation shortly after buckling from the nonlinear analysis is shown in Figure 3.1c. The dark blue dimples at the small diameter end of the cone indicate where buckling initiated.

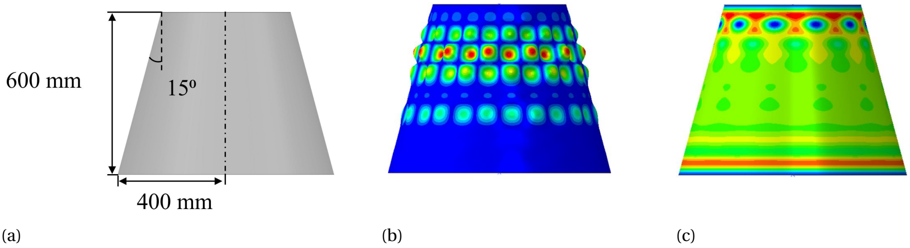

Figure 3.1: Conical shell: a) geometry; b) first eigenmode; c) radial deformation immediately after buckling.

The analysis procedure described above was repeated for a cylindrical shell with the same height of 600 mm, the same radius of 400 mm and the same material as shown in Figure 3.2a. The first (lowest) eigenvalue was predicted to be 581.5 kN, and the corresponding first eigenmode is presented in Figure 3.2b. The geometrically nonlinear buckling load was predicted to be 536.8 kN. The inclusion of large rotations and displacements reduced the buckling load by approximately 8%, which is similar to the conical shell. Figure3.2c presents the radial deformations just after buckling from the nonlinear analysis and shows that buckling may occur at ends of the cylinder.

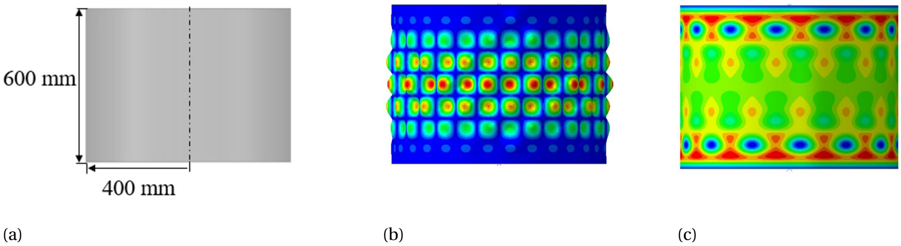

(a) (b) (c)

Figure 3.2: Cylindrical shell: a) geometry; b) first eigenmode;
c) radial deformation immediately after buckling.

To create the conical-cylindrical shell for this study, the cone and cylinder geometries presented above were stacked on top of one another and combined, Figure 3.3a. The eigenvalue for this conical-cylindrical shell corresponds to a linear buckling load of 516.8 kN and the associated eigenmode is presented in Figure 3.3b. The geometrically nonlinear buckling load was 261.5 kN, which is approximately 50% of the buckling load computed from the eigenvalue. This reduction is much greater than the reduction observed for the individual cone and cylinder components. The radial deformations immediately after buckling for the conical-cylindrical shell in Figure 3.3c shows that buckling initiated near the junction between the cone and cylinder.

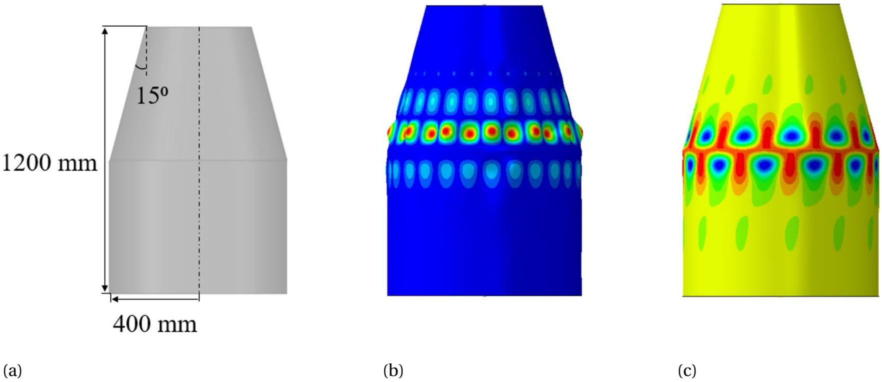

(a) (b) (c)

Figure 3.3: Conical-cylindrical shell: a) geometry; b) first eigenmode;
c) radial deformation immediately after buckling.

Since it is well known that the difference between test and analysis for conical and cylindrical shells can be largely attributed to the presence of radial imperfections, analyses were performed to understand whether conical-cylindrical shells share a similar sensitivity to radial imperfections. Using the geometry presented in Figure 3.3a, imperfection shapes of the first eigenmodes for the conical, cylindrical, and conical-cylindrical shell were used as the radial imperfection. The first eigenmode shapes were selected as the imperfection shape because the first eigenmode or weighted combinations of eigenmodes are commonly used in practice to assess the imperfection sensitivity of an aerospace shell structure. The eigenmode shapes are presented in Figure 3.1b, Figure 3.2b, and Figure 3.3b for the conical, cylindrical, and conical-cylindrical shells, respectively. The amplitude of the imperfection was chosen to be to 10% of the 1.43 mm thickness.

The KDFs given in NASA SP-8007 and NASA SP-8019 are scaling factors ranging between values as low as 0.2 up to a maximum of 1. These scaling factors relate the idealized eigenvalue buckling loads to the recommended buckling design loads. The KDFs recommended are the lower-bound recommendation based on a series of experimental tests that were normalized by the eigenvalue buckling load of a structure without imperfections.

In order to relate the results of the present study with the KDFs in NASA SP-8007 and NASA SP-8019, a quantity similar to the KDF, and referred to as the *normalized buckling load*, is defined here as the ratio between a buckling load that accounts for nonlinear effects prior to buckling as well as structural imperfections, divided by the eigenvalue buckling load of an ideal structure. The numerically-predicted geometrically-nonlinear buckling load with imperfections plays a role similar to the experimentally-obtained buckling loads in the NASA KDF. From this point of view, the normalized buckling load can be directly compared with the KDF even though they were obtained in different ways.

The load versus displacement curves for the conical, cylindrical, and conical-cylindrical shells obtained from a geometrically-nonlinear implicit quasi-static analysis are presented in Figure 3.4 for shells without imperfections (solid lines) and with imperfections (dashed lines). The values of the corresponding buckling load obtained as an eigenvalue of the buckling equation are shown as dotted lines. The dotted lines are extended over the horizontal axis to facilitate visual comparison with the peak value of the load-displacement curves. As can be observed in the figure, the buckling load obtained as an eigenvalue of the buckling equation without imperfections lies above the peak value of the geometrically-nonlinear response of a shell without imperfections. This difference can be ascribed to the fact that the prebuckled state used in the buckling equation is obtained from a geometrically linear analysis.

The normalized buckling load for the imperfect cone, computed as the buckling load from the nonlinear analysis with imperfections, 288.0 kN, divided by the eigenvalue buckling load, 542.4 kN, is equal to 0.53. The normalized buckling load for the cylinder with imperfections is 310.0 kN divided by the eigenvalue buckling load 581.5 kN, is equal to 0.53. The conical shell and cylindrical shell have the same normalized buckling loads up to the second decimal. However, the nonlinear buckling load with imperfections for the conical-cylindrical shell was 221.6 kN, which results in a normalized buckling load of 0.43.

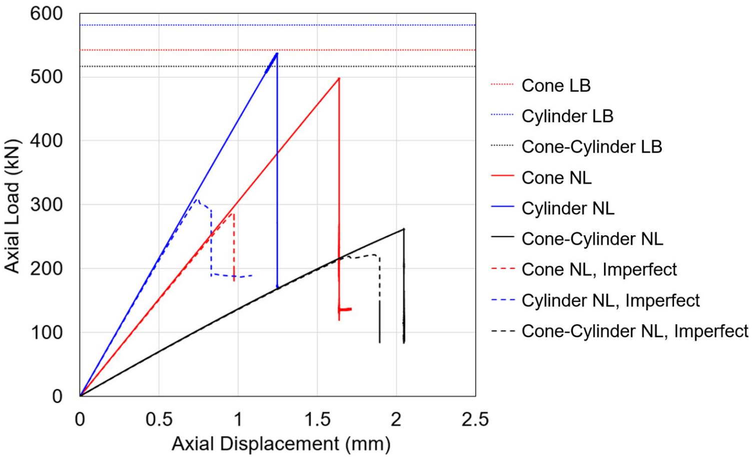

Figure 3.4: Axial compressive load as a function of the axial compressive displacement of isotropic conical, cylindrical, and conical-cylindrical shells obtained from an implicit geometrically-nonlinear analysis (NL) for shells with and without imperfections (dashed and solid lines, respectively). For comparison purposes, the eigenvalue buckling load (LB) is shown as a dotted line extended over the loading range.

The results of these nonlinear analyses of imperfect shells confirm that the presence of radial imperfections can significantly reduce the buckling capability for the conical and cylindrical shells. The inclusion of the eigenmode imperfection decreased the predicted buckling load by 42% for the cone and cylinder, which is significant compared the 8% reduction in load due to the effects associated to geometric nonlinearities for the cone and cylinder. These results contrast with the findings from the conical-cylindrical shell where the presence of radial imperfections reduced the buckling by only 15%, which was less than the reduction the geometrically nonlinear effects of 49%. These results indicate that conical-cylindrical shells may not be as sensitive to geometric imperfections as conical and cylindrical shell components.

From the perspective of launch-vehicle design, the KDFs recommended by NASA SP-8007 and NASA SP-8019 for the conical and cylindrical shells being analyzed are 0.33 and 0.42, respectively. The normalized buckling loads for the conical and cylindrical shells were both 0.53. Comparing the normalized buckling loads of 0.53 to the recommended KDFs, NASA SP-8007 and 8019 could be considered conservative. On the other hand, the normalized buckling load for the conical-cylindrical shell of 0.43, may not be considered conservative when compared to the KDF recommended for the cylindrical shell. The conical shell KDF is still conservative.

To assess if the large difference between the eigenvalue and nonlinear analyses is specific to the combined conical-cylindrical shell geometry, similar analyses were repeated with a shell of the same dimensions with Hexcel's IM7/8552-1 carbon-epoxy material system [32]. A composite quasi-isotropic layup of $[45/\text{-}45/90/0]_S$ with the unidirectional carbon fiber tape material system was assumed in the analyses. In order to maintain the same radius-to-thickness ratio as the isotropic structure, the total laminate thickness was 1.43 mm, so each ply had a 0.173-mm thickness. A modulus of elasticity of 140.9 MPa in the fiber direction, a modulus of elasticity transverse to the fiber direction of 9.72 MPa, a shear modulus equal to 4.69 MPa, and an in-plane Poisson's ratio of 0.356 were used in the analyses.

An eigenvalue buckling analysis and a geometrically nonlinear analysis were completed, followed by a geometrically nonlinear analysis with imperfections. The eigenvalue buckling load for this structure was 330.8 kN and the associated eigenmode is shown in Figure 3.5a. The nonlinear buckling load for this configuration was 186.0 kN and the radial deformation shape at this load is in Figure 3.5b. As with the isotropic case, the first eigenmode was used as an imperfection and applied to the geometry with an amplitude 10% of the total laminate thickness. The predicted nonlinear buckling load with the imperfect geometry was also 186.0 kN, which results in a normalized buckling load of 0.56. The radial displacement shape at buckling is presented in Figure 3.5c. The addition of radial imperfections essentially had no effect on the buckling load for the composite conical-cylindrical shell, and it did not significantly influence the location of buckling initiation. The dark blue dimples, which represent inward dimples and buckling locations, are still around the conical-cylindrical junction in both Figure 3.5b and Figure 3.5c. In a manner similar to the isotropic analyses, the inclusion of nonlinear geometric effects had a greater influence on the buckling load than the inclusion of imperfections for this geometry. From comparison of the buckling predictions for the isotropic and composite conical-cylindrical shells, it would appear that the buckling behavior of conical-cylindrical shells is influenced more by the chosen geometry than the material system. Additionally, using the first eigenmode shape as the imperfection shape to determine the imperfection sensitivity may not be considered the most conservative approach since it did not affect the buckling load for the composite conical-cylindrical shell.

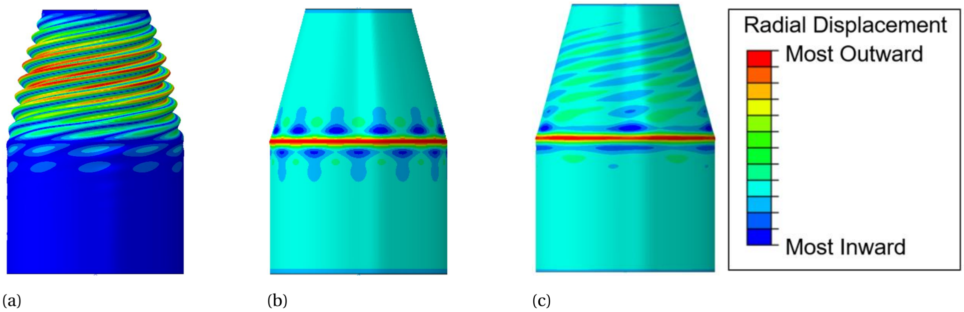

Figure 3.5: Composite conical-cylindrical shell radial displacement shapes: a) first eigenmode; b) at buckling without imperfections; c) at buckling with imperfections.

Since buckling initiates near the transition region for the configurations with and without imperfections for both isotropic and composite material systems, it would appear this region is important to the buckling response of conical-cylindrical shells. To investigate the importance of this region further, the radius of curvature between the conical and cylindrical shells was increased to create a more gradual transition between the components by creating a toroidal transition region as shown in Figure 6. The radius of curvature, ρ, for the geometry previously investigated was equal to 0 mm, Figure 3.6a.

Radii of curvatures of 200 mm, 400 mm, and 800 mm were also investigated, Figure 3.6b - Figure 3.6d. The radius of the cylinder was 400 mm, and the height was 1200 mm to be consistent with the previously considered geometry. Composite material properties were considered for the subsequent buckling analyses.

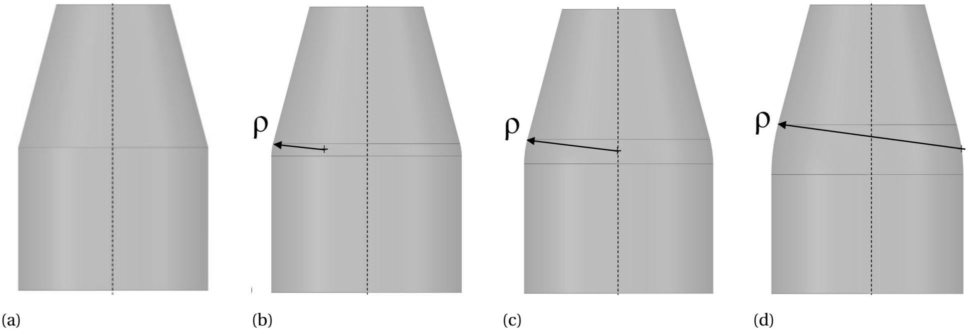

Figure 3.6: Geometry with different radii of curvatures: a) ρ = 0 mm; b) ρ = 200 mm; c) ρ = 400 mm; d) ρ = 800 mm.

The results for the eigenvalue and geometrically nonlinear quasi-static buckling analyses for the composite conical-cylindrical shells for each radius of curvature are presented in Table 3.1 and Figure 3.7. It can be observed in the table that as the transition between the cone and cylinder becomes more rounded, i.e., the radius of curvature increases, the eigenvalue buckling loads were essentially unchanged while the nonlinear buckling loads increased. It is postulated that, as the radius of curvature increases, there is a reduction in the large rotations and displacements that occur near the transition region, which makes the nonlinear buckling load in better agreement with the linear eigenvalue. A result of the large rotations near the transition region is a decreasing in stiffness with decreasing transition-region radius, which can be seen in Figure 3.7 as a decreasing slope of the nonlinear load-displacement curves with decreasing transition-region radius. In the following discussion, the configuration with the radius of curvature equal to 400 mm will be the baseline for comparison.

Table 3.1: The eigenvalue buckling loads and nonlinear buckling loads of a composite conical-cylindrical shell with different radii of curvatures.

Radius of curvature of transition region, ρ (mm)	Eigenvalue (kN)	Nonlinear (kN)
0	330.8	186.0
200	330.9	229.9
400	331.0	271.7
800	331.0	300.8

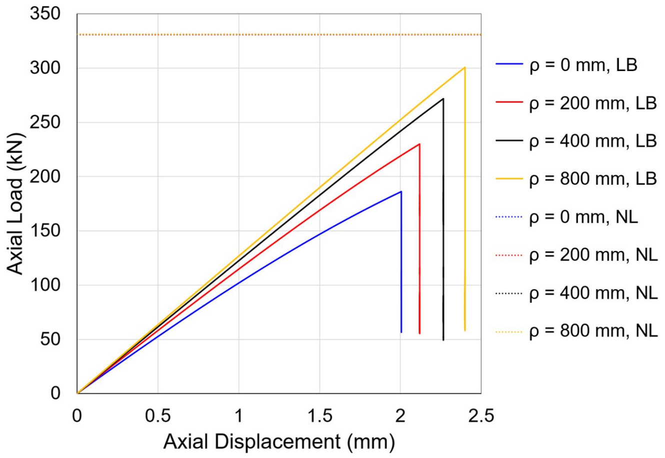

Figure 3.7: Eigenvalue buckling loads (LB, dotted lines) and nonlinear compressive axial load (NL, solid lines) as a function of the axial compression for composite conical-cylindrical shells with different radius of curvatures. The eigenvalue buckling loads are extended as (overlapping) dotted lines over the horizontal axis for visual comparison with the peak load of the non-linear response curves.

After the effect of the transition region on the buckling behavior was studied, an investigation of the imperfection sensitivity was completed. The composite conical-cylindrical shell with a radius of curvature of 400 mm was investigated and will be referred to as the baseline. The imperfection shape used was the first eigenmode, shown as Figure 3.8, since it is generally assumed that it will accelerate buckling by triggering the lowest buckling mode and, consequently, assess sensitivity to radial imperfections. Imperfection amplitudes equal to 10% and 20% of the wall thickness were considered. The values for the nonlinear buckling loads and normalized buckling loads are presented in Table 3.2. The compressive axial load versus compressive axial displacement curves are presented in Figure 3.9.

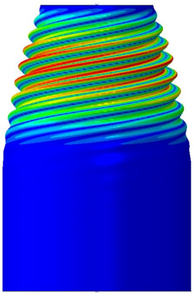

Figure 3.8: First eigenmode of a composite conical-cylindrical shell with $\rho = 400$ mm.

From Table 3.2 and Figure 3.9 it can be observed that the composite conical-cylindrical shell with a radius of curvature of 400 mm, baseline configuration, was more imperfection sensitive than with a radius of curvature of 0 mm. The nonlinear buckling load for the

Table 3.2: The eigenvalue and nonlinear buckling loads and normalized buckling load of a composite conical-cylindrical shell with different imperfection amplitudes.

Imperfection	Linear eigenvalue (kN)	Nonlinear (kN)	Normalized
Baseline	331.0	271.7	0.82
Eigenmode 10%	331.0	213.4	0.65
Eigenmode 20%	331.0	160.5	0.48

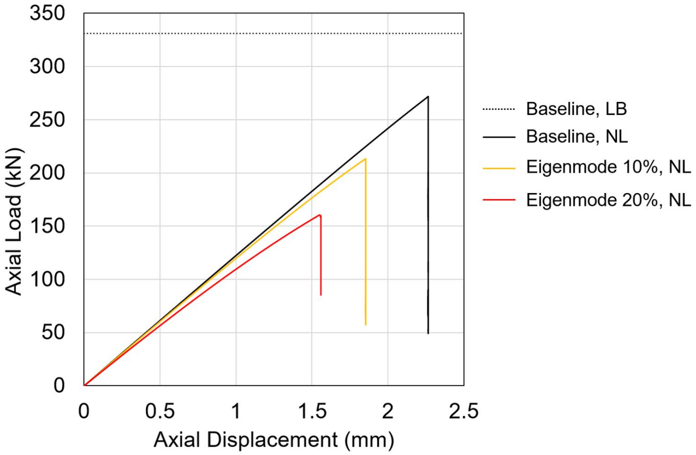

Figure 3.9: Eigenvalue buckling load (LB, dotted line) and nonlinear compressive axial load (NL, solid lines) as a function of the axial compression for composite conical-cylindrical shells with $\rho = 400$ mm without imperfections (baseline) and with imperfections (10% and 20% of the first eigenmode). The eigenvalue buckling load is extended as a dotted line over the horizontal axis for visual comparison with the peak load of the non-linear response curves.

baseline configuration without imperfections was 271.7 kN. The nonlinear buckling load with an imperfection amplitude of 10% was 213.4 kN. It was previously shown that, for no radius of curvature between the cone and cylinder components ($\rho = 0$ mm), the buckling load with imperfections was 186.0 kN and there was no reduction in load carrying capability when a same imperfection amplitude was included in the analysis. This suggests that, as the transition-region radius of curvature increases, the perfect-geometry buckling load increases, and so does the imperfection sensitivity. In addition, it should be noted that the normalized buckling load for the analyses with a 20% imperfection amplitude was 0.48. The orthotropic-cylinder KDF calculated using NASA-SP-8007 is 0.43, which may not be considered conservative.

3.3. EXPERIMENTAL VALIDATION OF THE BUCKLING BEHAVIOR OF A COMPOSITE CONICAL CYLINDRICAL SHELL

The numerical results provided interesting observations regarding the trade-offs between effects from geometric nonlinearities and imperfection sensitivity as a function of the radius of curvature, which needed to be validated experimentally. To achieve this, a composite conical-cylindrical shells similar to the Baseline design will be manufactured and tested.

3.3.1. TEST ARTICLE DESIGN AND MANUFACTURING

A composite conical-cylindrical shell test article, referred to herein as 3CHELL (Figure 3.10), was fabricated with Hexcel IM7/8552-1 (190 gsm) carbon fiber/epoxy system. The test-article geometry is an approximate scaled-down version of the SLS USA. The overall height (axial length) of 3CHELL is 762 mm. The cylindrical inner mold line (IML) diameter is 639 mm, and the IML diameter of the top of the conical shell is 418 mm. The conical shell has a 15-degree semi-vertex angle, α. The conical shell and cylindrical shell are combined with a seamless toroidal transition with a 380-mm radius of curvature.

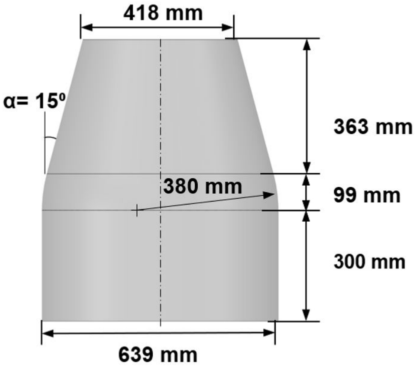

Figure 3.10: Test article geometry.

The test article was fabricated at the NASA Marshall Space Flight Center (MSFC) Composite Technology Center using the AFP robot. Unidirectional tows, 6.35-mm wide and nominally 0.183-mm thick, were laid on an aluminum mandrel that matched the inner mold line (IML) of the test article. The selected layup is quasi-isotropic with a nominal stacking sequence of $[45/\text{-}45/90/0]_S$ and a nominal laminate thickness of 1.46 mm, where 0 degrees is parallel to the axis of rotation and 90 degrees is perpendicular to the axis of rotation and tangential to the circular cross section of the shell at that axial position along the length of the shell. The positive ply angle is specified as clockwise from the 0-degree location when viewed from the outside. Figure 3.11 shows 3CHELL being manufactured at MSFC.

Figure 3.11: Test article being manufactured with the MSFC AFP robot.

The material properties for Hexcel IM7/8552-1 (190 gsm) were taken from data published by the National Institute for Aviation Research [32]. The lamina properties, such as elastic moduli and Poisson's ratio, are presented in Table 3.3. The B-basis laminate failure strength properties and laminate modulus for a layup with 25/50/25 proportion of 0-degree, 45-degree, and 90-degree plies are presented in the first two columns of Table 3.4. Failure strains were calculated from the laminate strength and modulus values assuming a linear elastic behavior and were used to design 3CHELL to have buckling occur prior to any strength failures under axial compression loading.

Table 3.3: Nominal lamina properties of Hexcel IM7/8552-1 composite.

0-degree modulus E_{11} (GPa)	90-degree modulus E_{22} (GPa)	Shear modulus G_{12} (GPa)	Poisson's ratio ν_{12} (-)
140.9	9.72	4.69	0.356

Table 3.4: Documented B-basis laminate failure stresses and calculated failure strains.

Test	Failure stress (MPa)	Modulus (GPa)	Calculated failure strain ($\mu\varepsilon$)
Unnotched tension	633.8	57.85	10,956
Unnotched compression	491.3	54.19	-9,065

After the test article was fabricated, the upper and lower edges were trimmed flat and parallel to an overall final height of 813 mm with a final trimmed weight of 3.40 kg. Following trimming, each end of the test article was potted in aluminum end rings with 25.4 mm-deep channels, leaving a free length of 762 mm. The test article was centered in the end rings and held in place with a ring of epoxy potting compound 8.0 mm wide on the outer mold line (OML) and 10.9 mm wide on the inner mold line (IML). The end rings were machined from an aluminum plate with an assumed modulus of elasticity of 71.01 GPa and Poisson's ratio of 0.33 [63]. The epoxy potting compound had an assumed modulus of elasticity of 7.58 GPa with an assumed Poisson's ratio of 0.33 [64]. The potted test article in the end rings is shown in Figure 3.12.

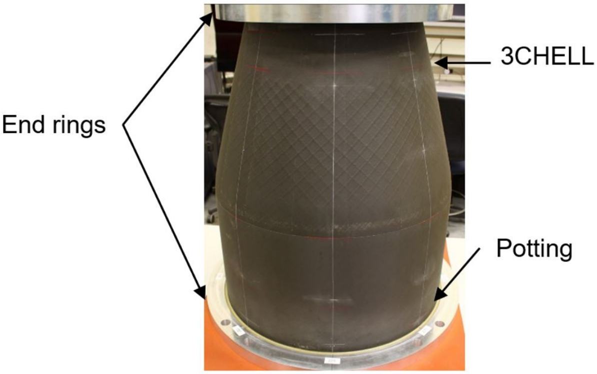

Figure 3.12: Test article potted in the end rings.

3.3.2. NONDESTRUCTIVE EVALUATION

Thermography and structured light scanning were two nondestructive evaluation techniques used to assess the construction quality of 3CHELL prior to testing. Thermography was used to interrogate the integrity of the test article. The purpose of structured light scanning was to collect data on the as-built test article to better understand how radial imperfections and thickness variations affect the buckling response.

THERMOGRAPHY

Flash thermography was used to inspect the composite shell for flaws. A pulse of light is aimed at an area of interest and thermal diffusivity can be determined. A flaw, or indication thereof, can be identified if there is a discontinuity in the thermal diffusivity in the area of interest. From this inspection, four areas of interest were noted in the cylindrical shell. The locations and sizes of the indications are given in Table 3.5. These areas were marked on 3CHELL to monitor during testing. Three of the four areas are located near the midheight of the cylinder, and the fourth is located near the cylinder end. No concerning areas were noted in the transition region or the conical section.

Table 3.5: Areas of interest identified with thermography.

Indication Number	Axial location from potted cylinder end (mm)	Circumferential location (degrees)	Approximate size (mm)
1	193	50°	8.0 × 5.0
2	188	93°	4.3 × 4.3
3	Encased in potting	210°	2.0 × 5.8
4	203	356°	13.5 × 6.4

STRUCTURED LIGHT SCANNING

Once 3CHELL was potted in the aluminum end rings, the geometries of the OML and IML were measured using structured light scanning, a photogrammetric technique [30]. The radial imperfections of the OML and IML are shown in Figure 3.13a, and the thickness calculated from the OML and IML data is shown in Figure 3.13b. The radial imperfections of the OML and IML ranged from a minimum inward radial deviation of 0.81 mm of the nominal surface to a maximum outward radial deviation of 1.01 mm of the nominal surface. The average thickness in the cylindrical and transition region of the shell was 1.37 mm. This would result in an average ply thickness of 0.171 mm, which is 6.5% less than the nominal ply thickness. In the conical section, a pattern of ±45-degree thickness variations that was due to tow overlaps is apparent. The overlapped region has a maximum thickness of 1.91 mm, and is the result of the AFP process to maintain a constant angle and the choice to eliminate gaps between each course. A tow drop occurred approximately 140 mm from the conical top end, which accounts for the thickness discontinuity in the conical shell section. The overlap patterns and the thickness discontinuity are also apparent in Figure 3.12.

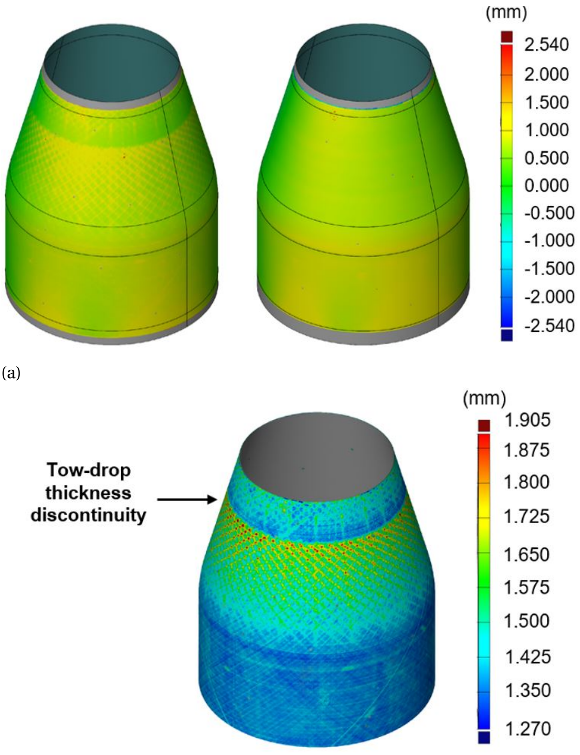

(a)

(b)

Figure 3.13: Structured light scan data of 3CHELL: a) Radial imperfections from OML (left) and IML (right); b) Measured thickness.

3.3.3. EXPERIMENTAL SETUP

The experimental setup was designed to capture the structural response, specifically the buckling behavior, of a composite conical-cylindrical shell under axial compression. The test article, 3CHELL, was highly instrumented and was subjected to several subcritical load sequences prior to the final load sequence to failure. These subcritical loads were 20% and 40% of the predicted 276.0-kN buckling load obtained from a geometrically nonlinear analysis (GNA) of the nominal test article with no radial or thickness imperfections. The final load case was to apply a compressive force on the 3CHELL test article up to buckling. Testing was performed at MSFC using a load frame that is capable of applying loads up to 1112 kN. A displacement-controlled compression rate of 0.076 mm/min was used for all load sequences. Numerous data-collection sensors such as strain gages, linear variable differential transformers (LVDTs), and low-speed and high-speed digital image correlation (DIC) systems were used to monitor the test article prebuckling, buckling, and postbuckling response throughout all load sequences. An overview of the test setup and a closeup-view of 3CHELL in the load frame can be seen in Figure 3.14.

Strain gage data were used to monitor the behavior of the test article in real time and for postprocessing. A series of 16 IML and 16 OML uniaxial strain gages, measuring axial strain, were placed back-to-back and spaced every 45 degrees. Half of those strain gages were located 25.4 mm from the top end ring, and the remaining half were positioned 25.4 mm from the bottom end ring. In addition, 24 back-to-back biaxial gages, measuring axial and hoop strains, were placed every 90 degrees at three different axial positions. The first set of biaxial gages were placed at the midheight of the cylindrical section, the second were placed near the center of the transition region, and the third were placed just above the tow drop in the conical section. A schematic of the strain gage layout is presented in Figure 3.15. The gages at the conical end, 25.4 mm from the end ring, are referred to as the cone-end gages. The gages 101 mm from the ring are referred to as the cone midheight gages. The gages at the transition region are referred to as transition gages. A similar naming convention is applied to the cylinder gages 137 mm from the cylinder end ring and 25.4 mm from the cylinder ring, which are referred to as the cylinder midheight and cylinder end gages, respectively.

Six pairs of low-speed DIC cameras (six low-speed 3D DIC systems) and two pairs of high-speed DIC cameras (two high-speed 3D DIC systems) were used to capture full-field displacements and strains. A top-down view of the DIC camera layout with approximate fields-of-view is shown in Figure 3.16. Of the low-speed DIC systems, the two systems centered about 0 and 180 degrees were used to measure the global behavior. Global refers to a field-of-view, approximately 711 mm x 864 mm, that includes the entire test article and end rings. The low-speed cameras had a capture rate of 1 Hz. Based on results obtained by the finite element analysis with perfect geometry, high strain gradients were expected at the transition region. Therefore, four low-speed local DIC systems were set up at 0, 90, 180, and 270 degrees, with a field of view to focus on the transition region between the conical and cylindrical sections. The fields of view of these local systems were approximately 297 mm x 365 mm. The local systems provided a higher resolution to measure the deformations and strains more accurately in this area of interest.

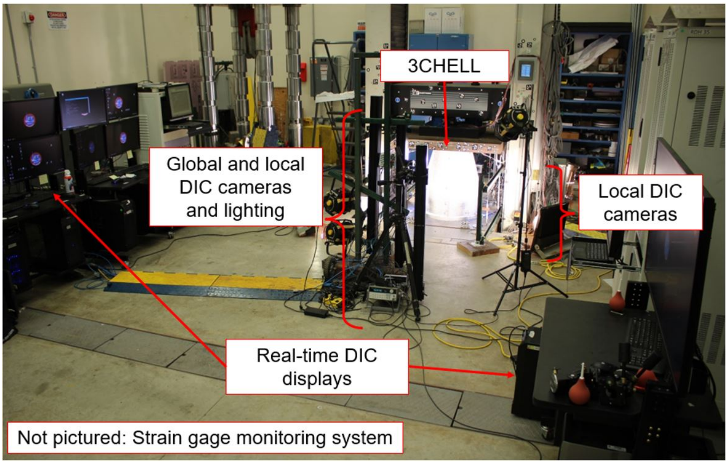

(a)

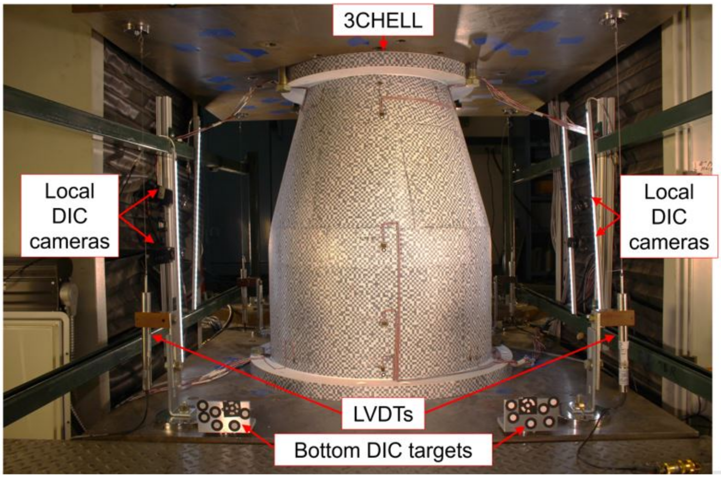

(b)

Figure 3.14: Test setup of 3CHELL: a) Overview of test setup; b) Close-up-view of 3CHELL in load frame.

The high-speed systems were also placed at 0 and 180 degrees with a similar global field-of-view and a frame rate of 10,000 Hz. The high-speed cameras were intended to capture the entire buckling event from just prior to buckling initiation (incipient) through buckling propagation and postbuckling. The image-capturing system was triggered by an operator shortly after buckling was detected, either audibly or visually, allowing to save all images approximately 2.5 seconds before the trigger was activated. This time interval covers the relevant transient states from initiation to postbuckling.

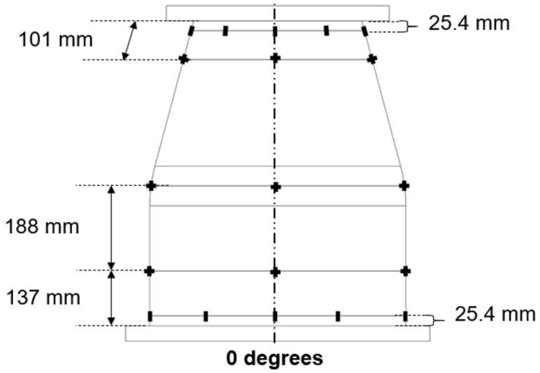

Figure 3.15: Strain gage layout.

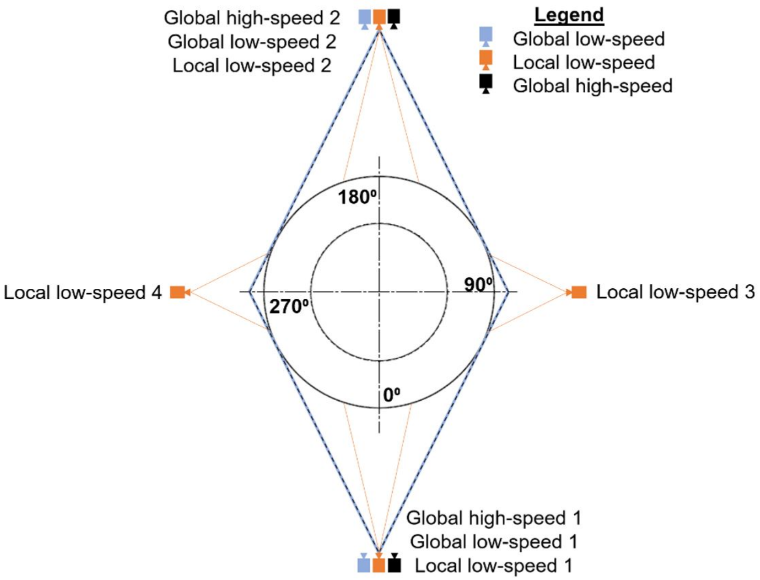

Figure 3.16: Top-down view of the DIC camera layout with approximate fields-of view.

The high-contrast speckle pattern for DIC accommodated both the low-speed (global and local) and the high-speed (global) photogrammetry requirements, which are based on camera resolution, acquisition rate, and field of view. A speckle size of 6.4 mm was utilized for the global systems, while a speckle size 1/10 of the global size was considered more appropriate for the local systems. To accommodate both speckle sizes in a single pattern, the entire test article was covered with a pattern similar to that shown in Figure 3.17, where it is seen that there is a two-tiered speckle pattern. The larger squares represent the speckle pattern that was utilized by the global systems, and the smaller squares within the larger squares represent the speckle pattern that was utilized by the local systems. The pattern was printed on transfer paper and then applied to the test article. This technique was first demonstrated by Bomarito, et al. [65, 66] on small specimens, and has also been applied to a large-scale buckling test [67].

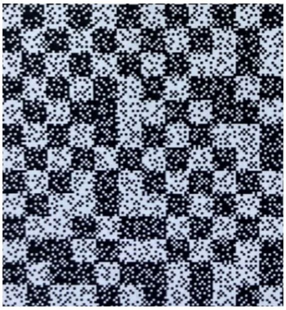

Figure 3.17: Example of the DIC speckle pattern for 3CHELL.

Four LVDTs were placed at the four corners of the load frame to measure relative axial displacements of the loading platens. To measure movement perpendicular to the loading direction, four targets were placed on the top and bottom corners of the load platens. These targets were monitored by a ninth DIC system to measure the movement of these points and can be seen in Figure 3.14.

3.3.4. RESULTS AND DISCUSSION

In this section, a description of the FEM used to predict the buckling response of 3CHELL is presented. A comparison of the test data to the predicted response is then provided. A discussion of the off-nominal loading observed during the test, and how this anomaly affected the predicted response, is presented next. Finally, the results of the repeated experimental buckling load sequence are presented. Results of the test article behavior at incipient buckling and postbuckling are discussed in detail.

FINITE ELEMENT MODEL AND ANALYSIS

A FEM of 3CHELL was created using Abaqus 2021 [62]. The four-node, reduced-integration shell element, S4R, was selected to characterize the solid laminate, potting compound, and end rings. The tow drop was not a specifically desired design feature, but instead was an artifact of the AFP manufacturing process where the changes in the shell geometry result in tow gaps and/or tow overlaps. During the shell design process, it was decided not to allow tow gaps, so changes in shell geometry resulted in tow overlaps. According to the measured thickness variation in Figure 3.13b, the laminate had areas where the thickness was almost 40% thicker than the acreage laminate thickness of 1.37 mm. Therefore, it was important to incorporate the tow-overlap and tow-drop features into the FEM. To discretely model the thickness variations of the ply overlaps, the equation of the fiber path for a constant angle on a conical surface, i.e.,

$$\Phi(l) = \tan(\phi) \ln\left[\frac{l}{l_0}\right] + \Phi_0 \tag{3.1}$$

was used [68]. In equation (3.1), Φ is the circumferential coordinate on an unrolled, flattened cone, ϕ is the nominal fiber angle, l_0 is the distance from the conical apex to the top edge of the cone which is derived from the small end radius,r_0, and l is the longitudinal surface coordinate on a flattened cone that can be calculated by the radius r. The flattened cone configuration and variables associated with equation (3.1) is presented in Figure 3.18.

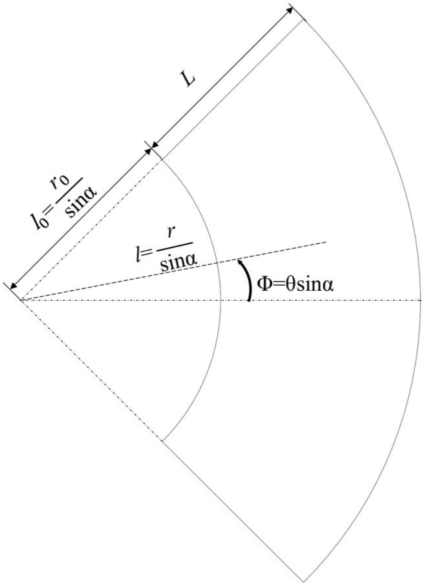

Figure 3.18: Flattened cone configuration.

The FEM with a detailed view of the thickness variations is presented in Figure 3.19. The cyan color represents the acreage or nominal layup, the light gray areas represent the end regions that are surrounded by the potting compound and end rings, the red color represents where two +45-degree plies overlap, the yellow color represents where two -45-degree plies overlap, and the dark blue region represents where the overlapped positive and negative 45-degree tows intersect. The positive X-axis of the FEM aligns with the 0-degree circumferential location, the positive Y-axis aligns with the 90-degree circumferential location, and Z-direction is defined along the axis of rotation.

During manufacturing, the amount of overlap in the +45 and -45 plies grew linearly as the diameter decreased until the point where one entire tow-width was overlapped, and a tow drop was instituted. The decision to section the overlapped area in the FEM into thirds (expanded section of Figure 3.19) was based on calculations comparing the density of various axial sections. The stacking sequences for the composite shell are given in Table 3.6, where the emboldened font indicates an overlapped ply.

Explicitly modeling the ply overlaps in the geometry made meshing complex. A mesh convergence study was used to determine that an approximate mesh size of 5 mm was appropriate to capture the buckling behavior of the composite conical-cylindrical test

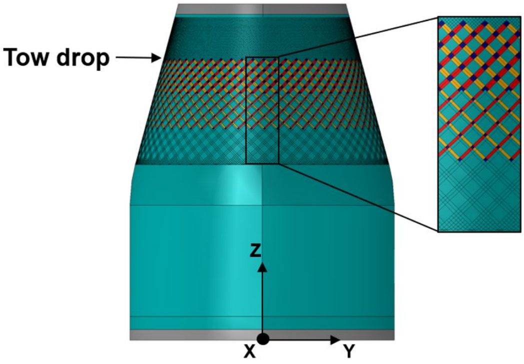

Figure 3.19: Finite element model with thickness-variation details.

Table 3.6: FEM Section Properties.

Section	FEM Color	Layup
Acreage	Cyan	[45/-45/90/0/0/90/-45/45]
+45 overlap	Red	[45/**45**/-45/90/0/0/90/-45/**45**/45]
-45 overlap	Yellow	[45/-45/**-45**/90/0/0/90/**-45**/-45/45]
+45 and -45 overlap	Dark blue	[45/**45**/-45/**-45**/90/0/0/90/**-45**/-45/**45**/45]
Potted ends	Gray	[Al ring/Potting/Acreage/Potting/Al ring]

article with a uniform mesh. An approximate mesh size of 3.8 mm was utilized herein because this finer mesh was necessary to incorporate the thickness variations.

After the model was meshed, the radial imperfections were incorporated. The IML structured light scan data was used as the source for the radial imperfections since the OML data had influences of the thickness variations. The process in which the radial imperfections were incorporated is explained by Kosztowny [69]. In addition, the measurement-derived average ply thickness of 0.171 mm was used in the FEM. The end-ring configuration in the test article was used to approximate a clamped boundary condition. To apply clamped boundary conditions, reference points were placed on the axis of rotation at the top and bottom and tie constraints were used to connect all degrees of freedom to the respective reference points. The bottom reference point had all degrees of freedom fixed, and the top reference point had all degrees of freedom fixed except for axial displacement.

Linear bifurcation analysis (LBA), vibration analysis, and implicit nonlinear transient analysis, referred to as GNA, were used to predict the structural response of 3CHELL. The Lanczos solver was used to determine the eigenvalues and corresponding eigenmodes. The critical (lowest) eigenvalue was 307.8 kN from the LBA. For vibrational analysis, proportional Rayleigh damping was assumed, with damping parameters A and B scaling the mass and stiffness matrices, respectively. To determine the damping parameters A

and B , the first natural frequency f from modal analysis was required. Assuming a modal damping ratio of $\xi = 0.05$, the corresponding damping coefficients were estimated as

$$A = 2\pi f \xi \tag{3.2}$$

and

$$B = \frac{\xi}{2\pi f} . \tag{3.3}$$

For the GNA, the time integrator parameter of -0.05 was used for slight numerical damping as suggested by [62]. The half increment solution parameter was set equal to the approximate buckling load of 3CHELL. The transient dynamic analysis used a time duration of 2000 seconds, with an initial time increment and a maximum increment of 1 second each. An applied displacement was ramped linearly from 0.00 mm to -2.54 mm at the top reference node to obtain the load rate of 0.076 mm/min that was used in the test. This was completed in a single analysis step. The GNA was performed for the structure with and without geometric imperfections. The GNA without imperfections resulted in a buckling load of 246.7 kN, which is approximately 20% less than the eigenvalue buckling load of 307.8 kN. The GNA with imperfections resulted in a buckling load of 235.1 kN, which is approximately 24% less than the linear eigenvalue buckling load. The inclusion of imperfections reduced the GNA buckling load by 5%. Table 3.7 includes a summary of the analyses and results. It should also be mentioned that the incorporation of the thickness variations increased the LBA load by 12%.

Table 3.7: Buckling load obtained from distinct types of analyses and incorporating distinct actual imperfections.

Analysis type	Radial imperfections (Y/N)	Thickness variations (Y/N)	Buckling load (kN)
LBA	N	Y	307.8
GNA	N	Y	246.7
GNA	Y	Y	235.1

The FEM included much of the variances from the nominal design such as the tow overlaps and radial imperfections. The goal was to create a high-fidelity FEM to predict the buckling response of a composite conical-cylindrical. From this, a validated modeling approach could be used in future analyses for developing buckling design guidelines for composite conical-cylindrical shell.

TEST-ANALYSIS CORRELATION

The test article 3CHELL buckled at a load of 251.8 kN, 7.1% greater than the predicted nonlinear buckling load with radial imperfections of 235.1 kN. The load versus displacement curves for the predicted and measured behavior are shown in Figure 3.20. The end-shortening data was determined using DIC by measuring the change in length between points on the top and bottom end rings. It is observed that the test article was approximately 14% stiffer than the FEM-predicted stiffness. There is also a notable change in slope that occurs around 50 kN. Additionally, the postbuckling equilibrium load predicted using the model was approximately 96.1 kN. The postbuckling equilibrium load during test was 96.6 kN.

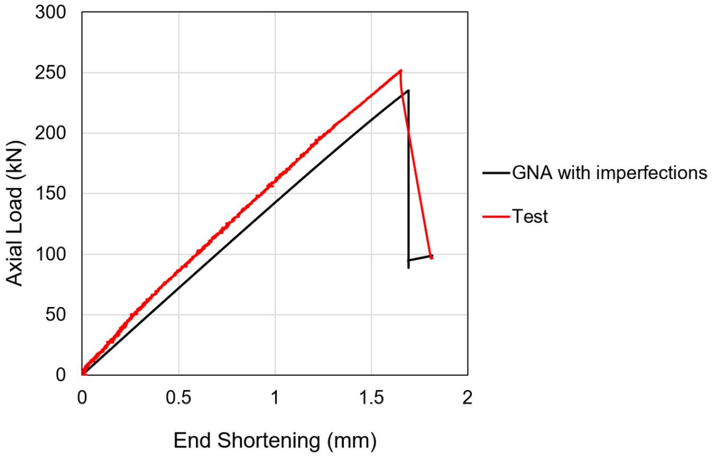

Figure 3.20: Finite element model with thickness-variation details.

The predicted radial displacements at incipient buckling are presented in Figure 3.21a. Multiple potential buckling-initiation sites can be observed as blue and black dimples just above the transition region with a minimum inward displacement of -0.42 mm. Another band of blue dimples is seen just below the transition in the cylindrical portion as well, but the minimum inward displacement in this region is only -0.08 mm. A third row of dimples, not as pronounced as the first two, is observed just above the tow-drop region. Ultimately, it was predicted that buckling would initiate with the dimple located at the 120-degree circumferential location in the cone just above the transition region. The outward radial displacement was predicted to be relatively uniform with the most-pronounced outward deformations shown in Figure 3.21a as the two red bands in the transition region. The maximum predicted outward radial displacement is 0.87 mm. Despite the presence of the radial imperfections, the radial displacements are relatively uniform at a given longitudinal location.

There are similarities between the predicted radial displacements, Figure 3.21a, and the observed radial displacements during test, Figure 3.21b. For example, the three sets of relatively inward radial displacements can be seen just above and below the transition region, and just above the tow drop. In addition, the region of the most outward deformation occurred in the transition region with a magnitude of 0.87 mm, the same as was predicted. On the other hand, the measured maximum inward displacement of -0.20 mm at incipient of buckling is approximately half of the predicted value of -0.42 mm. There were also similarities in the axial location of the radial-displacement patterns, but the dimples in the cylindrical region were more prominent than those in the conical region in the test data while the dimples were predicted to be more prominent in the conical region. The measured radial displacements in the cone seem skewed in the X-Y plane at a given axial location, while in the displacement predictions are uniform. This skew can be identified globally in Figure 3.21b by the presence of the shades of green and light blue in the conical region in the figure centered about 0 degrees, and the dark blue and purple colors in the conical region in the figure centered about 180 degrees. More specifically, just above the tow-drop region at the 0-degree circumferential location the measured radial displacement is 0.44 mm. The measured radial displacement at 180 degrees at the same axial location is 0.13 mm.

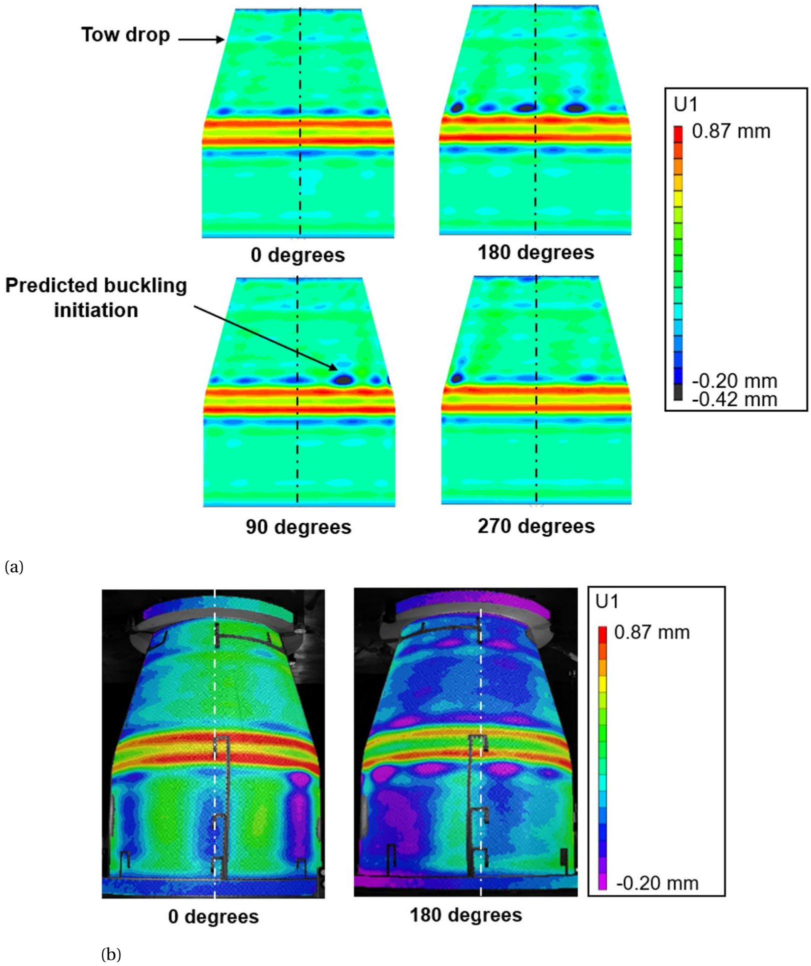

Figure 3.21: Radial displacement, U_1, at incipient buckling: a) FEM; b) test.

It is suspected that buckling initiated in the cylinder just outside the field of view of the 180-degree-centered high-speed DIC system, which encompasses the circumferential coordinates of approximately 125 degrees to 235 degrees. Figure 3.22 shows the radial displacements measured with the high-speed DIC system at the time of buckling initiation, 1.6 milliseconds (ms) and 3.2 ms into the buckling event, and in the final high-speed DIC frame at approximately 15 ms. In the first high-speed image (buckling initiation, Figure 3.22a), there is a purple inward dimple that forms on the edge of the field of view, circled, with an inward displacement of -2.11 mm. Between the initial image and 1.6 ms later, the dimple grows slightly and begins to propagate, Figure 3.22b. After 3.2 ms, the displacement at the buckling initiation location has grown much larger with an inward deformation approximately 6 times larger than it was at 1.6 ms, Figure 3.22c. Also, adjacent to the buckling initiation dimple, a pattern of four inward dimples has formed. Eventually, the four dimples coalesce into four circumferential axial waves around the entire cylindrical section of the specimen in the final post-buckling configuration as shown in Figure 3.22d. The inward deformation of the post-buckling configuration is -17.7 mm. The three dimples observed in the 180-degree high-speed camera view can also be viewed by 3CHELL in post-buckling as shown in Figure 3.23.

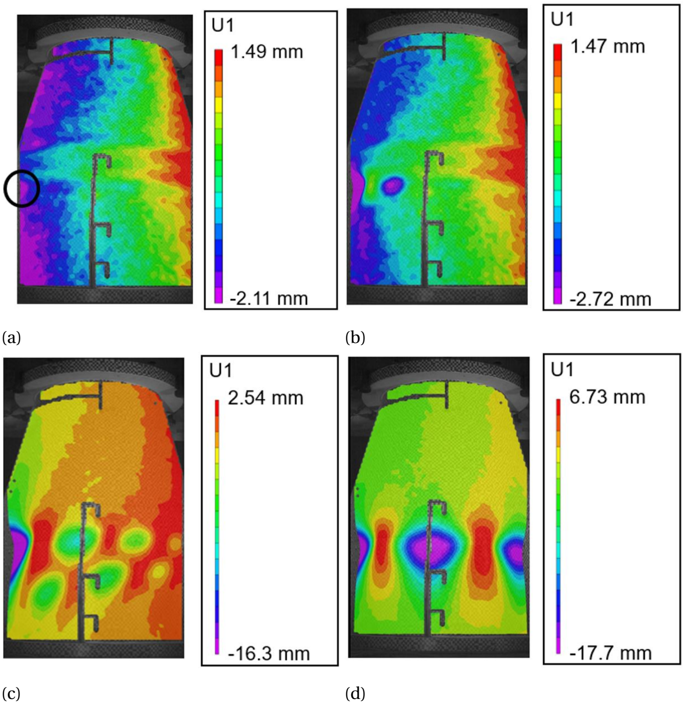

(a) (b)

(c) (d)

Figure 3.22: Buckling propagation from a) buckling initiation; b) 1.6 ms after initiation; c) 3.2 ms after initiation; and d) post-buckled configuration

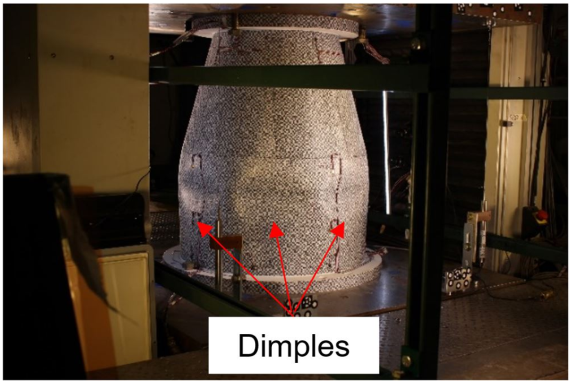

Figure 3.23: Postbuckling configuration of 3CHELL from the first test.

The high-speed images indicated that buckling initiated in the cylindrical portion of 3CHELL. However, buckling was predicted to initiate and propagate in the conical region, Figure 3.24. The post-buckling displacements from the FEM were taken from the point when the end-shortening in the analysis matched the measured test article end-shortening in a best attempt to quantitatively compare the data. Although the location of the predicted post-buckling deformation pattern is different than what was observed in test, the pattern and magnitude of the inward and outward radial deformations is similar. The minimum predicted inward deformation was -16.8 mm, approximately 1.0 mm less than what was measured. The maximum outward predicted deformation in the postbuckling configuration was 7.52 mm, less than 1.0 mm greater than what was measured.

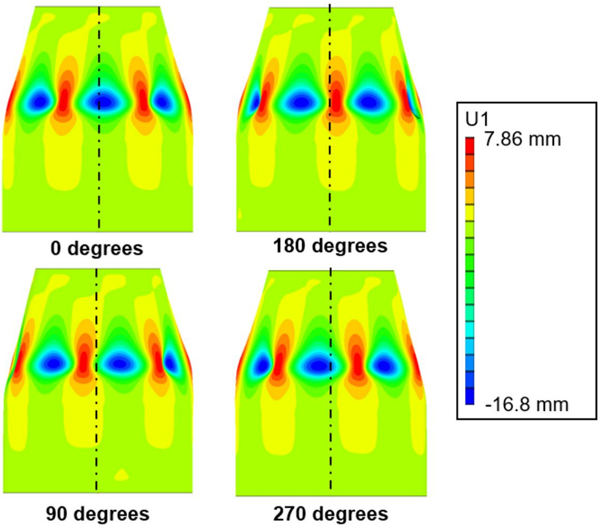

Figure 3.24: Postbuckling predicted by the FEM.

The differences between test and analysis in the postbuckling responses is due, in part, to the assumptions made when including the thickness variations. Buckling was predicted to occur in the conical region and buckling propagation would remain in the conical region because conical region in FEM was not as stiff as the conical region in 3CHELL. Also, the differences between the number of dimples present could also be related to the thickness variations between 3CHELL and what was assumed in the FEM. With regard to stiffness, the predicted curve in Figure 3.20, shows a total loss of stiffness after buckling initiation, which is different from what was indicated in the figure for the test. The jump in axial displacement after the buckling event is related to the stiffness of the load frame.

POSTTEST ANALYSIS

During testing, a small shearing motion in the load platen was identified using the real-time DIC displays. After the test, the relative movement between the top and bottom end rings was measured using the coordinate system with respect to the load frame and the orientation of 3CHELL shown in Figure 3.25. The measurements dX and dY are the changes in lateral displacement of the top load platen relative to the bottom load platen in, respectively, the X direction (toward 0 degrees) and Y direction (toward 90 degrees). The DIC-measured relative displacement between the top and bottom end rings in the X and Y directions are shown Figure 3.26. It can be observed from this figure, that the relative displacements between the top and bottom end rings at buckling were 0.16 mm in the X-direction and 0.31 mm in the Y-direction. This displacement results in a magnitude of 0.35 mm towards the 62-degree circumferential location. The total axial displacement of the test article at buckling was 1.65 mm, so the in-plane displacement was approximately 20% of the total axial shortening.

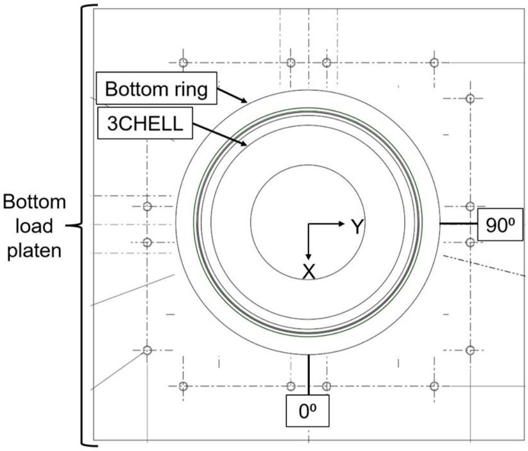

Figure 3.25: Top-down view of 3CHELL in load frame with coordinates for load platen movement.

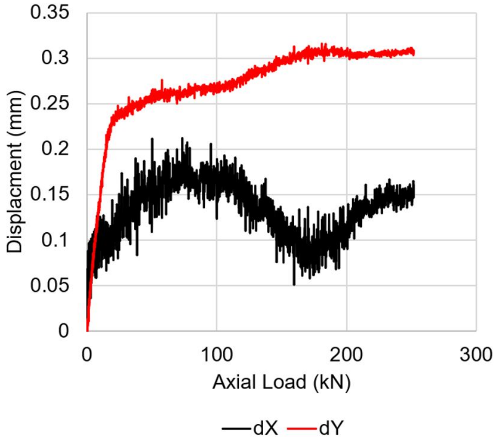

Figure 3.26: Measured load platen movement.

To represent the measured off-nominal shear displacement in the finite element analysis, an additional step was created in the analysis. The first step was used to simulate the relative shear displacements of 0.16 mm in the X-direction and 0.31 mm in the Y-direction at the initiation of buckling. The second step was used to simulate the application of the axial displacement at a rate of 0.076 mm/min, the same as used in the initial analysis.

The predicted buckling load with the shear displacement included was 231.4 kN, which is almost 2% lower than the initial FEM prediction and 8.8% lower than the experimental buckling load. In the load-displacement curves in Figure 3.27, it can be observed that the stiffnesses of the FEM with and without the shear displacement are indistinguishable, but that the predicted buckling load with the included shear displacement is slightly lower. While there was minimal change in the overall response, a skewed pattern in the predicted radial displacements at incipient buckling is observed in the conical region due to the shear displacement, as can be seen in Figure 3.28. The predicted outward radial displacements with the shear displacement included were to 1.0 mm, higher than without the shear displacement, but the maximum inward radial displacement remained unchanged. The inclusion of shear displacement did not significantly influence the results, despite the fact that the magnitude of the shear displacement was 20% of the total end shortening. It should be noted that the postbuckling equilibrium load with shear is 96.7 kN, almost the same as the model without shear and the test postbuckling equilibrium load.

The full-field strain distribution from DIC can be compared to the predicted strain from the outermost ply in the FEM with the shear displacement. The predicted and measured maximum principal strains are presented in Figure 3.29 and Figure 3.30, respectively. The patterns and strain magnitudes are quite similar for the views centered about 0 degrees (Figure 3.29a and Figure 3.30a) and 180 degrees (Figure 3.29b and Figure 3.30b). The maximum principal direction is primarily in the hoop direction. The areas with the highest maximum principal strain are in the transition region and coincide with the areas of maximum radial displacement. The highest predicted maximum principal strain at incipient buckling was 2785 $\mu\varepsilon$. This value is within 3% of the measured highest maximum principal strain of 2853 $\mu\varepsilon$.

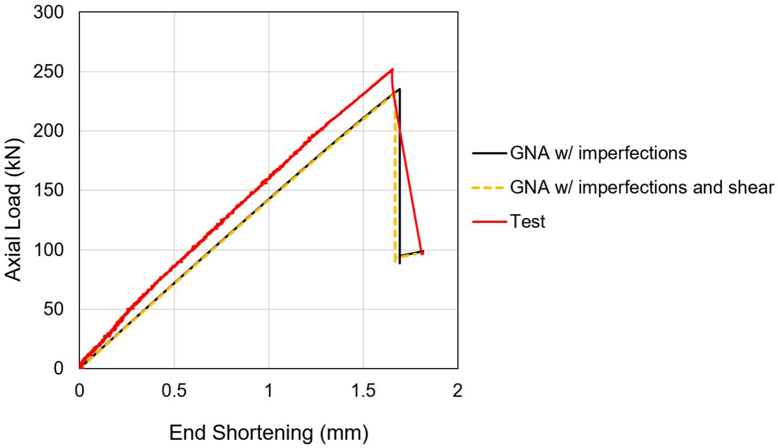

Figure 3.27: Compressive axial load versus end shortening curve from the GNA with shear and without shear, and test.

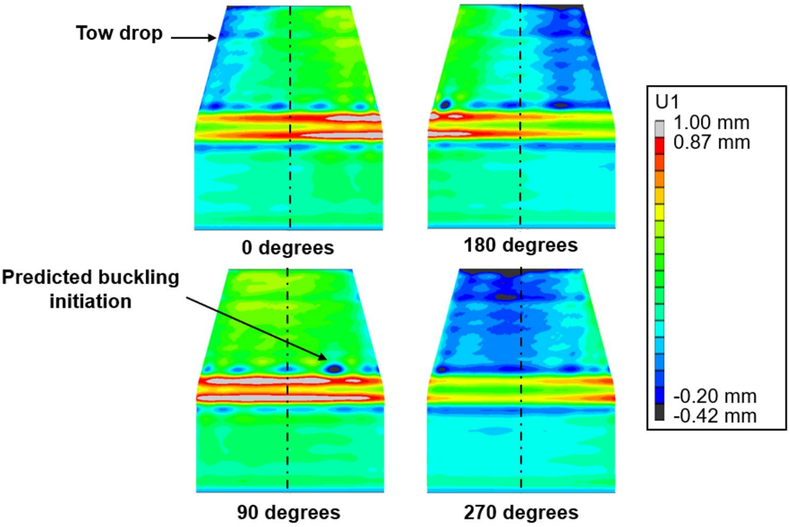

Figure 3.28: FEM with shear radial displacements at incipient buckling.

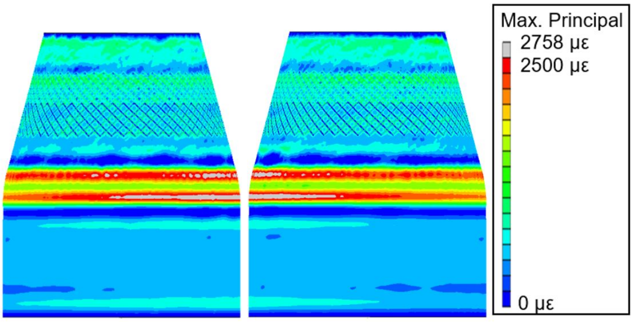

(a) (b)

Figure 3.29: Predicted maximum principal strain at incipient buckling: a) centered at 0 degrees; b) centered at 180 degrees.

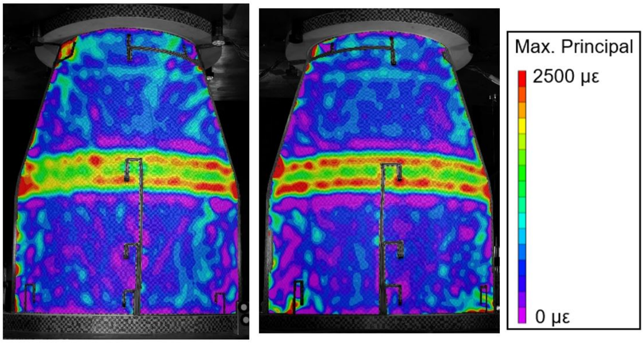

(a) (b)

Figure 3.30: Measured maximum principal strain at incipient buckling: a) centered at 0 degrees; b) centered at 180 degrees.

There are also elements of agreement when comparing the predicted and measured minimum principal strains as shown in Figures 3.31 and 3.32. The minimum principal direction coincides mainly with the axial direction. First, it is important to note the band of highly negative strains near the end of the conical region in the FEM. This predicted negative strain is due to the way in which the radial imperfections were incorporated into the model. The structured light scanning data near this region is noisy, which can lead to abrupt radial changes in the mesh. The lowest predicted minimum principal strain recorded in this region is -7131 $\mu\varepsilon$. If this end region is discounted, then the lowest minimum principal strain is -4222 $\mu\varepsilon$, which occurs just above the transition region at the base of the cone in Figure 3.31b. This spot corresponds to the inward dimple in Figure 3.28 for the view centered about 180 degrees. The lowest minimum principal strain measured at incipient buckling was -3971 $\mu\varepsilon$, which approximately occurs in the same circumferential region as was predicted, but just below the transition in the cylinder. As with the maximum principal strain plots, the ply overlaps are observed in the predicted data, but not in the DIC data.

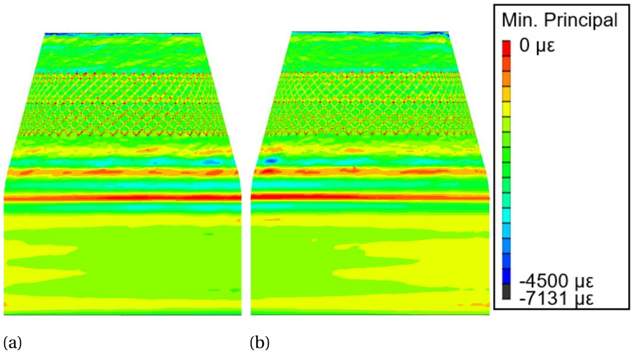

Figure 3.31: Predicted minimum principal strain incipient of buckling:
a) centered at 0 degrees; b) centered at 180 degrees.

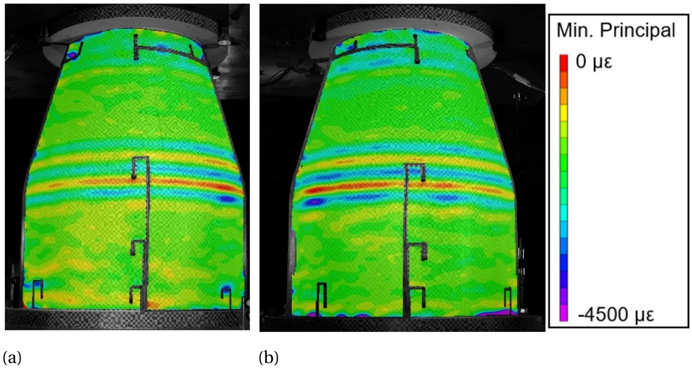

Figure 3.32: Measured minimum principal strain at incipient buckling:
a) centered at 0 degrees; b) centered at 180 degree.

The predicted (FEM) and measured (Test) cylindrical-end axial membrane strains, shown in Figure 3.33, and bending strains, shown in Figure 3.34, were plotted for the corresponding axial loads to investigate the previously mentioned experimental slope change observed in the load versus displacement plot (see Figures 3.20 and 3.27). A change in slope in the load-strain curve can also be observed in the cylinder-end axial membrane strain at the 0-degree circumferential location, black solid line (Figure 3.33a). Also, a change in slope can be seen in the 45-degree circumferential location at approximately 25 kN, where the slope is increasing until just under 50 kN, at which point the slope decreases slightly (Figure 3.33b). In the bending-strain data at the cylindrical end, there is no calculated bending strain until just below 50 kN for the 0-degree and 45-degree circumferential degree locations (Figure 3.33a and 3.33b). Therefore, the change in slope around 50 kN may be related to the bending strain.

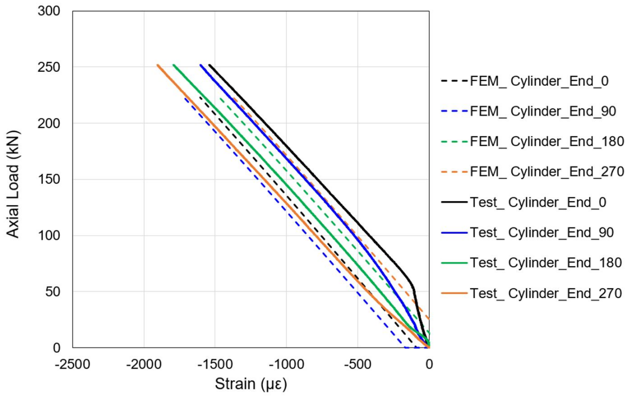

(a)

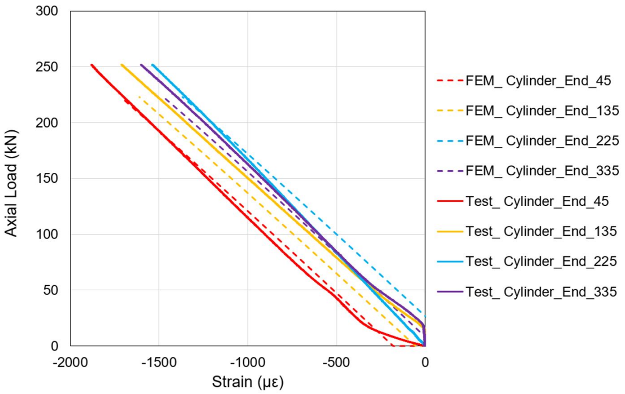

(b)

Figure 3.33: Cylinder-end axial membrane strains: a) 0-, 90-, 180-, and 270-degree locations; b) 45-, 135-, 225-, and 335-degree locations.

To better understand why the cylinder-end bending strain at 0 degrees remains near zero until a load of approximately 50 kN, DIC was used to compare the change in axial displacement before and after 50 kN. Shown in Figure 3.35 is the change in axial displacement, dZ, between a) 10 kN and 20 kN, b) 20kN and 40 kN, c) 40 kN and 50 kN, and d) 50 kN and 70 kN for the DIC cameras centered about 0 degrees. Shown in Figure 3.36 is the change in axial displacement at the same load levels, but for the DIC cameras centered about 180 degrees.

The change in axial displacement pattern between 10 kN and 20 kN was dominated by the shear displacement imparted by the load frame, and not due to the axial load, Figure 3.35a and Figure 3.36a. As the load increased, the top of the test article exhibited a more-uniform loading pattern as shown by the horizontal purple band with similar magnitudes in Figure 3.35b and Figure 3.36b. At the bottom of the test article at 0 degrees, there is more axial displacement than at the edges of the frame (towards 335 and 45

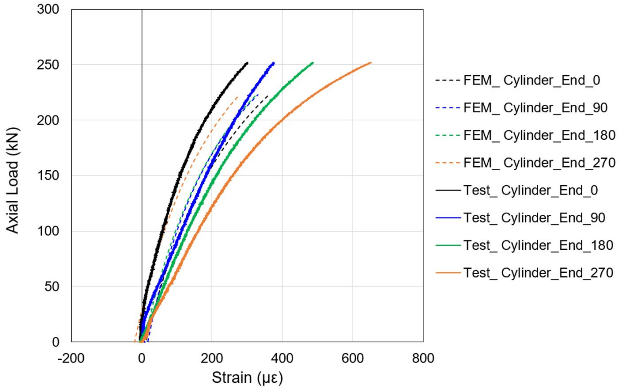

(a)

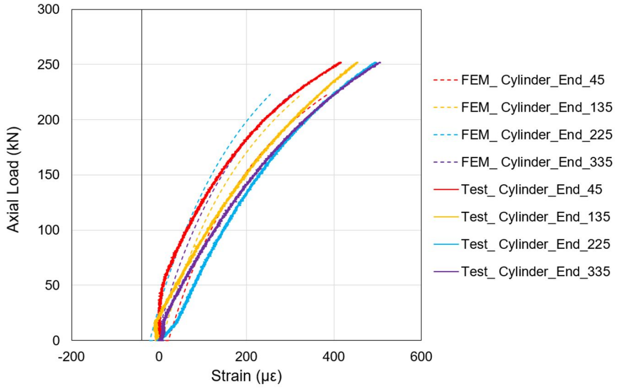

(b)

Figure 3.34: Cylinder-end bending strains: a) 0-, 90-, 180-, and 270-degree locations; b) 45-, 135-, 225-, and 335-degree locations.

degrees) in Figure 3.35b. This variation in the bottom axial displacement is observed by the warmer colors near the edge of the frame that correspond to a smaller change in axial displacement compared to the cooler colors that represent a larger change in axial displacement near the center of the frame, Figure 3.35b. A more uniform distribution is observed in the bottom of Figure 3.35b, where the relatively horizontal bands extend from the top to the bottom. This same trend of more bottom displacement-variation near the 0-degree position than the 180-degree position is seen in Figure 3.35c and Figure 3.36c, which show the change in axial displacement between 40 kN and 50 kN. This trend indicates a potential gap between the ring and the end of the test article near 0 degrees, which would allow the test article to displace more in this region than at 335 and 45 degrees, where the end of 3CHELL could be in contact with the end ring. The behavior was more uniform in the DIC system centered around the 180-degree circumferential location at the same load level, as indicated by the horizontal contour bands, signifying a more uniform axial displacement. Instead, the more uniform horizontal bands indicate more uniform axial displacement.

Between 40 kN and 50 kN, the bottom edge of 3CHELL separated from the end ring by 0.01 mm, as shown by the green-yellow coloration at the bottom end ring-test article interface in Figure 3.35c. After the change in slope, the change in axial displacement between 50 and 70 kN becomes more uniform for the region centered about 0 degrees. The horizontal bands in Figures 3.35d and 3.36d are relatively uniform, which may signify that a gap has closed, and the test article is in complete contact with the ring. The change in axial displacement between 50 and 70 kN at 180 degrees remained uniform. The fact that the measured responses are more uniform in Figure 3.36 than in Figure 3.35 correlates well with the strain data because the slope change anomaly was most apparent in the cylinder gages at 0 degrees.

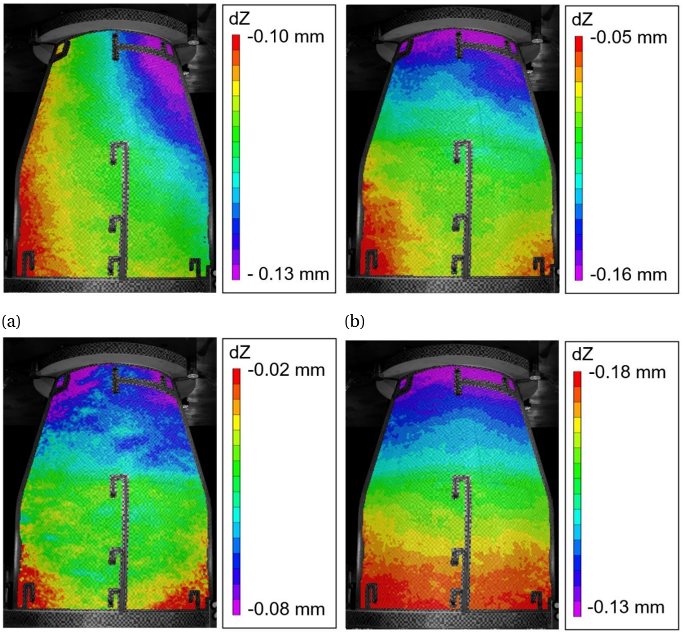

(a) (b)

(c) (d)

Figure 3.35: Change in axial displacement at 0-degrees between load intervals: a) 10 kN-20 kN; b) 20 kN-40 kN; c) 40 kN-50 kN; d) 50 kN-70 kN

The maximum and minimum principal strains in the postbuckling pattern also have elements of agreement when comparing the test results to the FEM as shown in Figures 3.37 – 3.38 despite the fact that the experimental buckling occurred in the cylindrical region rather than the conical region as predicted. The postbuckling strains from the FEM were taken from the point when the end-shortening in the analysis matched the measured test article end-shortening in order to quantitatively compare the data. The maximum and minimum principal strain values predicted are quite similar to the measured values. The highest maximum principal strain predicted was 9020 $\mu\epsilon$ and the strain measured

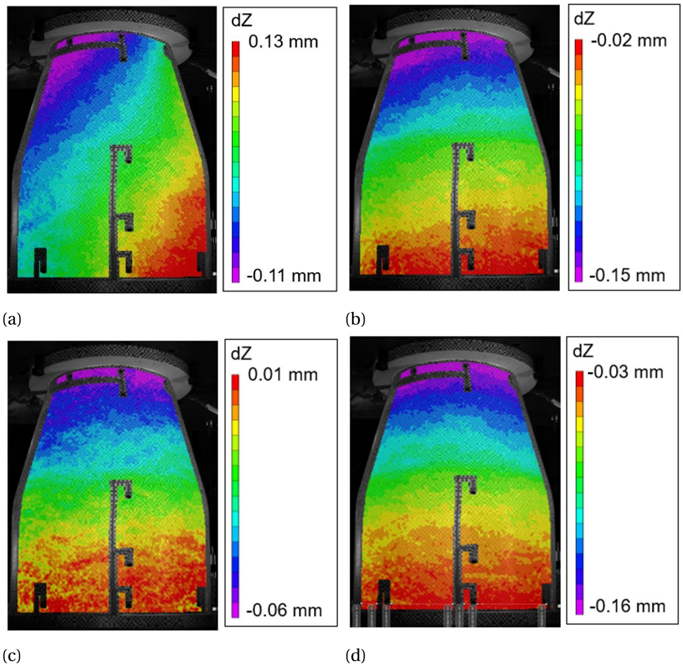

(a) (b) (c) (d)

Figure 3.36: Change in axial displacement at 180-degrees between load intervals: a) 10 kN-20 kN; b) 20 kN-40 kN; c) 40 kN-50 kN; d) 50 kN-70 kN.

was 9055 $\mu\varepsilon$. This is only a 35 $\mu\varepsilon$ difference, which is within the error limits of the DIC capability. The region of maximum principal strain occurred between the dimples in the postbuckling configuration shown in Figure 3.37 and Figure 3.38. The most negative minimum principal strain predicted was -9396 $\mu\varepsilon$, while the most negative minimum principal strain measured was -9613 $\mu\varepsilon$, less than 3% different from what was predicted, which occurs at the edges of the dimples in the postbuckling configuration (see Figure 3.39 and Figure 3.40). The magnitudes of the strains are similar, even though postbuckling behavior was contained in the cylindrical region instead of the conical region as predicted. The difference in the postbuckling location is most likely due to the assumptions made when incorporating the thickness variations in FEM. A cone that is stiffer, in this case more ply overlaps, would buckle at a higher load than the cylindrical region that does not have ply overlaps. This will be interrogated in detail in Chapter 4.

It should be noted that the highest measured maximum principal strain of 9055 $\mu\varepsilon$ is less than the threshold used in design as reported in Table 3.4 of (10,956 $\mu\varepsilon$). However, the lowest measured minimum principal strain value of -9613 $\mu\varepsilon$ is greater than the design value of -9065 $\mu\varepsilon$. The calculated failure strains are conservative since they were calculated assuming linear elastic properties. After loading, the test article returned to its original shape, and no material failure was apparent upon visual inspection. Based on these observations, it was concluded that the test article was likely undamaged.

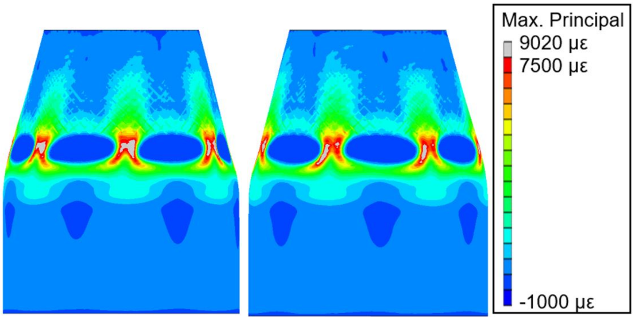

(a) (b)

Figure 3.37: Predicted maximum principal strain at postbuckling:
a) centered at 0 degrees; b) centered at 180 degrees.

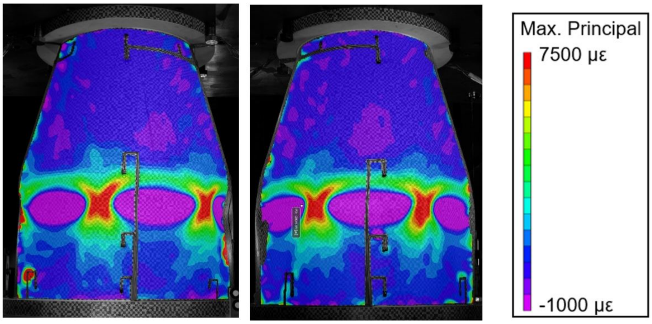

(a) (b)

Figure 3.38: Measured maximum principal strain at postbuckling:
a) centered at 0 degrees; b) centered at 180 degrees.

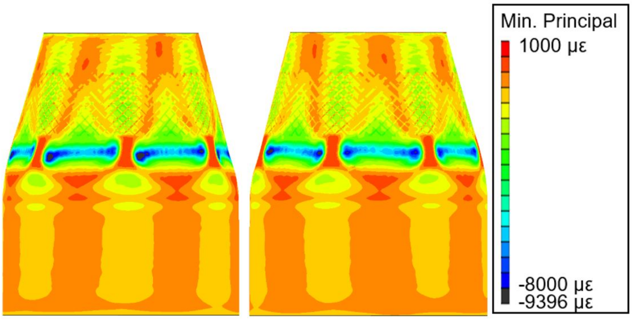

(a) (b)

Figure 3.39: Predicted minimum principal strain at postbuckling:
a) centered at 0 degrees; b) centered at 180 degrees.

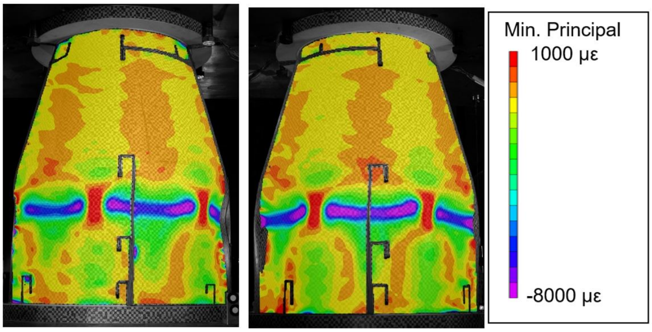

(a) (b)

Figure 3.40: Measured minimum principal strain at postbuckling:
a) centered at 0 degrees; b) centered at 180 degrees.

Overall, there was good correlation between the FEM and the experimental results, which is valuable since there is limited experimental data on the buckling of composite conical-cylindrical shells. The differences between test and analysis may not necessarily be related to the modeling methodology (eg.completing a nonlinear analysis and accounting for measured geometric imperfections), but rather external factors that were not quantified such as the test setup and model resolution related to the tow overlaps. For example, the shear from the load platen affected the radial displacements. Also, the apparent gap in the end ring seemed to influence the test article's initial stiffness. Another possible source of variance was related to the manufacturing process, specifically the overlaps. It is thought that the influence of the the tow overlaps was larger in 3CHELL than it would be in a larger launch-vehicle structure because the influence of each tow overlap is related to the shell thickness, which would be larger for most flight structures. In general, the model was able to predict the global behavior with good accuracy. This would suggest the modeling approach present is appropriate for predicting the buckling response of a conical-cylindrical shell, and could potentially be used in finite element analyses to develop buckling design guidance.

Some of the differences between test and analysis may also be attributable to the assumptions made when incorporating the thickness variations into the FEM. The calculated specimen weight in the FEM was 3.31 kg and the measured weight of 3CHELL was 3.40 kg. The larger mass in the physical test article indicates that there was additional material not accounted for in the FEM. It is presumed that this additional material was related to the tow overlaps that form the grid-like pattern seen in the thickness variations in Figure 3.13, and may be the reason for the measured stiffness being higher than predicted, and subsequently the overall buckling load as well. In addition, if the cone was stiffer than what was modeled and the cone was stiffer than the cylindrical region then this would explain the discrepancy in buckling location between the test and FEM. The differences between the test and analysis highlights the amount of detail that may be required to accurately capture the buckling behavior of a conical-cylindrical shell. The buckling behavior of conical-cylindrical shells may be sensitive to stiffness variations (e.g., tow overlaps), intentional or otherwise.

In the future, importing the thickness data from the structured light scan data into the FEM could help improve the results, as might a smaller mesh size. An attempt was made to include the structured light scanning data into the finite element model using the continuum shell reduced integration elements (SC8R) and a smaller mesh edge side of 2.54 mm. The OML and IML nodes could be manipulated based on the structured light scanning data from the OML and IML surfaces and could account for the radial imperfections and thickness variations. Afterwards, the section properties for elements with an increase thickness corresponding to an additional ply would need to be modified. Unfortunately, this approach made the model computationally cumbersome. This approach was not implemented due to constraints on the computational resources. A similar approach of modifying the SC8R nodes to account for thickness and radial imperfections to predict the buckling of a composite cylinder is presented in reference [36] with good results.

SECOND BUCKLING TEST

Since the first test was successful and the test article appeared to have buckled elastically, it was decided to repeat the final buckling load sequence. The test article response was very similar to that of the first buckling test and the test article buckled within 1% of the first buckling test, Figure 3.41. The measured buckling load from the first test was 251.8 kN with a measured end shortening of 1.65 mm, and during the second test 3CHELL buckled at 250.99 kN with a measured end shortening of 1.63 mm. As seen in Figure 3.41, the stiffnesses were essentially the same; the blue line, representing the load versus displacement curve from the second test, seems to trace over the load versus displacement curve (red line) from the first test. The postbuckling equilibrium load for the second test was 96.6 kN, as compared to 96.7 kN for the first test.

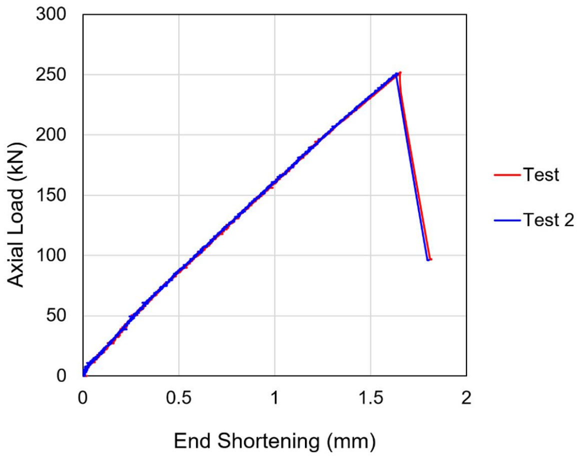

Figure 3.41: Axial load versus end shortening curve for both buckling load sequences.

The buckling propagation sequences from the first test, Figure 3.22, and the second test, Figure 3.42, were essentially the same. Buckling initiated in approximately the same region just outside the field of view of the high-speed camera, circled in Figure 3.22a and

Figure 3.42a. A second dimple formed adjacent to the buckling initiation dimple 1.6 ms after buckling initiation, Figure 3.22b and Figure 3.42b. In addition, two rows of dimples are present next to the buckling initiation after 3.2 ms after buckling initiation, Figure 3.22c and Figure 3.42c. Finally, the postbuckling configuration of six circumferential waves is present in both the first and second test, Figure 3.22d and Figure 3.42d. The outward and inward radial displacements for both postbuckling configurations are similar, where during the first test the maximum outward deformation was 6.73 mm and 7.24 mm during the second test. The maximum inward deformation was -17.7 mm and -17.8 mm after the first and second test, respectively. Similarly, three distinct dimples can be seen in the postbuckling configuration from the second test, Figure 3.43, as was observed in the first, Figure 3.23.

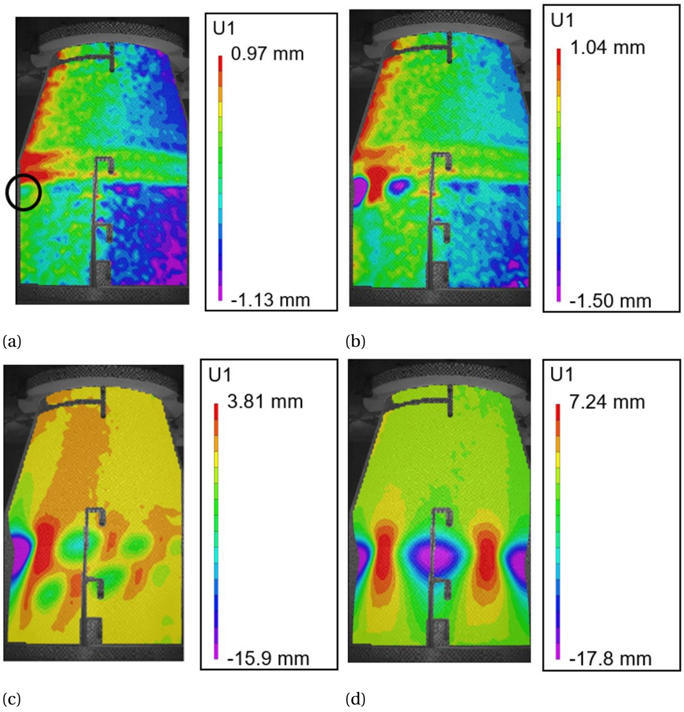

Figure 3.42: Buckling propagation from a) buckling initiation; b) 1.6 ms after initiation: c) 3.2 ms after initiation;and d) Post-buckled configuration.

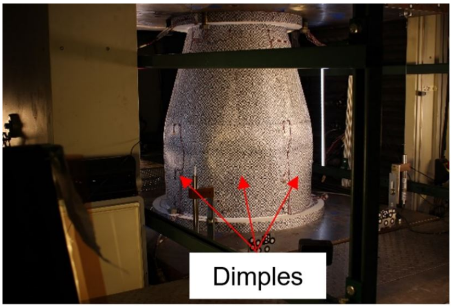

Figure 3.43: Postbuckling configuration of 3CHELL from the second test.

The maximum and minimum principal strain distributions at incipient buckling for the second buckling test are shown in Figures 3.44 and 3.45, respectively, and are similar to that of the first buckling load sequence (Figures 3.30 and 3.32). The contour plots for the measured maximum and minimum principal strains at incipient buckling from the second test are analogous to the first test. The areas of the most positive and most negative strain values occur in the transition region. The highest value for the maximum principal strain at incipient buckling for the second test was 2924 $\mu\varepsilon$, which is within 100 $\mu\varepsilon$ of the first test, and the error limits of the DIC capability. The lowest value for the minimum principal strain incipient of buckling for the second test was -3546 $\mu\varepsilon$, which is approximately 10% lower than the first test (4222 $\mu\varepsilon$).

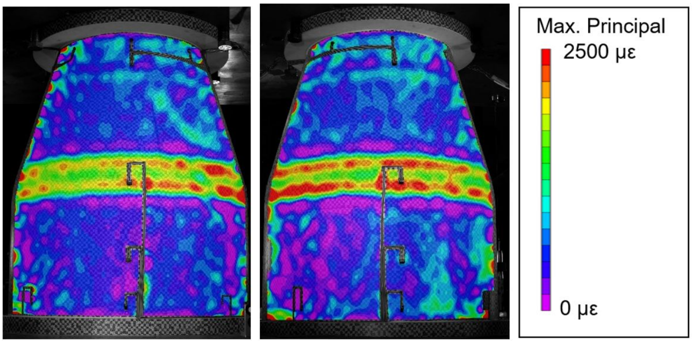

(a) (b)

Figure 3.44: Measured maximum principal strain at incipient buckling:
a) centered at 0 degrees; b) centered at 180 degrees.

The maximum and minimum principal strains for the postbuckling configuration are very similar between the first, Figures 3.38 and 3.40, and second tests, Figures 3.46 and 3.47. The measured maximum principal strain from the second test is 9064 $\mu\varepsilon$, which is only 10 $\mu\varepsilon$ different from the measured maximum principal strain from the first test (9055 $\mu\varepsilon$). The measured minimum principal strain from the second test is -9032 $\mu\varepsilon$ and is approximately 600 $\mu\varepsilon$ less than what was measured in the first test (-9613 $\mu\varepsilon$).

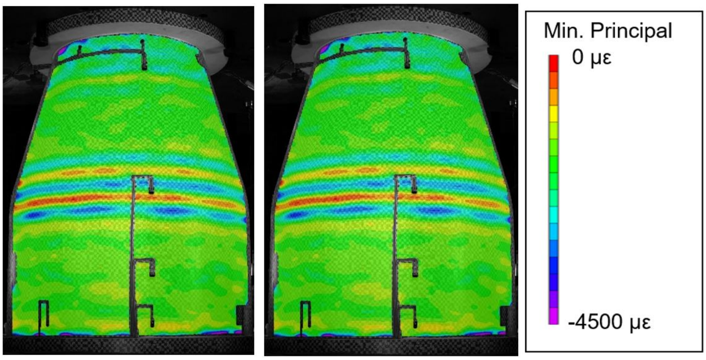

(a) (b)

Figure 3.45: Measured minimum principal strain at incipient buckling: a) centered at 0 degrees; b) centered at 180 degrees.

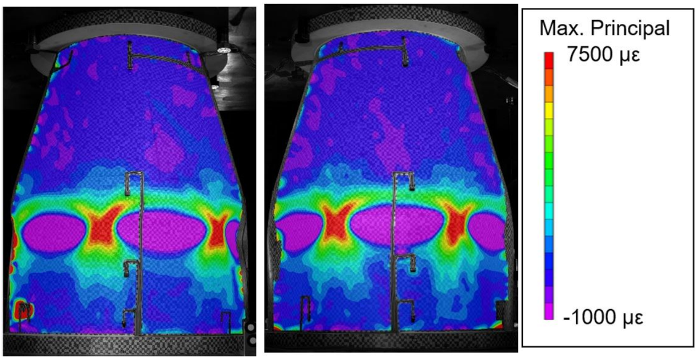

(a) (b)

Figure 3.46: Measured maximum principal strain at incipient buckling: a) centered at 0 degrees; b) centered at 180 degrees.

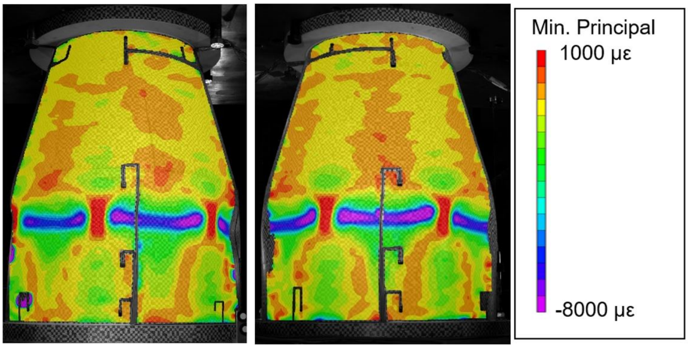

(a) (b)

Figure 3.47: Measured minimum principal strain at incipient buckling: a) centered at 0 degrees; b) centered at 180 degrees.

3.4. CONCLUSION

Utilizing a single-piece composite conical-cylindrical shell with a toroidal transition for aerospace applications has the potential to reduce structural mass and expand the design space for launch vehicles and payload adapters. This geometry combines cylindrical and conical shells common in launch-vehicle architecture, thereby eliminating the need for the heavy, stiff interface ring that often separates two independent shell structures. However, such conical-cylindrical shells can be susceptible to stability failures. A composite conical-cylindrical shell with a toroidal transition, 3CHELL, was fabricated, and tested. The specimen was designed to fail in buckling in an effort develop a better understanding of the buckling response of this type of shell structure. The numerical and experimental data presented provides insight into the ability to predict the buckling response of a composite-conical cylindrical shell using nonlinear FEM to aid in future design guidelines and recommendations for structures of this geometry.

The purpose of the presented work is to demonstrate the ability to predict the buckling behavior of this special shape in order to influence the future designs of launch vehicles and payload adapters. A FEM that included radial imperfections and thickness variations was developed, and GNA analyses were conducted to predict the structural response. The test article buckled at 251.8 kN, and the predicted buckling load from an analysis that included measured off-nominal shear movement of the load platens was 231.4 kN, an 8.8% difference. The lateral displacement was 20% of the total axial end shortening at buckling but simulation of this lateral movement did not significantly influence the results. The predicted and measured buckling responses had several similarities when radial displacements and patterns at incipient buckling and postbuckling were compared. The measured and predicted buckling-initiation location were different, but similar patterns in the radial deformations and magnitudes could be identified. In addition, the buckling test was repeated since 3CHELL buckled without perceptible damage, and in the second test 3CHELL buckled within 1% of the first buckling test.

Some of the discrepancies, such as buckling load, buckling location, and test-article stiffness, between test and analysis may be attributable to the size of the test article and its design. For example, one possible explanation for the differences in stiffness, buckling load, and buckling location is the assumptions made when incorporating thickness variations due to ply overlaps in the conical region. The overlaps were a manufacturing limitation of the AFP robot to maintain a constant fiber angle along the length of the cone, while eliminating gaps. For a larger structure, these manufacturing limitations observed in 3CHELL may not be an issue, but sources of stiffness variation should be included in the FEM since the buckling behavior of conical-cylindrical has been demonstrated to be sensitive to stiffness variations. The sensitivities to thickness variations are investigated in Chapter 4.

4

ANALYSIS AND TESTING OF A LAUNCH-VEHICLE-LIKE COMPOSITE CONICAL-CYLINDRICAL SHELL WITH REINFORCEMENT

CONICAL-CYLINDRICAL shells are common geometries in launch-vehicle structures as stage adapters and payload adapters, and they are susceptible to buckling due to their large radius-to-thickness ratios. Buckling design guidance is available, but it is limited for conical and cylindrical shells. There is no available buckling design guidance for conical-cylindrical shells. This paper presents the validation of two finite element models used to successfully predict the buckling behavior of a conical-cylindrical composite shell with and without reinforcement tested in two separate campaigns. The laminate design for the first test campaign consisted of a quasi-isotropic layup. For the second test campaign, additional composite plies were applied to reinforce the transition region of the original laminate. The work presented demonstrates the ability to predict the buckling behavior of a composite conical-cylindrical shells with two different designs, which may aid in creating buckling design guidance for conical-cylindrical shells. Additionally, in this chapter, it is shown that there is no appreciable benefit of adding reinforcement to the transition region if the intent is to increase the buckling load, due to the fact that the reinforcement brings increased buckling imperfection sensitivity to the shell.

This chapter has been adapted from Rudd MT., Schultz MR., Bisagni C., "Buckling behavior of Conical-Cylindrical Shells and Design Considerations for Launch-Vehicle Structures", AIAA Scitech Forum 2024, AIAA Paper 2024-0034 and Rudd MT., Schultz MR., Gardner NW., Kosztowny CJR., Bisagni C., "Experimental validation of the buckling behavior of unreinforced and reinforced composite conical-cylindrical shells for launch-vehicles", Composite Structures, Volumes 349–350, 2024

4.1. INTRODUCTION

Empirically-based KDFs are used to account for differences between test and analysis, which are largely attributable to radial imperfections and can be specific to the structural design. The buckling capability of a shell is related of the imperfection sensitivity, meaning the greater the imperfection sensitivity, the lower the buckling design load. Researchers have investigated how to design imperfection insensitive shell structures with the goal of increasing the design buckling load. One way to design imperfection-insensitive shell structures was by stabilizing the postbuckling response to prevent a large loss in load after an initial buckling event. Bisagni and Cordisco [70] manufactured and tested stiffened composite cylinders to assess the performance in the postbuckling range. Ning and Pellegrino [71, 72] took a nontraditional approach by investigating cylinders with wavy cross sections to demonstrate imperfection insensitive designs. Lincoln, et al. [73] took an alternative approach by designing imperfection-insensitive composite cylinders with variable tow angles. Using variable tow angles breaks up the symmetry in the prebuckling strain field, which may reduce the cylinder's sensitivity to imperfections. Wagner, et al. [74] used machine learning to optimize buckling load and imperfection insensitivity. Additionally, it was demonstrated in Chapter 3 and [75] that conical-cylindrical shells can be designed to be insensitive to radial imperfections, which may save mass.

In addition to radial imperfections, tow overlaps and gaps due to the automated fiber placement (AFP) manufacturing constraints have been demonstrated to affect the buckling behavior of small-scale composite test articles. Tow overlaps and gaps were carefully considered in the modeling of NDL-1 in Chapter 2, for this reason. Additionally, Chapter 3 determined that the probable reason for the discrepancy between the test data and numerical predictions of the buckling of a composite conical-cylindrical shell was due to assumptions made when incorporating the unavoidable tow overlaps into the finite element model. The concept of design for manufacturing can be used to account for potential tow gaps, overlaps, and other manufacturing constraints during the AFP process. To account for these new manufacturing-based details in the design, the build of the part can be simulated, and the overlaps and gaps can be estimated. Then a process to modify the design to minimize the gaps and overlaps can be completed [76, 77].

Specifically regarding the buckling behavior of composite conical-cylindrical shells, the minimal research publicly available to this shape is primarily specific to the piping and civil industry [48, 49]. With regard to aerospace applications, Chronopoulos, et al. [54] focused on the dynamic response of a composite conical-cylindrical-conical shell in which the geometry was based on the Sylda. Chapter 3 and [75] also investigated the buckling of composite conical-cylindrical shells and showed that the currently used empirically-based KDF approach may not be appropriate for conical-cylindrical shells. Additionally, the ability to predict the buckling behavior of a conical-cylindrical shell was shown in Chapter 3 and [78] by providing test and analysis correlation data which can be used towards the development of buckling design guidelines.

In order to develop buckling design guidance, it is recommended to have at least more than one test of a conical-cylindrical shell to validate the buckling response predictions of an associated finite element model (FEM). Correspondingly, the test and analysis results of a second buckling test of a composite conical-cylindrical shell was completed. The first buckling test article, 3CHELL, buckled elastically after the first test campaign. The test article was undamaged, and additional composite reinforcement was added to the transition region. The modified test article with reinforcement will be referred to herein as Re3CHELL.

The use of FEM to predict the buckling behavior of a composite conical-cylindrical shell without and with reinforcement, 3CHELL and Re3CHELL, respectively, will be demonstrated in Section 4.2. The design and manufacturing details of 3CHELL and Re3CHELL are discussed in Section 4.3.1. Next, the finite element model of 3CHELL and Re3CHELL is discussed in Section 4.3.2. This includes information pertaining to an updated 3CHELL FEM based on manufacturing data, and how the manufacturing data influenced the FEM of Re3CHELL. The experimental setup for Re3CHELL is included in Section 4.3.3. The updated 3CHELL FEM is compared to the 3CHELL experimental data in Section 4.3.4, and the Re3CHELL FEM is compared to the Re3CHELL experimental data also in Section 4.3.4. The effect of adding reinforcement to a composite conical-cylindrical shell by comparing the buckling response of 3CHELL and Re3CHELL is discussed in Section 4.3.5. Concluding remarks are presented in Section 4.4.

4.2. NUMERICAL STUDY ON THE EFFECTS REINFORCEMENT HAS ON THE BUCKLING BEHAVIOR OF A CONICAL-CYLINDRICAL SHELL

With composite material systems, it is possible to reinforce localized areas of a structure with additional plies. For example, it may be advantageous to increase the stiffness of the transition region, and this could affect the buckling behavior and imperfection sensitivity of the composite conical-cylindrical shell. To investigate the influence of localized reinforcement of the transition region further, four reinforcement cases were considered, ranging in relative stiffness of less stiff to more stiff, as shown in Table 4.1. The area where reinforcement was applied is highlighted in red in Figure 4.1. The reinforcement material is the same as the original layup, [32] The baseline configuration has a radius of curvature equal to 400 mm and no additional plies. The increase in mass from the baseline composite-conical cylindrical shell due to the additional plies is also shown.

Table 4.1: Transition reinforcement layups and associated percent increase in mass.

Reinforcement	Layup	% Increase in mass
Baseline	$[45/\text{-}45/90/0]_S$	-
Reinforcement 1	[**90**/45/-45/90/0/0/90/-45/45]	1.1%
Reinforcement 2	$[\mathbf{90}/45/\text{-}45/90/0]_S$	2.2%
Reinforcement 3	$[\mathbf{90}/\mathbf{0}/45/\text{-}45/90/0]_S$	4.7%
Reinforcement 4	$[\mathbf{90}/\mathbf{0}/\mathbf{90}/\mathbf{0}/\text{-}45/90/0]_S$	9.4%

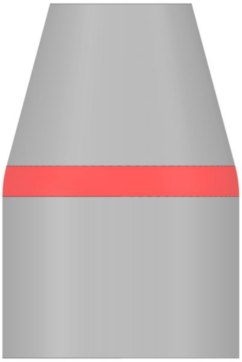

Figure 4.1: Region where reinforcement was applied highlighted in red.

The results from the eigenvalue buckling analyses and quasi-static nonlinear buckling analyses for the composite conical cylindrical shells with and without reinforcement are presented in Table 4.2 and Figure 4.2. The eigenvalue buckling loads for all levels of reinforcement were the same, similar to what was observed when the radius of curvature was increased (Table 3.1). The nonlinear buckling load, on the other hand, increases as additional plies are added, but only up to the eigenvalue buckling load. In this case, after Reinforcement 3, the nonlinear buckling load seems to converge to the eigenvalue buckling load as seen in Figure 4.2. The overall shell stiffness was increased with Reinforcement 4, but the buckling load was not significantly increased. Therefore, there seems to be a point of diminishing returns when comparing the mass of the additional reinforcement to the increase in buckling load as predicted by the quasi-static nonlinear analysis.

Table 4.2: Buckling loads predicted as an eigenvalue of the buckling equation and as the peak load of a quasi-static nonlinear buckling analysis for composite conical-cylindrical shell with different transition-region reinforcement layups.

Reinforcement case	Eigenvalue buckling load (kN)	Nonlinear quasi-static buckling load (kN)
Baseline	331.0	271.7
Reinforcement 1	331.0	296.9
Reinforcement 2	331.0	319.8
Reinforcement 3	331.0	331.9
Reinforcement 4	331.0	332.2

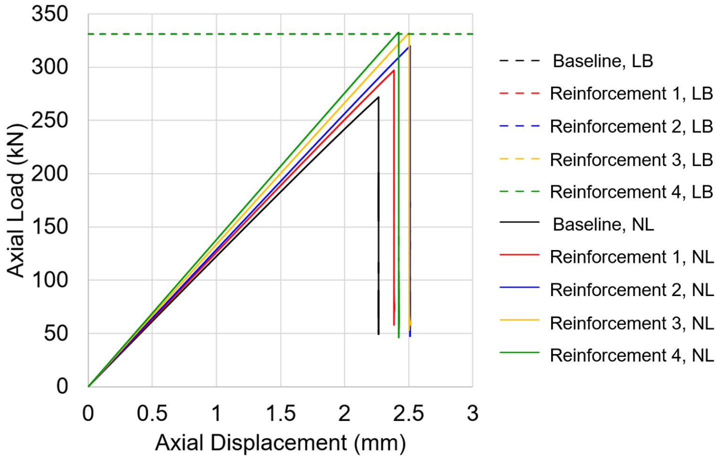

Figure 4.2: Eigenvalue buckling load (LB) and nonlinear response (NL) for the composite conical-cylindrical shell with different transition-region reinforcement layups. The eigenvalue buckling load is extended as a dashed line over the horizontal axis for comparison purposes with the peak load of the non-linear response.

The buckling load from the nonlinear analysis of the shell with Reinforcement 3 was 331.9 kN, which is essentially equal to the eigenvalue buckling load. The buckling load of the shell with Reinforcement 3 and a radial imperfection amplitude equal to 10% of the wall thickness was 214.0 kN (Figure 4.3). It should be noted that in Figure 4.3 the dashed line representing the linear buckling load for the Baseline design is on top of the dashed line showing the Reinforcement 3 linear buckling load. This results in a normalized buckling load of 0.65, and the reduction in load is solely due to the presence of imperfections. This result is opposite from what was observed for the radius of curvature of 0 mm, which also had a normalized buckling load of 0.65, but where the reduction in load was due to the influence of nonlinear effects (Figure 4.3). It should be noted that, while the buckling load of the perfect shell may increase by reinforcing the transition region, the reinforced conical-cylindrical shell may be more imperfection sensitive. Therefore, the inclusion of additional plies in the transition did not improve the buckling behavior of the imperfect composite-conical cylindrical shell because it was more sensitive to imperfections, which negated the benefits of adding the reinforcement.

In the end, a KDF is required to account for the difference between the tested buckling load and the buckling load from an eigenvalue analysis of the geometry without imperfections. For a conical and cylindrical shell, a significant percentage of the difference between test and analysis is attributable to imperfections, which are generally unknown during the design phase. For conical-cylindrical shells it is possible to design the structure so that buckling design load is less sensitive to imperfections, and more sensitive to large displacements and rotations. The large rotations and displacements can be accounted for in the design phase with a geometrically nonlinear analysis. Therefore, it may be possible to use a KDF closer to unity if the buckling load of the shell is more susceptible to the effects of nonlinear geometry, which may result in a more mass efficient design. A second test campaign was completed in order to validate the numerical observations.

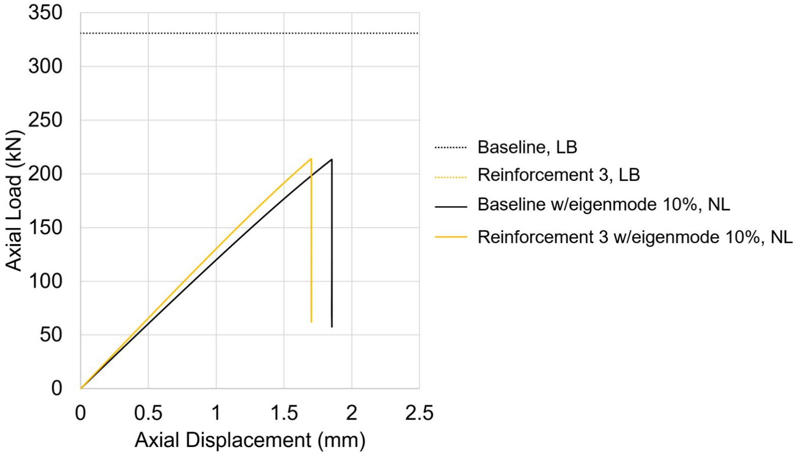

Figure 4.3: Eigenvalue buckling load (LB) and nonlinear response (NL) for the composite conical-cylindrical shell with different transition-region reinforcement layups including imperfections. The eigenvalue buckling load is extended as a dashed line over the horizontal axis for comparison purposes with the peak load of the non-linear response.

4.3. EXPERIMENTAL VALIDATION ON THE BUCKLING BEHAVIOR OF A CONICAL-CYLINDRICAL SHELL WITH REINFORCEMENT

4.3.1. DESCRIPTION OF TEST ARTICLE

Two layers of Toray plain-weave fabric T1100G 3960 PW [79] were adhered to the IML surface of 3CHELL in the region indicated by the box in Figure 4.4a using an autoclave cure process. The fabric plies were placed so that the 0-degree orientation aligned with the axis of rotation of the test article. The reinforcing fabric was placed on the IML because the test article OML surface had been painted for digital image correlation (DIC), which was used to collect displacement and strain data during the test of 3CHELL. The design details for the reinforcement are shown in Figure 4.4b, where the acreage region is the original 3CHELL layup, and ply 1 and ply 2 consisted of the plain-weave fabric. The fabric was approximately 0.20 mm thick. Ply 2 covered ply 1 with a 6.35 mm overlap on the top and bottom. Not pictured is a layer of film adhesive FM 209-1 [80] which was 0.25 mm in thickness and was placed between the acreage and the added fabric plies. The transition region had a compound curvature so each ply and film adhesive was cut into 8 sections to reduce the amount of wrinkling. The seams for fabric ply 1, fabric ply 2, and the film adhesive were staggered. A picture of the cured reinforcement plies as viewed axially upwards is shown in Figure 4.5. The assumed moduli for the fabric is presented in Table 4.3. The Poisson's ratio was estimated to be 0.05 based on references [81, 82, 83].

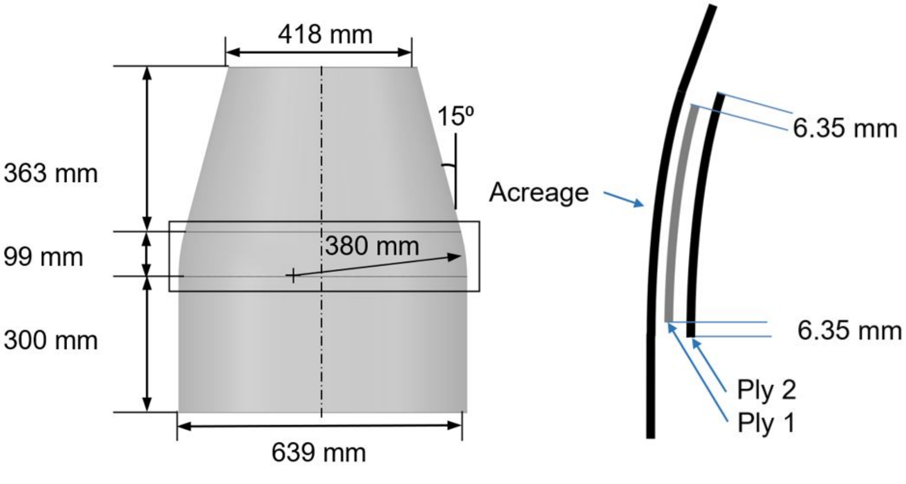

(a) (b)

Figure 4.4: Re3CHELL a) dimensions and location of reinforcement, and b) reinforcement detail.

Figure 4.5: Close up image of the reinforcement after cure.

Table 4.3: Nominal lamina properties of T1100G 3960 PW composite.

0-degree modulus E_{11} (GPa)	90-degree modulus E_{22} (GPa)	Shear modulus G_{12} (GPa)	Poisson's ratio ν_{12} (-)
77.9	86.9	5.1	0.05

The shape of test article Re3CHELL was measured in the same manner as 3CHELL, using the structured light scanning photogrammetry method after the cure of the additional reinforcement plies to determine the IML and OML radial imperfections and thickness variations. The IML and OML radial imperfections are presented in Figure 4.6a where the cooler colors represent relatively inward imperfection, and the warmer colors represent a relatively outward imperfection. The overall peak-to-peak amplitude of the radial imperfection was approximately 1.50 mm, which was slightly larger than the overall thickness of the laminate at 1.37 mm.

The measured thickness is shown in Figure 4.6b, and the red band at the transition region corresponds to the added thickness from the reinforcing fabric plies. Red hatched lines, corresponding to an increased thickness region, were observed in the conical region of the shell. These lines relate to the overlapped areas of the ±45-degree plies. Each course of composite unidirectional tape was laid from the cylindrical end to the conical end. In the cylindrical region of the shell, one course contained four tows of unidirectional tape. To ensure no gaping occurred between tows while transitioning from the cylinder to the tapered conical end, adjacent courses overlapped by a full tow width of 6.35 mm. The overlapped area increased from the bottom towards the conical end until the red lines abruptly end near the top of the cone. At this location, the tow of the currently laid course has overlapped an entire tow width of the adjacent course that was previously laid, and the overlapping composite tow was dropped. The course continues up the length of the conical region with three tows remaining.

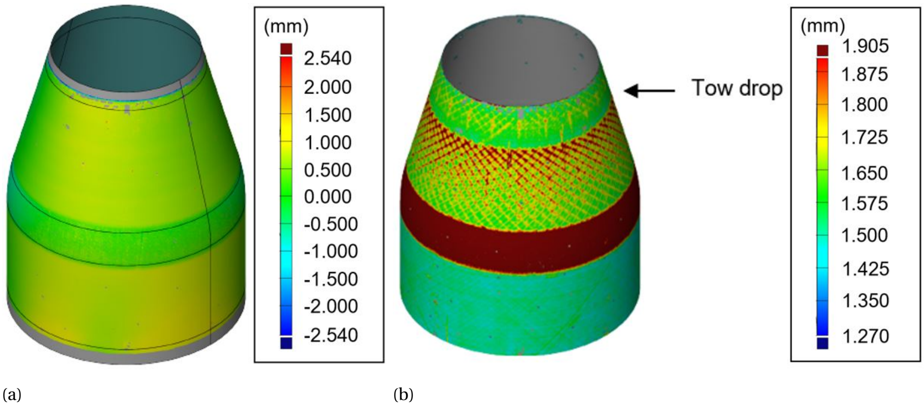

(a) (b)

Figure 4.6: Structured light scan data of Re3CHELL: a) radial imperfections of IML; b) measured thickness.

4.3.2. NUMERICAL ANALYSIS USING UPDATED 3CHELL FEM AND RE3CHELL FEM

A FEM of Re3CHELL was created in Abaqus 2021 [62] by modifying the original 3CHELL FEM to account for the additional fabric plies. Both FEMs consisted of the four-node, reduced-integration shell element, S4R, with the same element size. Additionally, geometric nonlinear analyses were completed to determine the buckling load for both models. The geometric nonlinear analysis was completed using the dynamic implicit solver approximating a quasi-static response, in which the axial displacement rate was 0.076mm/min. The measured IML radial imperfections were also included. From the original test and analysis correlation of 3CHELL, it was determined that the discrepancy between the test data and the FEM was largely due to assumptions made when incorporating the ±45-degree plies tow overlaps.

It was not until after the test of Re3CHELL that it was learned that the program used to control the AFP robot, Vericut Composite Programming (VCP) [84] provided by CGTech[1], can be used to estimate parameters such as the tow overlaps per ply. Comparing the VCP output to the original FEM, the VCP estimate of overlapped areas from the ±45-degree tows was approximately 28% greater than what was assumed in the original 3CHELL FEM. Additionally, the original model assumed that there were no regions with overlapping 0-degree tows, however the VCP estimated an area associated with 0-degree-tow overlaps.

Once VCP was used to estimate the overlaps, the original 3CHELL FEM was updated to reflect the larger predicted overlapped area. This new FEM will be referred to as the updated 3CHELL model. To account for the additional ±45-degree overlaps, more elements in the FEM were assigned the section properties inclusive of the +45 and -45 overlaps. The pattern of the overlapped tows was similar to the original 3CHELL FEM, but the yellow and red areas corresponding to the overlapped +45-degree and –45-degree plies, respectively, extend all the way to the top of the transition region. The updated 3CHELL FEM with newly defined section properties is shown in Figure 4.7a and listed in Table 4.4. Additionally, a new section was defined to account for the overlapped 0-degree is shown in magenta. Since the 0-degree overlapped areas are concentrated towards the conical end due to the shrinking diameter, the region above the tow drop was modified. The 0-degree overlapped area specified by VCP was 16% of the magenta region. To account for the increase in overlapped area, the thickness of the 0-degree plies was increased by 16% from the as-measured thickness of 0.171 mm to 0.185 mm. These modifications increased the 3CHELL FEM weight from 3.31 kg to 3.34 kg, which was closer to the measured weight of 3.40 kg. The area of the overlapped regions, as determined by the VCP program, are compared in Table 4.5 with what was assumed in developing the original 3CHELL model and the updated 3CHELL model.

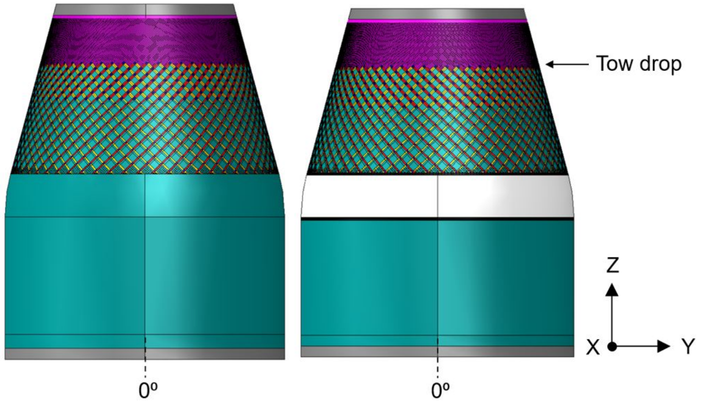

(a) (b)

Figure 4.7: Finite element models: a) updated 3CHELL; b) Re3CHELL.

Table 4.4: Added section properties of the updated 3CHELL and Re3CHELL FEMs.

Section	FEM Color	Layup
Acreage w/modified 0-ply	Magenta	[45/-45/90/0/0/90/-45/45]
Padup- 2 plies	White	[45/-45/90/0/0/90/-45/45/Film adhesive/T1100/ T1100]
Padup- 1 ply	Black	[45/-45/90/0/0/90/-45/45/Film adhesive/T1100]
Potted ends	Gray	[Al ring/Potting/Acreage/Potting/Al ring]

Table 4.5: Section properties of the original 3CHELL.

Ply	VCP	Original 3CHELL FEM	Updated 3CHELL FEM
±45-degree overlaps	0.39 m^2	0.28 m^2	0.40 m^2
0-degree overlaps	0.03 m^2	0.00 m^2	0.03 m^2

The main difference between the updated 3CHELL FEM and the Re3CHELL FEM was the inclusion of the reinforced regions shown in black and white in Figure 4.7b. The white region has film adhesive and two plain weave fabric plies on the IML. The black region has the film adhesive and only one fabric ply. For all FEMs, the positive global X-axis of the FEM aligns with the 0-degree circumferential location of the test article, the positive global Y-axis aligns with the 90-degree circumferential location of the test article, and global Z axis is defined along the axis of rotation. In all models, the measured IML radial imperfections were incorporated into the FEM because the OML data was highly influenced by the thickness variations that were primarily due to the tow overlaps.

The updated 3CHELL FEM and the Re3CHELL FEM contained two reference points on the top and bottom of the test article centered along the axis of rotation. Tie constraints were used to connect all degrees of freedom to the respective reference points. The top reference point had all rotational degrees of freedom fixed. The primary source of loading was due to an applied axial displacement (Z-axis), but it was observed that the load platen applied a shearing displacement in the X-Y plane during the test of 3CHELL. Therefore, the X and Y translational degrees of freedom were not fixed to account for the measured shearing displacement. The bottom reference point had all degrees of freedom fixed. A geometrically nonlinear implicit dynamic analysis was used to predict the buckling response of 3CHELL and Re3CHELL.

4.3.3. EXPERIMENTAL SETUP

The experimental setup and instrumentation for 3CHELL and Re3CHELL were identical. The test article was instrumented and was subjected to several subcritical load sequences prior to the final load sequence to failure. Instrumentation included strain gages, and low-speed and high-speed DIC systems were used to monitor the test article prebuckling, buckling, and postbuckling response throughout all load sequences.

The test article was covered with a high-contrast speckle pattern for DIC to accommodate two different fields of view (global and local). The global field of view was used for the low-speed and high-speed cameras centered at the 0-degree and 180-degree circumferential locations and encompassed the entire length of the test article including the end rings, approximately 711 mm × 864 mm. The cameras used to capture the entire test article and interface rings will be referred to as the global systems. A smaller, more localized field of view was defined with additional low-speed cameras positioned at the 0-, 90-, 180-, and 270-degree circumferential locations. The local field of view encompassed a smaller area, approximately 297 mm × 365 mm, and focused on the transition region. Due to the fact that the local camera systems had smaller fields of view, higher spatial resolutions (pixel/mm) could be obtained without interfering with the data being collected by the global camera systems. The local field of view was chosen because it was anticipated there would be high strain gradients in this region due to the curvature and ply drops from the added reinforcement. A more detailed description of the test setup can be found in Chapter 3.

4.3.4. RESULTS AND DISCUSSION

The test and analyses correlation for the test article 3CHELL using the updated 3CHELL finite element model based on manufacturing data output from the VCP program is discussed in this section. Next, the results for Re3CHELL are presented in this section followed by a comparision of the buckling behavior of 3CHELL and Re3CHELL.

UPDATED 3CHELL RESULTS

A comparison of the load versus displacement data up to and including the buckling limit point of the updated 3CHELL FEM, and the test data is presented in Figure 4.8. The test article 3CHELL buckled at a load of 251.8 kN. The updated 3CHELL model with included measured radial imperfections and the X-Y plane shearing displacement from the load frame had a predicted buckling load of 247.2 kN, which was within 2% of the measured buckling load. The inclusion of radial imperfections reduced the predicted buckling load by 5%. While, the predicted and measured buckling loads were similar, the predicted and measured stiffness are not well aligned. However, it was suggested in [78] that the difference between the FEM stiffness and the measured stiffness was potentially attributable to a gap between 3CHELL and the bottom surface of the end ring. The presence of such a gap could not be verified because the end rings were never removed, so no additional effort was made to determine the source of change in stiffness. The updated 3CHELL model predicted the initiation of buckling in the cylinder just below the transition region at the 0-degree circumferential region, as shown in the predicted radial displacement plots, Figure 4.9. The cooler colors (e.g., blues and blacks) represent relatively inward displacement, and the warmer colors (e.g., reds and orange) represent relatively outward deformation. During the testing of 3CHELL, buckling also initiated in the cylinder just below the transition region, but at approximately the 125-degree circumferential location (circled) instead, as shown in the radial displacement plots in Figure 4.10.

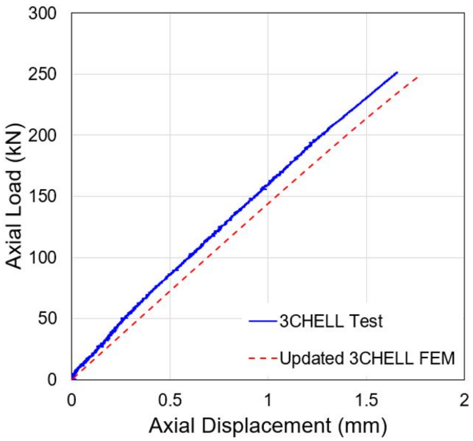

Figure 4.8: Axial load versus axial displacement curves from test and updated 3CHELL FEM.

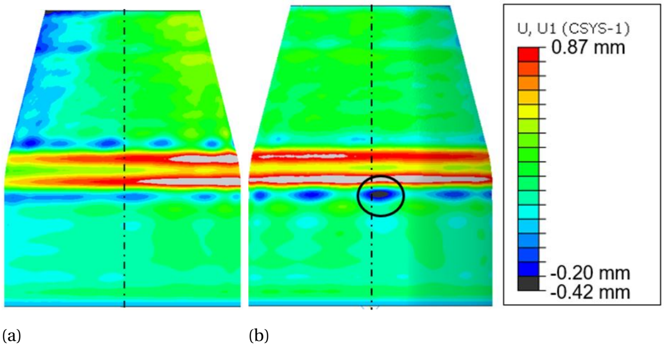

Figure 4.9: Predicted radial displacements (U_1) from updated 3CHELL FEM:
a) centered at 0 degrees; b) centered at 180 degrees.

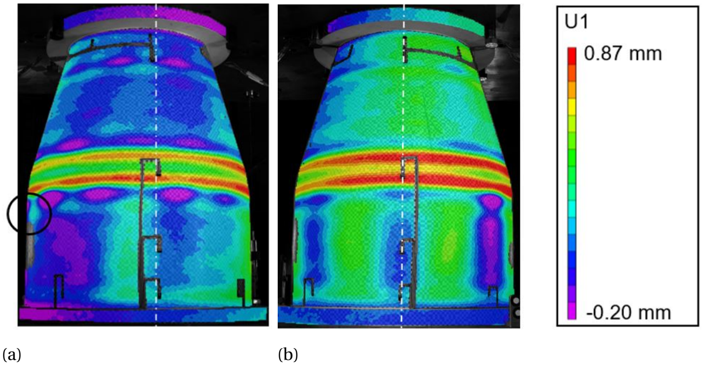

Figure 4.10: Measured radial displacements (U_1) of 3CHELL:
a) centered at 0 degrees; b) centered at 180 degrees.

RE3CHELL RESULTS

The test article Re3CHELL buckled at a load of 268.7 kN and its post-buckled configuration is shown in Figure 4.11. The load versus displacement curves up to and including the buckling limit point from the test data and the Re3CHELL FEM are presented in Figure 4.12. Re3CHELL was predicted to buckle at 304.5 kN without measured radial imperfections (dashed red curve), and 275.5 kN with IML measured radial imperfections (green curve). The inclusion of measured radial imperfections led to a reduction in the buckling load of 9.5%. This reduction was greater than the predicted decrease in load-carrying capability due to imperfections for 3CHELL, which was only 5%. As in 3CHELL, the load frame caused the top load platen to move perpendicular to the test article axis of rotation in the X-Y plane. This resulted in a shearing displacement measured at the top of the test article. This shearing displacement had a magnitude of 0.28 mm towards the 34-degree circumferential location. This shearing displacement and the radial imperfections resulted in a predicted buckling load of 275.2 kN (black curve), which was within 2.5% of the tested load (blue curve).

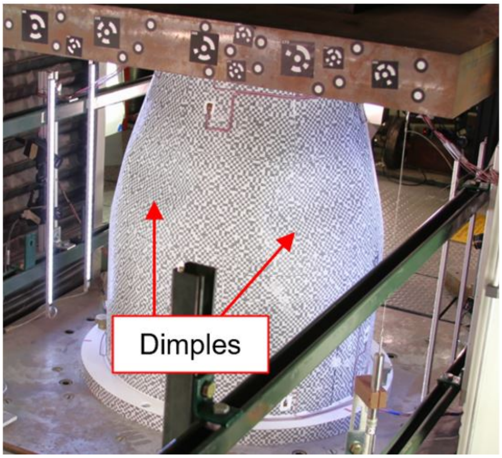

Figure 4.11: Postbuckling configuration of Re3CHELL.

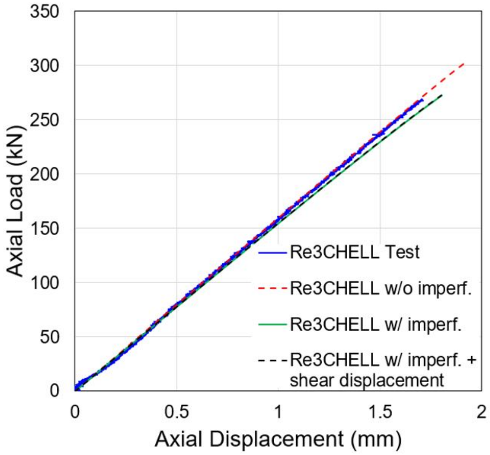

Figure 4.12: Axial load versus axial displacement curves from test and Re3CHELL FEM.

Using high-speed DIC, it was confirmed that buckling occurred approximately at the 125-degree circumferential location at an axial position just above the tow drop in the conical region. The progression of the experimental buckling event is shown in Figures 4.13a to 4.13f using a sequence of data from the high-speed DIC system centered at the 0-degree circumferential location. In Figure 4.13, the warmer colors represent relative outward displacements, and the cooler colors represent relatively inward displacements. In Figure 4.13a, initiation of buckling is observed in the upper left-hand corner of the image, near the conical end, where the edge of a purple dimple can be observed (circled). Approximately 0.5 ms after that, as shown in Figure 12a, a secondary dimple forms adjacent to the first (Figure 4.13b). Then, 2.0 ms after the first image, buckling has propagated with a series of buckling waves around the entire top circumference of the conical section (Figure 4.13c). Figure 4.13 was taken 5.5 ms after the first image and shows a second row of dimples forming just below the first. In Figure 4.13e, the newly formed row of dimples has become larger, while the first row become smaller. Eventually, postbuckling equilibrium was reached in the final image (Figure 4.13f), which is consistent with Figure 4.11.

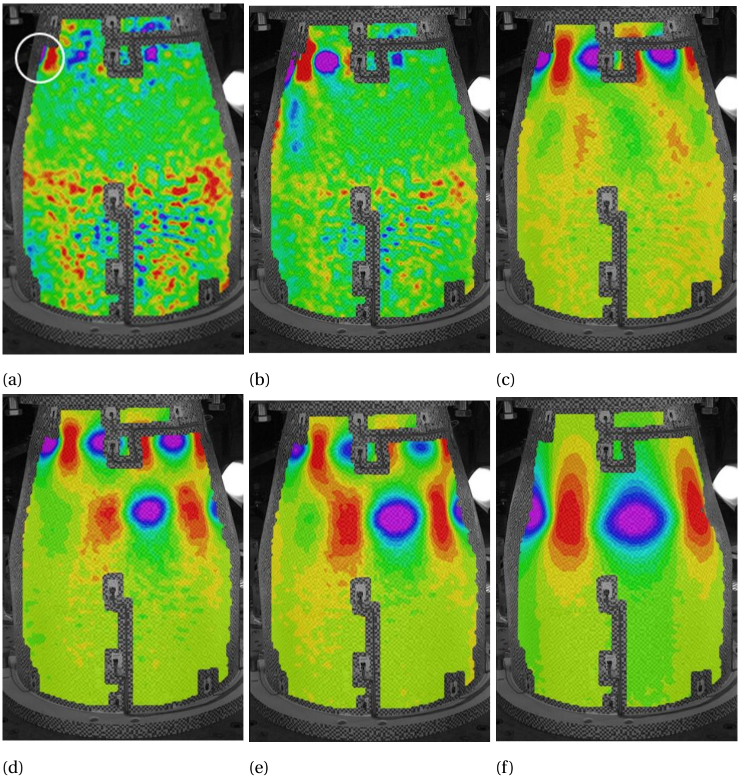
(a) (b) (c) (d) (e) (f)

Figure 4.13: Radial displacement after buckling initiation from high-speed cameras at 180 degrees beginning at a) first image; b) 0.5 ms after first image; c) 2.0 ms after first image; d) 5.5 ms after first image; e) 6.5 ms after first image; f) last image captured.

The predicted and measured radial displacements (U1) at incipient buckling for Re3CHELL are shown in Figure 4.14 and Figure 4.15, respectively, with the buckling location circled. Buckling was predicted to occur in the conical region above the tow drop just outside of the DIC field of view at approximately the 90-degree location, which is shown in Figure 4.14c for clarity. This was similar to the location that buckling was observed to initiate in Re3CHELL as determined using the high-speed DIC data. Buckling initiated just out of the field of view of the high-speed cameras, and it was therefore difficult to confirm the exact location. Similar patterns can be observed in the predicted and measured radial displacements, most notably the inward deformations in the blue just above the tow drop in the conical section and the maximum outward displacement at the transition region. The measured maximum outward displacement was 0.63 mm, as measured by the DIC system centered about 0-degree circumferential location (Figure 4.15a). For the same field of view centered about 0-degrees in the FEM (Figure 4.14a), the predicted maximum outward displacement was 0.60 mm. The minimum inward displacement occurs just above the tow-drop region. The measured inward deformation was 0.38 mm, as observed in the DIC system centered about 180 degrees (Figure 4.15b).

In the same field of view for the FEM (Figure 4.14b), the predicted inward displacement was 0.19 mm. The predicted inward displacement was half of the measured inward displacement; however, both occur in a dimple in the tow drop region. One difference that can be observed occurs where the reinforcement ply 1 was terminated just above and below the transition region. In the FEM, there was a sharp gradient of outward radial displacement (red bands) where the reinforcement ply ends. This is not observed in the measured radial displacements.

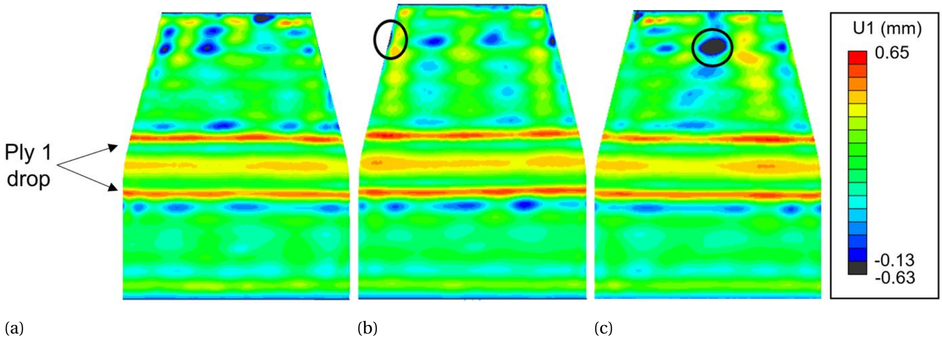

(a) (b) (c)

Figure 4.14: Predicted radial displacements (U_1) from Re3CHELL FEM:
a) centered at 0 degrees; b) centered at 180 degrees; c) centered at 90 degrees.

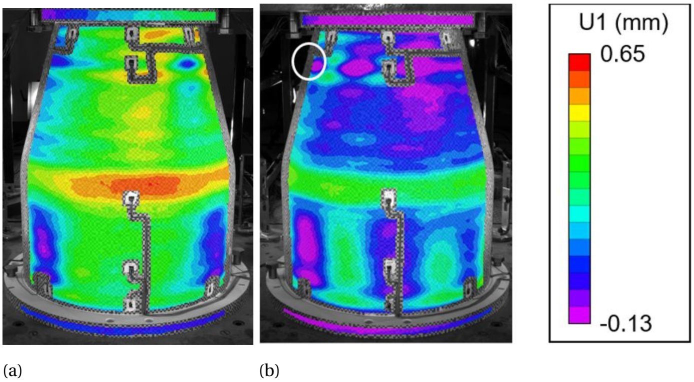

(a) (b)

Figure 4.15: Measured radial displacements (U_1) of Re3CHELL:
a) centered at 0 degrees; b) centered at 180 degrees.

The predicted and measured minimum principal strains at the onset of buckling, with the corresponding in-plane principal strain direction primarily aligned in the axial direction for the current work, are presented in Figures 4.16 to 4.18. There was a red band of low minimum principal strain at the transition region in both predicted and measured results. Also, at the conical end there was a band of green which corresponds to a higher axial strain. The greatest predicted minimum principal strain was -5749 $\mu\varepsilon$, which was about 60% higher than the greatest measured minimum principal strain of -3560 $\mu\varepsilon$. The stiffness discontinuities due to the tow drops in the FEM led to an artificially high strain in the predicted results, which may be a contributing factor as to why the difference between the measured and predicted minimum principal strains was observed.

The spatial resolution of the local DIC systems was 3.5-times higher than the global system, meaning there were more pixels per millimeter in the field of view. This means that the local systems could accurately capture areas with high strain gradients, such as the tow drop region and the transition region. The field of view of the local systems did not include the tow drop region, but it did include the transition region. The area boxed in Figures 4.16b and 4.17b corresponds to the field of view of the local DIC system centered at 180 degrees. The high strain gradients predicted are presented as thin circumferential bands that extend outward from the transition region red to green to gray (Figure 4.16) and are not visible in the data from the global DIC systems (Figure 4.17). Although, the high strain gradients can also be observed in the results from the local DIC systems in Figure 4.18. The image on the left in Figure 4.18 is the area in the black box in Figure 4.16, and the image on the right is the local view of the test article. Two strain gages, SG1 and SG2, can be observed in the local view of the test article. Two areas are highlighted in Figure 4.18 that correspond to high stress gradients in the FEM that were measured by the local DIC systems, but not the global systems.

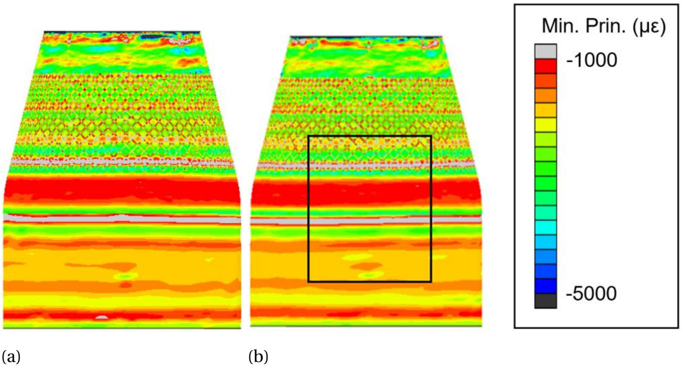

Figure 4.16: Predicted minimum principal strains from Re3CHELL FEM:
a) centered at 0 degrees; b) centered at 180 degrees.

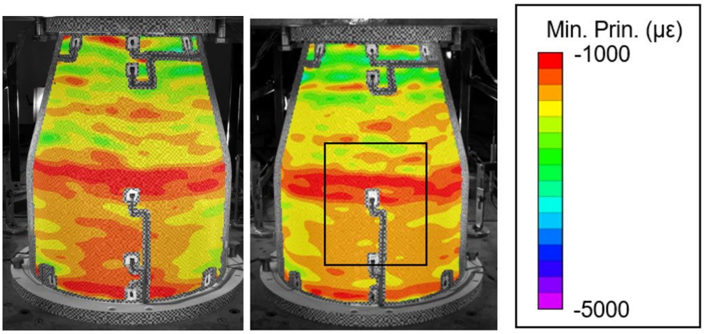

(a) (b)

Figure 4.17: Measured minimum principal strains from Re3CHELL FEM:
a) centered at 0 degrees; b) centered at 180 degrees.

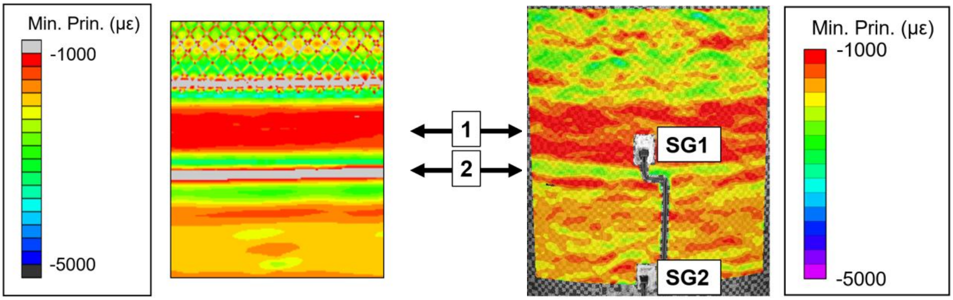

(a) (b)

Figure 4.18: Minimum principal strains from a) Re3CHELL FEM,
and b) measured from local low-speed DIC system at 180 degrees.

As mentioned previously when reporting the values of minimal principal strain, the discrepancy between the measured and predicted values was most likely due to the stiffness discontinuities in the FEM. It was demonstrated that using the local DIC systems with the higher spatial resolution could more accurately measure high strain gradients, which can improve correlation when directly comparing the measured DIC data to the predicted FEM.

Evaluating the strain gage data can also provide valuable information on the correlation between test and analysis. The strain data presented is for the gages SG1 and SG2 and appear in the local system field of view in Figure 4.18. The calculated axial membrane strain data from the OML and IML strain gages in the transition region (SG1) and cylinder at 180 degrees (SG2) is presented in Figure 4.19. There was only a 3% difference between measured and predicted axial membrane strains at incipient buckling (-1380 $\mu\varepsilon$ and -1426 $\mu\varepsilon$, respectively) at the cylinder mid-height gages. There was 6% difference between the measured and predicted axial membrane strains at incipient buckling of -1739 $\mu\varepsilon$ and -1847 $\mu\varepsilon$, respectively, at the transition strain gage. The slopes of the predicted and measured data are in good agreement.

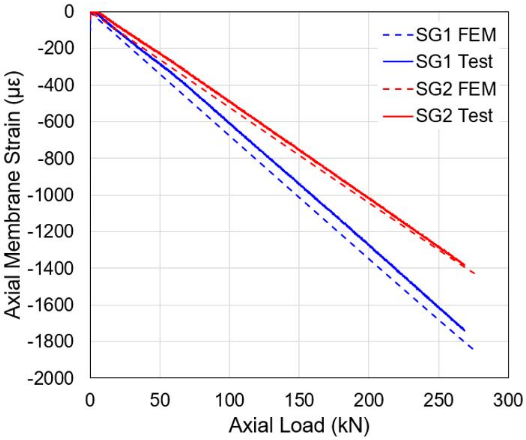

Figure 4.19: Calculated axial membrane strain from the test and FEM for the midheight cylindrical strain gages (SG1) and the transition strain gages (SG2) at 180 degrees.

The predicted and measured maximum principal strain contour plots at incipient buckling are shown in Figures 4.20 and 4.21, respectively, and the highest principal strain occurs near the transition region where the hoop strain was the greatest, as shown by the green-yellow band. The maximum measured principal strain was 2215 $\mu\varepsilon$ in the center of the transition region in the global DIC system, centered about 180 degrees (Figure 4.21b). The predicted strain in the same corresponding region was 2652 $\mu\varepsilon$, which was 20% greater (Figure 4.20b). The predicted maximum principal strain was located in the area of the ±45-degree tow overlap termination at the base of the cone and where the reinforcement ply 2 was dropped. The abrupt changes in the thickness results in a stiffness discontinuity similar to what was observed in the predicted minimum principal strain (Figure 4.16). This may have contributed to the large difference between the predicted maximum principal strains and the maximum principal strains measured by DIC.

Better correlation can be observed in Figure 4.22 when looking at the measured and predicted hoop-direction membrane strains at discrete locations corresponding to the same set of strain gages in Figure 4.18. There was a 10% difference in the hoop membrane strain from the analysis and test at incipient buckling for both sets of gages in the transition region (SG1), and the cylinder midheight (SG2). There was good agreement in the slopes of the measured and predicted minimum principal strain for the cylinder midheight gages (SG2). On the contrary, the calculated hoop membrane strains in the transition region (SG1) for the measured and predicted curves began to diverge around 75 kN.

Overall, the correlation between test and analysis for 3CHELL using the updated 3CHELL FEM and Re3CHELL creates confidence in the ability to predict the buckling behavior of composite conical-cylindrical shells. The experimentally correlated finite element model provides an additional data point for further developing a buckling design methodology for conical-cylindrical shells by demonstrating the ability to predict the buckling behavior for two different designs.

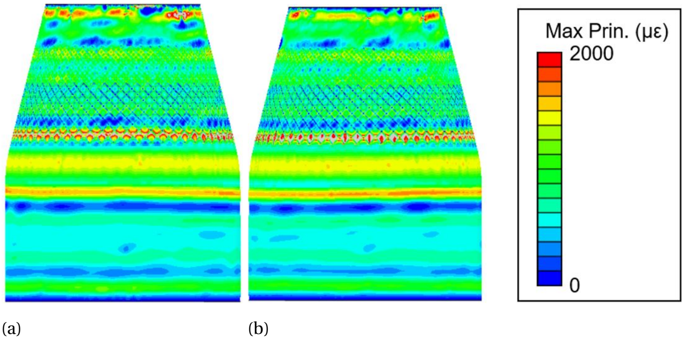

Figure 4.20: Predicted maximum principal strains from Re3CHELL FEM:
a) centered at 0 degrees; b) centered at 180 degrees.

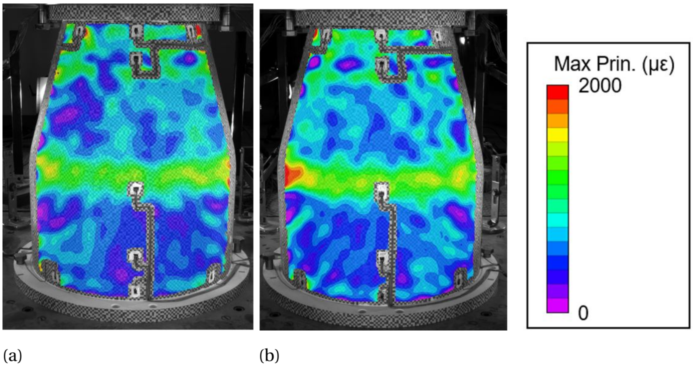

Figure 4.21: Measured maximum principal strains from Re3CHELL:
a) centered at 0-degrees; b) centered at 180-degrees.

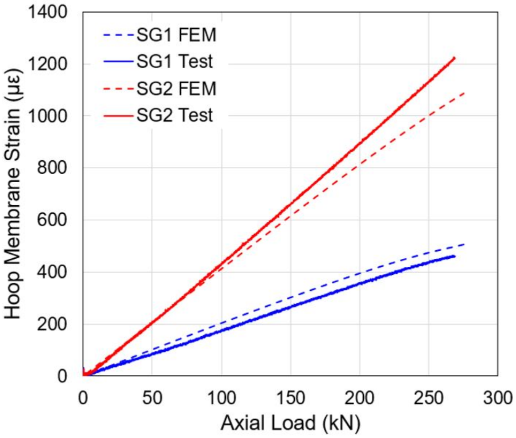

Figure 4.22: Calculated hoop membrane strain from the test and FEM for the midheight cylindrical (SG1) gages and the transition gages (SG2) at 180 degrees.

4.3.5. 3CHELL VERSUS RE3CHELL

The testing of 3CHELL and Re3CHELL provided valuable information on the buckling behavior for composite conical-cylindrical shells to help establish design guidelines, but it also validates observations on the buckling behavior of conical-cylindrical shells made from the numerical study. Specifically, conical-cylindrical shells without reinforcement in the transition region are more inclined to have a reduction in buckling load by including the effects of large displacements and rotations, i.e., geometric nonlinearity, but they are less sensitive to radial imperfections. The opposite is true for conical-cylindrical shells with reinforcement in the transition region, where the increased stiffness of the transition region prevents large displacements and rotations from occurring and the geometrically nonlinear buckling load is close to the eigenvalue buckling load. As a result, the shells with transition-region reinforcement are more sensitive to geometric imperfections than those without reinforcement. To that end, the anticipated gains in the buckling load by adding reinforcement with the intent to increase buckling performance may not be achievable due to the increase in imperfection sensitivity.

The effect of adding reinforcement to the transition region can also be observed when comparing the average axial membrane strain along the length of 3CHELL and Re3CHELL (Figure 4.23). The axial membrane strains were calculated by averaging the OML and IML gages. The axial membrane strains at each strain gage axial location were averaged and plotted for 3CHELL (black) and Re3CHELL (red). For this plot, positive axial membrane strains correspond to compressive strains. As can be seen in 4.21, the axial membrane strains in the cylindrical regions for 3CHELL and Re3CHELL were similar. The variation in the axial membrane strain in the cylindrical region was within 100 $\mu\epsilon$. It is interesting to note that 3CHELL buckled in the cylinder region, and the axial membrane strains in the cylinder were lower than the conical region strains. For comparison, in 3CHELL the average axial membrane strain in the conical region at the 650 mm was 50% higher than the axial membrane strains in the cylindrical region at the axial height of 137 mm. Adding reinforcement resulted in lower axial membrane strains in the conical region of Re3CHELL and buckling occurred in the middle-conical region. The average axial membrane strain in the conical region at the axial position of 650 mm, is within 300 $\mu\epsilon$ (or 15%) of the cylindrical axial membrane strain at 137 mm.

The observation that adding reinforcement to the transition region may not increase the buckling load a significant amount can be verified when comparing the mass to the experimental load for Re3CHELL and 3CHELL. The tested Re3CHELL buckling load was 6.2% higher than 3CHELL tested buckling load, 268.7 kN and 251.8 kN, respectively. The reinforcement added to create Re3CHELL increased the total mass by 5% of the test article as compared to 3CHELL. A structural efficiency of the test articles can be calculated by dividing the tested buckling load by the mass. Based on the experimental buckling load, the structural efficiency was 74.1 kN/kg for 3CHELL and 75.3 kN/kg for Re3CHELL. Therefore, adding the reinforcement resulted in only a minor increase in efficiency of 1.4%. According to the buckling loads from the geometrically nonlinear analyses without radial imperfections, it was predicted that by adding reinforcement to 3CHELL to make Re3CHELL the buckling load with increase from 261.3 kN to 304.5 kN, respectively. Based on these values, it would seem that an 11% increase in load per unit mass could be achieved when radial imperfections were not included. According to the

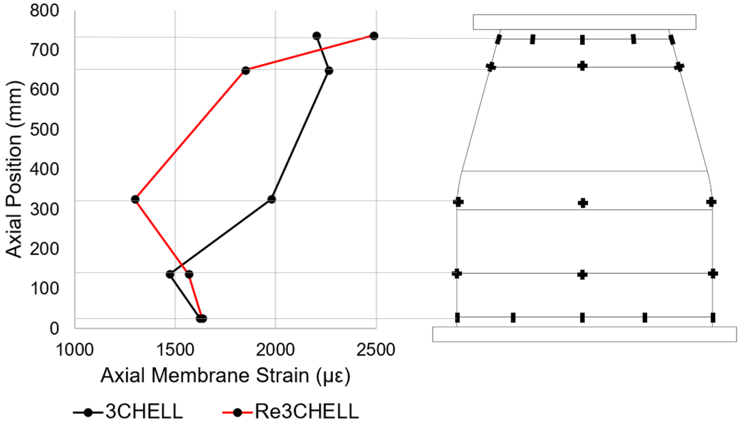

Figure 4.23: Average axial membrane strains for 3CHELL and Re3CHELL and 240 kN.

test data, the added reinforcements only provided an increase of 1.4% because of the increase in imperfection sensitivity. The experimental results demonstrate that it may not be beneficial to add reinforcement to conical-cylindrical shells to increase the buckling load.

4.4. CONCLUDING REMARKS

Conical-cylindrical shells have been used in the aerospace industry as launch vehicle stage adapters and payload adapters and can be susceptible to buckling. Though conical-cylindrical shells are being used in practice, there is little buckling design guidance publicly available. To develop buckling design guidance for conical-cylindrical shells, the ability to accurately predict the buckling behavior of composite conical-cylindrical shells must be demonstrated. The successful test and analysis correlation of a composite conical cylindrical shell with and without reinforcement was presented in this chapter. Additionally, previous analysis-based observations that adding reinforcement to the cylinder-to-cone transition region may not significantly increase buckling load-to-mass ratio was validated with experimental testing, and therefore care should be taken when adding reinforcement with the intent of increasing the buckling load.

5

DESIGN SENSITIVITY ANALYSIS OF BUCKLING IN CONICAL-CYLINDRICAL SHELLS USING POLYNOMIAL CHAOS EXPANSION

CONICAL-CYLINDRICAL *shells with a seamless toroidal transition are being utilized as launch-vehicle and payload adapters in aerospace structures due to their intrinsic structural advantages compared to sections joined with traditional methods. However, the buckling behavior under compressive axial loads of this type of monolithic shell has been less extensively studied compared to purely cylindrical or conical structures. To better understand the buckling behavior of conical-cylindrical shells, the polynomial chaos expansion (PCE) method was implemented to quantify the influence of primary design geometric parameters, namely the shell thickness, the radius of curvature of the transition zone, and the angle of the conical section. The PCE method was applied to shells made of isotropic material and anisotropic composites. In the latter case, the influence of the 0-degree-laminae ply fraction on the buckling load was also quantified. The buckling load was determined using two separate methods, namely from a (linear) eigenvalue analysis and a (nonlinear) implicit dynamic analysis. The polynomial expansion obtained from the PCE method provides useful insight into the relative influence of the basic geometric and material parameters on the buckling load and may find use in preliminary design of conical cylindrical shells for launch vehicles.*

5.1. INTRODUCTION

Cylindrical shells and conical-cylindrical shells have been utilized as a primary structure in launch vehicles to support the resultant loads from various phases of flight. The primary structure is responsible for carrying the predominately compressive loads, which makes buckling an important failure mode to be considered when designing launch-vehicle structures. For a given design mode, the buckling load of a structure depends on the geometric and material parameters that control the structural response. Researchers have used various stochastic methods to quantify the effect a given variable has on the buckling response, but mainly for cylindrical shells. If the buckling sensitivities of a cylindrical or conical-cylindrical shell can be quantified with respect to different variables, then the buckling design methodology for launch-vehicle shells structures can potentially be improved.

Researchers have attempted to quantify the effects of material variations and geometric imperfections on the buckling response of cylindrical isotropic shells. For example, Elishakoff and Arbocz [85, 86] investigated the stochastic imperfection sensitivity of a metallic cylinder assuming axisymmetric and nonsymmetric geometric shapes. Stefanou [87] demonstrated that assuming Gaussian distributions for the random input variables may not be conservative based on their research regarding sensitivities of Young's modulus and Poisson's ratio for an isotropic cylinder.

Composite manufacturing introduces a set of variables unique to composite structures. Knowing that the buckling capability of a composite shell could be sensitive to variability in the manufacturing process, Broggi and Schuller [88] used a moving-average technique to account for thickness and material variations based on measured data to demonstrate the scatter in the buckling load. The results showed that the thickness variations can have a significant effect on the buckling load of a composite shell, which is why Kepple, et al. [89] expanded on Broggi and Schuller's research by looking at various stochastic methods for thickness variations. Sadovsky, et. al [90] took a novel approach by linking imperfections to strain energy, and proposed that strain energy be considered as the random variable instead of imperfection shape.

Researchers have used similar stochastic methods specifically for design of aerospace structures. For example, Arbocz and Hilburger [91] presented the application of the Monte Carlo method and the first order second-moment approach to quantify buckling sensitivities. Alfano and Bisagni [92] used the Monte Carlo method to assess effects that material-property and ply-angle uncertainties, loading imperfections, and geometric imperfections have on the buckling load of a composite cylinder. The individual influence of each variable was quantified as well as combined effects from all the variables. Alfano and Bisagni [93] also expanded their work to include composite shells with cutouts. Schillo, et al. [94] performed a similar study, but instead of assuming probabilistic distributions for the variables, they used the actual distributions measured from 11 different test articles; again, the Monte Carlo method was employed.

Polynomial chaos expansion (PCE) is a method that has been used to perform sensitivity analyses and uncertainty quantification [95] on a wide range of applications[96, 97, 98]. Polynomial expansions are used in the PCE method to estimate an output based on random input variables in a way that is computationally less expensive than the Monte Carlo and first-order methods, which require a relatively large number of functional evaluations [99]. Specifically related to the buckling of thin-walled structures, PCE was used to estimate the nonlinear buckling load with geometric imperfections [100]. The PCE method was chosen because only a small number of computationally expensive nonlinear functional evaluations were required. Additionally, Kumar, et al. [101]. demonstrated the use of the PCE method to assist in the material selection and design process of an aircraft fuselage. They considered a multiscale modeling approach, where they propagated the uncertainties from the microscale, into mesoscale and macroscale finite element (FE) models. Additionally, Kumar, et al. demonstrated the ability of the PCE to handle a large number of input variables. Paudel, et al. [102] demonstrated the use of the PCE to perform uncertainty quantification and a global sensitivity analysis of a composite cylinder with geometric imperfections.

In addition to quantifying uncertainty, the PCE method can also be used as a tool for design sensitivity analysis by choosing input design variables with a continuous uniform probability distribution. A uniform distribution, with a chosen design range specified by upper and lower bounds, reflects the arbitrary nature of design choices. This approach is useful for supporting preliminary design choices and, in the present work, it is applied for conical-cylindrical shells. In particular, the PCE approach is used to investigate the influence of basic geometric and material design variables on the buckling load, which is a major driver for design choices. For the purposes of the present study, which is the design sensitivity analysis of the primary design variables, geometric imperfections were not included. Nonetheless, it is relevant to point out that in Chapter 3 and [75] observed that the difference between the linear and nonlinear analyses to predict the nominal buckling load can be significant for conical-cylindrical shells even when geometric imperfections are not included. Correspondingly, separate PCE expressions are developed for the buckling load predicted from a (linear) eigenvalue problem and the buckling load predicted from a (nonlinear) implicit dynamic simulation.

The present work is organized as follows: A brief overview of the PCE method is presented in 5.2. The method is then applied to obtain a PCE representation of the buckling load fitted to values obtained from the linear buckling equation (eigenvalue problem) of an isotropic conical-cylindrical shell. The importance of the order of the PCE expression and oversampling ratio, both of which need to be chosen at the beginning of the process, is studied in 5.3. Subsequently, in 5.4, the same approach is used for the nonlinear buckling load of an isotropic shell. In 5.5, the PCE method is applied for composite (anisotropic) conical-cylindrical shells. Concluding remarks are given in 5.6.

5.2. METHODOLOGY AND APPLICATION

Polynomial chaos expansion, specifically using the nonintrusive point-collocation technique, is a stochastic method where a desired random output variable, y, which depends on p random input variables X_j ($j = 1, ..., p$) is expressed in a series expansion using polynomial basis functions Φ_i ($i = 1, ...$), [95, 103]. The series expansion, denoted as y_{PCE}, is typically truncated using a finite number of terms, N, that capture the most relevant contributions to the actual output variable y. The input variables X_j have specific probabilistic distributions (e.g., uniform, normal, etc.) that best represent their nature. Correspondingly, the output y_{PCE} is expressed as a finite summation, i.e.,

$$y_{PCE} = \sum_{i=0}^{N} \beta_i \Phi(X) \tag{5.1}$$

where the random input variables X_j have been collected in a multivariate vector $\boldsymbol{X}$ and the scalars β_i ($i = 1, ..., N$) are unknown coefficients that need to be determined.

The basis functions Φ_i are obtained by carrying out a tensor product of univariate orthogonal polynomials P_j of each input variable X_j, i.e.,

$$\Phi_i(X) = \prod_{j=1}^{p} P_j^{a_{ij}}(X_j) \tag{5.2}$$

where the integers a^{ij} correspond to the order of the univariate orthogonal polynomial P_j for the orthogonal multivariate polynomial Φ_i. The functions P_j are orthogonal polynomials that are connected to the probability distribution of the input variable X_j. For example, if an input variable X_j has a uniform distribution, the Legendre family of orthogonal polynomials P_j is used, and for normally distributed variables, Hermite polynomials are used.

The coefficients β_i with $i = 1, ..., N$, need to be adjusted such that the expansion y_{PCE} in 5.1 can approximate the output y. To this end, the first step is to obtain a collection of S sampling input points $\boldsymbol{X}^{(s)}$ and known corresponding output values $y(\boldsymbol{X}^{(s)})$, with $s = 1, ..., S$. These sample points can be obtained experimentally or, in the present case, numerically through finite element (FE) simulations. This entails running S simulations, each with a deterministic output. Subsequently, a best-fit analysis is carried out to minimize the difference between the PCE prediction $y_{PCE}(\boldsymbol{X}^{(s)})$ and the actual values $y(\boldsymbol{X}^{(s)})$. Commonly used strategies are least-square formulations and point collocation methods that generate a system of (linear) equations representing the necessary conditions for an optimum match. Correspondingly, the number of sampling points S must be at least equal to the number of approximating terms N in the truncated series, i.e., $S = n_p \geq 1$ is the oversampling ratio.

The number of terms N in the truncated series is dependent upon the number of input variables, p, and the greatest order of the polynomials, n, as $N = (n+p)!/(n!p!)$ (see, e.g., [104] for details). The input variables used in the method, and hence the value p, are chosen a priori based on expert knowledge, a preliminary analysis, or a combination thereof. The oversampling ratio n_p is normally dependent on the availability of existing data and/or the effort required to generate new data. Similarly, the leading order of the polynomial n is chosen based on the available data and resources, where normally higher values may be required to capture complex dependencies between input and output (e.g., rapid changes in rates and nonmonotonic trends). A compromise between available data, resources and accuracy can be reached by first computing the number of sample points, i.e.,

$$S = n_p \frac{(n+p)!}{n!p!} \tag{5.3}$$

then estimating the cost to generate that number of samples (e.g., number of experiments or number of simulations), and finally choosing appropriate values for n, p, n_p for a desired accuracy of y_{PCE}.

A nonintrusive approach is used in the present work to generate data points $y(\boldsymbol{X}^{(s)})$ ($s = 1, \ldots, S$), where $\boldsymbol{X}^{(s)}$ is the buckling load obtained from finite element simulations of a conical-cylindrical shell characterized by design variables X_j treated as uniformly distributed random variables within a design range. A Latin hypercube sampling scheme is used to select a discrete number of input variables based on their distributions. Those inputs are then used to create finite element models (FEMs) to get the desired output for that specific combination of input variables. This is repeated S times. The point collocation method is then implemented where linear systems of equations are used to solve for the resulting coefficients, thus determining the polynomial expansion. The open-source Python package Chaospy [105] was employed to assist in process of solving for the coefficients to determine the resulting polynomial.

5.3. LINEAR BUCKLING OF AN ISOTROPIC CONICAL-CYLINDRICAL SHELL

The process outlined in the previous section is applied to obtain a polynomial expression that can estimate the buckling load of an isotropic, linearly elastic conical-cylindrical shell as determined from an eigenvalue analysis (and hereafter referred to as the linear buckling load). Three design parameters, as shown in Figure 5.1, were chosen as input variables for the linear buckling load, namely:

(i) The wall thickness, t, of the shell (same thickness in both the cylindrical and conical sections),

(ii) The radius of curvature, ρ, of the transition region between the cylindrical and conical sections, and

(iii) The cone angle, α.

For simplicity, the aspect ratio (radius-to-height ratio) of the shell was kept fixed. The accuracy of the polynomial expression (i.e., its capacity to reproduce the actual linear buckling load) was assessed using different goodness-of-fit metrics, such as the determination coefficient, R^2, and plotting the residuals. Once the accuracy was established, a sensitivity analysis was carried out to determine the influence of each variable on the linear buckling load.

5.3.1. INPUT VARIABLES

The conical-cylindrical shells considered in the study had an overall height of 1200 mm that remained constant. Also, the radius of the cylindrical end was 400 mm and was kept constant (Figure 5.1). For design purposes, the radius of curvature of the cylindrical-to-conical transition region was allowed to range from 0 mm, an abrupt transition, to 800 mm, a smooth transition. Additionally, the design range for the conical angle was from 10 degrees to 25 degrees and the wall thickness ranged from 1.27 mm to 2.54 mm. The ranges of interest for the design input variables are summarized in Table 5.1. After the number of evaluations S was chosen, then the Latin hypercube sampling technique was implemented to create the corresponding set of S combinations of t, ρ, and α. In all simulations, the elastic material properties were taken as constant and corresponded to an aluminum alloy with a Young's modulus of 71.0 GPa and a Poisson's ratio of 0.33.

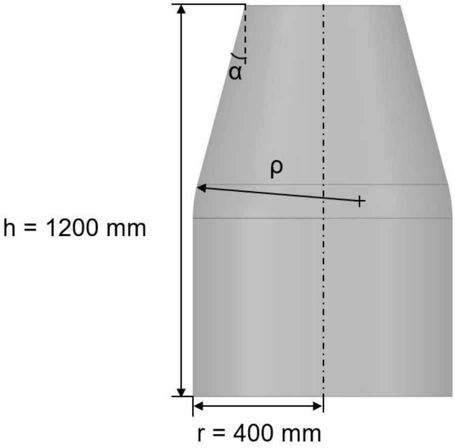

Figure 5.1: Conical-cylindrical shell geometry.

Table 5.1: Design space as described by the input variables and probabilistic distribution.

Variable	Distribution	Range
Thickness (t)	Uniform	Min=1.27 mm Max= 2.54 mm
Radius of curvature (ρ)	Uniform	Min= 0 mm Max= 800 mm
Cone angle (α)	Uniform	Min= 10 degrees Max= 25 degrees

The total number of finite element analyses S required for the PCE expansion, as indicated in 5.3, depends on the number of input variables, p, the largest order of the polynomial, n, and the oversampling ratio, n_p, which may influence the accuracy of the resultant equation. In the current case study, there are three input variables (t, ρ, and α), thus $p = 3$. The oversampling ratio and the order of the polynomial were modified to assess the sensitivity of these two factors on the accuracy of the final polynomial expansion. In general, an oversampling ratio of $n_p = 2$ has been deemed appropriate for many applications. To gain insight on the influence of this parameter, in addition to the commonly used value, an oversampling ratio of $n_p = 3$ was also considered. Similarly, the accuracy of quadratic ($n = 2$) and cubic ($n = 3$) polynomials was also assessed. Three cases, corresponding to different combinations of values of p, n, and n_p are shown in Table 5.2 together with the number of finite element analyses required to generate the sampling points. Increasing the order of the polynomial and/or the oversampling ratio may improve the accuracy of the resulting polynomial, but it comes at an increased computational cost due to the larger number to finite element analyses required. The resulting polynomials from cases 1, 2, and 3 were determined and assessed.

Table 5.2: Parameters for distinct polynomial expansions of the linear buckling load and number of required data points (training data set) for an isotropic conical-cylindrical shell.

Case	Number of variables (p)	Order of equation (n)	Oversampling ratio (n_p)	Number of evaluations (N)
1	3	2	2	20
2	3	2	3	30
3	3	3	2	40

5.3.2. FINITE ELEMENT MODEL

A FEM was created in Abaqus 2021 [62] to determine the linear buckling load for an isotropic conical cylindrical shell. For each training data set of the three cases indicated in Table 5.2, a finite element model was created. Each FEM was meshed using the four-node reduced integration shell element (S4R element type in Abaqus), with an approximate mesh density of one element every 0.5 degrees around the circumference of the cylinder. All degrees of freedom were constrained at a bottom reference node. At the top, all degrees of freedom were constrained, except for translation along the axis of rotation. The Lanczos solver was used to determine the associated eigenvalues. An example of the first eigenmode associated with the first eigenvalue is presented in Figure 5.2. The resultant polynomials can be determined for Cases 1, 2, and 3, once the eigenvalues (i.e., linear buckling loads) are known.

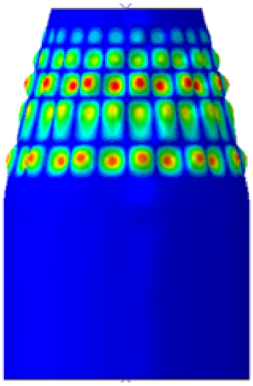

Figure 5.2: Example of a first linear eigenmode.

5.3.3. DETERMINING THE POLYNOMIAL

The PCE representation of the linear buckling load for Case 1 (i.e., assuming an oversampling ratio of $n_p = 2$ and polynomial order $n = 2$), denoted $L_{PCE}^{iso,1}$, requires the determination of $N = 10$ coefficients as indicated in equation 5.3. From the FEM analyses for selected sample points, and after solving the corresponding system of equations for the coefficients, the resulting polynomial expansion is given by

$$\begin{aligned} L_{PCE}^{iso,1} = 204.40t^2 + 0.063\rho t - 9.21\alpha t - 1.17\cdot 10^{-4}\rho^2 + 1.42\cdot 10^{-3}\alpha\rho - 0.44\alpha^2 \\ +258.97t + 3.59\cdot 10^{-3}\rho + 22.22\alpha - 337.58 \end{aligned} \tag{5.4}$$

The accuracy of the polynomial expansion shown in equation 5.4, or the goodness of fit, can be visualized in Figure 5.3a, which shows the linear buckling load L_{PCE} plotted against the buckling loads obtained from solving FEM eigenvalue buckling problems. The dots in the graphic represent the linear buckling loads corresponding to the input design variables used to determine the coefficients of the polynomial expansion (i.e., the training data set). The points in the graph denoted with an x-symbol correspond to independent data that were not used to calibrate the polynomial expansion. This data set is used to validate the accuracy of the polynomial expansion. The gray dotted line has a slope of unity. If a point lies on the line, the linear buckling load L_{PCE} estimated using the polynomial chaos expansion is equal to the buckling load obtained from the FEM simulation. Therefore, the closer the point is to the line, the greater the accuracy.

The resulting coefficient of determination, R^2, for the polynomial obtained in Case 1 is 0.9995. This means there is little variability between the FEM results and the estimates from the polynomial representation 5.4. It can be observed that many training and independent (validation) points are clustered around the gray dotted line in Figure 5.3a. The average error for all Case 1 validation models was 3%. The maximum individual percentual error between the FEM linear buckling load and the validation points was less than 9%. The model with the largest individual percentual error had a radius of curvature of 800 mm, a cone angle of 10 degrees, and a wall thickness of 1.27 mm, which is at the bounds of the considered design space in all three variables (see Table 1). This relative inaccuracy of the design-space boundary highlights some potential sensitivity to results with input variables near the outskirts of the design space. The plot of the residuals (Figure 5.3b) shows no obvious trend. This is also an indication the polynomial representation equation 5.4 is a good fit to estimate the linear buckling load.

For Case 2, the order of the polynomial representation remained the same as for Case 1, while the oversampling ratio was increased to $n_p = 3$, requiring $S = 30$ FEM analyses to determine the $N = 10$ coefficients of the expansion. After training, the corresponding PCE representation for the linear buckling load for Case 2 is given as

$$\begin{aligned} L_{PCE}^{iso,2} = 247.83t^2 + 0.09\rho t - 10.49\alpha t - 1.26\cdot 10^{-4}\rho^2 + 2.00\cdot 10^{-3}\alpha\rho - 0.12\alpha^2 \\ +132.88t - 0.08\rho + 13.36\alpha - 141.09. \end{aligned} \tag{5.5}$$

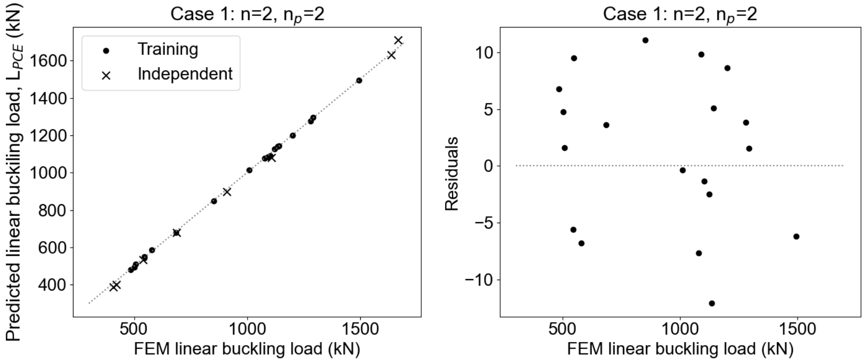

(a) (b)

Figure 5.3: Goodness of fit metrics for Case 1: a) the estimated linear buckling load versus the linear buckling load from FEM; b) plot of the residuals.

The expansion given in equation 5.5 has an R^2 value of 0.9994. The coefficient of determination, R^2, was very similar to the R_2 value of 0.9995 for Case 1. Visualizing the data for Case 2, as shown in Figure 5.4a, reveals similar trends compared to Case 1. For example, the training points and the independent (verification) models follow the line with a slope of unity showing that the estimated linear buckling load is in very good agreement with the FEM output. The average error between verification and predicted values was less than 2%. The largest individual error for the verification models was approximately 5%. The model with the largest error had input variables at the bounds of the design space. Additionally, the residuals are well scattered, and there is no discernible trend (Figure 5.4a).

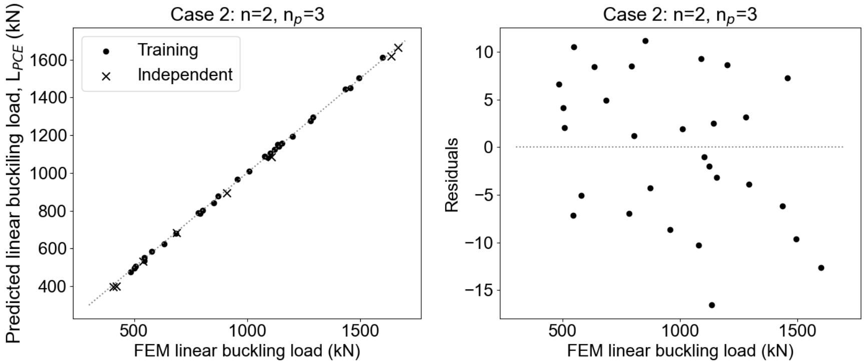

(a) (b)

Figure 5.4: Goodness of fit metrics for Case 2: a) the estimated linear buckling load versus the linear buckling load from FEM; b) plot of the residuals.

For Case 3, the order of the resultant polynomial expansion is cubic, $n = 3$, and the oversampling ratio is $n_p = 2$. Increasing the order of the PCE representation from quadratic to cubic doubled the number of FEM analyses required to $S = 40$. The corresponding cubic polynomial expansion for the linear buckling load requires $N = 20$ terms and is given by

$$\begin{aligned} L_{PCE}^{iso,3} = {} & 40.56t^3 - 0.098t^2\alpha + 0.018\alpha^3 + 1.16\cdot10^{-4}\alpha^2\rho - 1.09\cdot10^{-5}\alpha\rho^2 \\ & -0.016\rho t^2 + 2.98\cdot10^{-7}\rho^3 - 7.44\cdot10^{-4}\alpha\rho t + 1.95\cdot10^{-4}\rho^2 - 4.70\alpha t^2 \\ & -0.024\rho t + 11.95\alpha t - 6.23\cdot10^{-4}\rho^2 + 80.98t^2 + 7.26\cdot10^{-3}\alpha\rho \\ & -1.05\rho^2 + 282.38t + 0.20\rho + 9.07\alpha - 252.03 \end{aligned} \tag{5.6}$$

The PCE representation for the buckling load has an R^2 value 0.9998, which is slightly better than for Cases 1 and 2 (i.e., higher R^2 value for Case 3). The maximum percent error is less than 5% and the average error is less than 2%, which is the same as Case 2 with the oversampling ratio of n_p=3. As for the previous cases, the combination of input variables that resulted in the maximum error corresponded with values close to the limits of the design space. The goodness of fit for Case 3 can be visualized in Figure 5.5a. As with the previous cases, the residual plots are well-scattered (see Figure 5.5b).

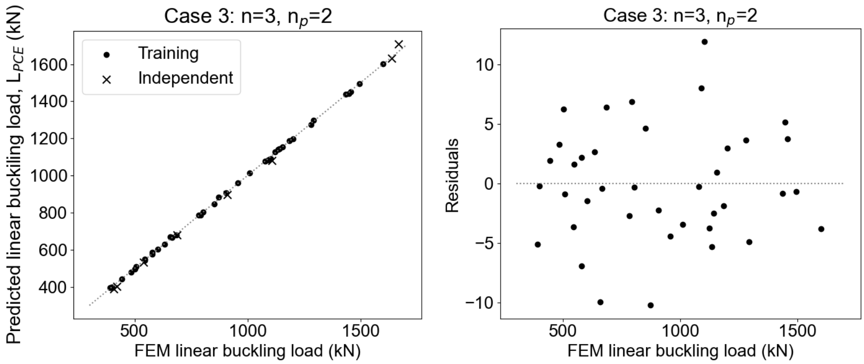

(a)

(b)

Figure 5.5: Goodness of fit metrics for Case 3: a) the estimated linear buckling load versus the linear buckling load from FEM; b) plot of the residuals.

Comparing the average and maximum errors between predicted and validation points for the three cases considered, it can be observed that there is a slight improvement from Case 1 to Case 2 (average from 3% to 2% and maximum from 9% to 5%), but marginal improvement from Case 2 to Case 3. Furthermore, in all cases it was observed that the largest errors were from models where the input variables were close to the edges of the design space. For all cases, the R^2 values were close to 1 and the residual plots were well-scattered. For practical purposes, the expansions shown in equations 5.4, 5.5, and 5.6, which were obtained with different combinations of oversampling ratios or order of polynomials, provide sufficiently accurate PCE representations for the linear buckling load.

5.3.4. SENSITIVITY ANALYSIS

The PCE approach can provide good results for estimating the linear buckling loads of an isotropic conical-cylindrical shell, but one of the most insightful attributes of this polynomial representation is the ability to assess the relative influence that the design variables (t, α, and ρ) have on the buckling load. The total sensitivity index shows the influence of each variable on the buckling load and also accounts for the interaction between variables and it is shown in Figure 5.6, which clearly indicates that the thickness of the shell has the largest influence on the linear buckling load, as expected. The cone angle does have a slight influence, but it is small compared to the wall thickness. The radius of curvature has almost no influence on the linear buckling load compared to the thickness. It is relevant to mention that the relative sensitivities shown in Figure 5.6 depend not only on the choice of the design variables, but also on their design range, which itself depends on design or manufacturing constraints. For example, the range of interest in the present study for the cone angle is from 10° to 25°. It is likely that the relative influence of the cone angle would increase if angles greater than 25° are considered. However, considering a different design range requires generating a new training set, hence the design range must be chosen carefully beforehand to represent the range of interest.

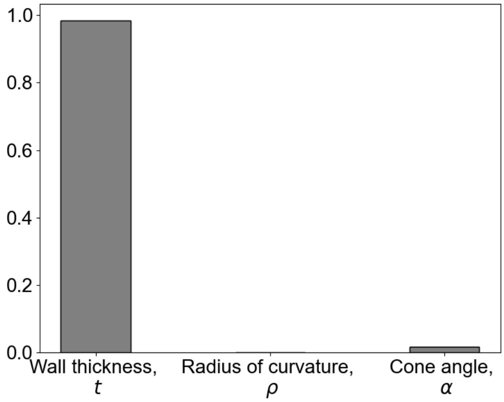

Figure 5.6: Total sensitivity index of the input variables on the linear buckling load of an isotropic conical-cylindrical shell, Case 2.

To further illustrate how the input design variables influence the estimated linear buckling load, it is insightful to plot the PCE representation of the load as a function of each design variable separately for fixed values of the others. In particular, a reference design is chosen with nominal design values in the middle of the individual design ranges, namely a thickness of $t = 1.91$ mm, a radius of curvature in the transition region of $\rho = 400$ mm and a cone angle of $\alpha = 17.5°$. The predicted linear buckling load L_{PCE}, as determined from Case 1 and given in equation 5.4, is plotted in Figure 5.7 about the reference design by varying the wall thickness from 1.27 – 2.54 mm (Figure 5.7a), varying the radius of curvature over the 0-800 mm range (Figure 5.7b) and varying the cone angle from 10° to 25° (Figure 5.7c).

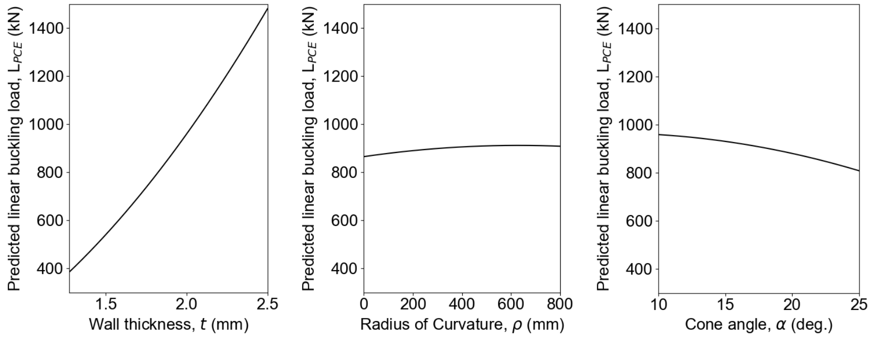

(a) (b) (c)

Figure 5.7: Predicted linear buckling load as a function of each design variable around the reference design (t = 1.9 mm, ρ = 400 mm, α = 17.5°) for (a) variable wall thickness, (b) variable radius of curvature and (c) variable cone angle, Case 2.

From Figure 5.7a, it can be observed that, as the wall thickness is varied from 1.27 mm to 2.54 mm, the linear buckling load increases more than three-fold (an increase from about 400 kN to about 1540 kN). This significant increase is consistent with the high sensitivity index of this variable. From Figure 5.7b, the predicted linear buckling load remains relatively constant as the radius of curvature increases, indicating that the buckling load is relatively insensitive to this parameter. The total variation in bucking load is only about 40 kN over the 0-800 mm range considered for the radius of curvature (from about 840 kN to 880 kN). For the cone angle, as can be observed in Figure 5.7c, there is a slight decrease in the buckling load over the selected design range. The linear buckling load decreased 150 kN as the angle increased from 10° to 25° (from about 930 kN to about 780 kN). This change in buckling load is greater than the change due to varying the radius of curvature as indicated above, but is still small compared to the changes due to variable thicknesses. The next step is to use PCE methodology to assess the influence of the input variables on the buckling load from a geometrically nonlinear analysis.

5.4. NONLINEAR BUCKLING OF AN ISOTROPIC CONICAL-CYLINDRICAL SHELL

The sensitivity analysis carried out in the previous section was based on solving the eigenvalue problem for bifurcation buckling (buckling equation) assuming a geometrically linear deformation up to buckling (linear buckling load). This approach is computationally inexpensive compared to a geometrically nonlinear analysis used to determine a limit point. Nonetheless, there can be a large discrepancy between the buckling load predicted from an eigenvalue problem and from a geometric nonlinear analysis even without imperfections [106]. In general, the linear buckling load may be viewed as an approximation of the geometrically nonlinear buckling load. Consequently, it is of interest to understand the influence of the design parameters ρ, α, and t on the nonlinear buckling load.

As previously noted, the computational cost of solving a nonlinear buckling analysis is significantly higher than the cost of solving an eigenvalue problem, hence a parametric analysis to study the effect of varying the order of the PCE polynomial and the oversampling ratio was not pursued in the nonlinear case. Only Case 1 from Section 5.3, with an oversampling ratio $n_p = 2$, a PCE of order $n = 2$ and using the same three input random variables ($p = 3$) is considered in this section for the nonlinear case. From Table 5.1, this case requires only 20 nonlinear analyses to find the coefficients of the PCE, which is significantly less than Cases 2 and 3. The representation obtained from Case 1 in Section 5.3 was found to be sufficiently accurate for the linear buckling load. Furthermore, it is expected that the trends for the linear and nonlinear cases would be similar since the quality of the fit only depends on the training data itself and not on the method used to generate the data.

The buckling loads for training the PCE were obtained from geometrically nonlinear implicit dynamic analyses implemented in the general-purpose finite element software Abaqus 2021 [62]. A total displacement of 5 mm was applied linearly over a period of 2000 seconds. The boundary conditions and mesh were the same as the linear buckling analyses. The design ranges for the random input variables are the same as the ones indicated in Table 5.1.

The buckling load in a nonlinear analysis may correspond to a limit point (unstable buckling) or may require a criterion to identify a nominal buckling load if the buckling occurs in a stable fashion (continuous transition from slightly buckled to significantly buckled). Not using a consistent method to determine the limit point may produce an inaccurate polynomial. In the present case the buckling load corresponds to the maximum load from the nonlinear analysis. An example of the radial displacements just prior to buckling is presented in Figure 5.8. The gradation from light to dark blue represent areas of relative inward deformation where buckling may initiate. Buckling was predicted to initiate in the conical region for all conical-cylindrical shell configurations.

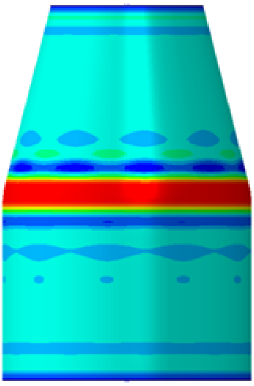

Figure 5.8: Example of radial displacements incipit buckling from a geometrically nonlinear analysis.

After postprocessing the nonlinear simulations chosen from a Latin hypercube sampling, the resultant quadric polynomial N_{PCE}^{iso} representing the nonlinear buckling load is given by

$$N_{PCE}^{iso} = 129.44t^2 + 0.37\rho t - 0.94\alpha t - 5.20\cdot 10^{-4}\rho^2 + 3.20\cdot 10^{-3}\alpha\rho + 0.43\alpha^2 \\ + 25.53t + 0.057\rho - 21.14\alpha + 138.60 \tag{5.7}$$

The R^2 value is in this case is 0.9992 and the visualization of the goodness of fit is presented in Figure 5.9a. The black dots are associated with the training data and the x-symbol associated with validation data. The average error for the validation data is approximately 4%, and the maximum error is 12%. The maximum error corresponded to the sampling input values of t = 1.45 mm, $\rho = 793.4$ mm, and $\alpha = 12.34°$, which are near the bounds of the design space. The residual plot is well-scattered with no obvious pattern (see Figure 5.9b). Overall, the polynomial chaos expansion N_{PCE}^{iso} given in equation 5.6 can be used to estimate the nonlinear buckling load of a conical cylindrical shells with relatively good accuracy in the specified design space.

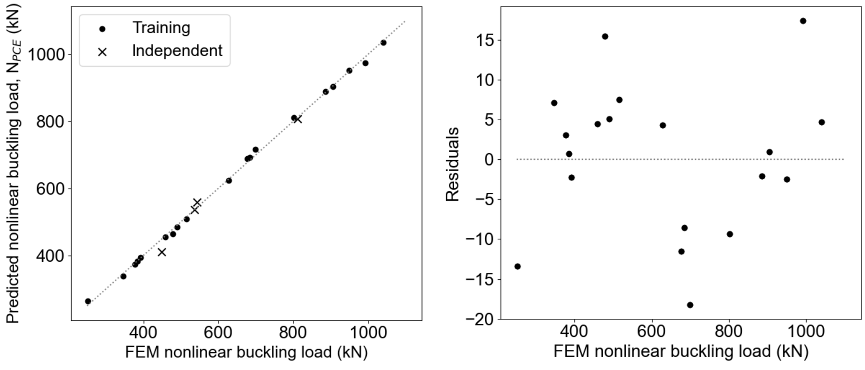

(a) (b)

Figure 5.9: Goodness of fit metrics for the nonlinear buckling load of an isotropic conical-cylindrical shell: a) the estimated buckling load versus the nonlinear buckling load from FEM; b) plot of the residuals.

The total sensitivities of the design variables based on the expansion N_{PCE}^{iso} are shown in Figure 5.10. Similar to the results obtained for the linear buckling load, it can be observed from Figure 5.10 in that the wall thickness has the largest influence when determining the nonlinear buckling load as compared to the radius of curvature and the cone angle. Nonetheless, the radius of curvature of the transition region from conical to cylindrical has a more significant influence on the nonlinear buckling load than it did for the linear buckling load (See Figure 5.6 and Figure 5.10 for sensitivities of radius ρ). The cone angle plays a marginal role on the buckling load.

The influence of the design variables on the nonlinear buckling load is illustrated in Figure 5.11 by plotting the buckling load as a separate function of each design variable for fixed values of the other variables around the reference design ($t = 1.91$ mm, $\rho = 400$ mm and $\alpha = 17.5°$). As can be observed in Figure 5.11a, the nonlinear buckling load varies

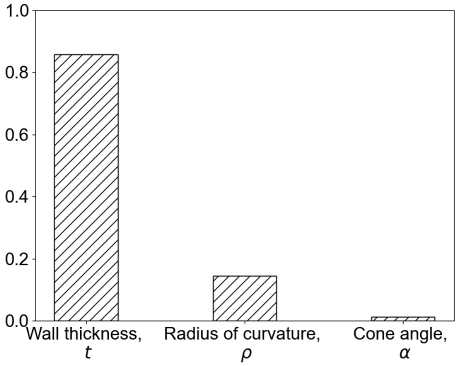

Figure 5.10: Total sensitivity index of the input variables on the nonlinear buckling load of an isotropic conical-cylindrical shell.

from 270 kN for t = 1.27 mm to 1100 kN for t = 2.54 mm, confirming that the thickness plays the most significant role. The radius of curvature, which had minimal effect on the linear buckling load (see Figure 5.7b), is more influential on the buckling load from the geometrically nonlinear analysis (see Figure 5.11b), as it increases from about 390 kN to about 720 kN. The nonlinear buckling load slightly decreases with an increase in the cone angle (decrease of ∽100 kN, see Figure 5.11c), but the effect is small compared to the radius of curvature and wall thickness.

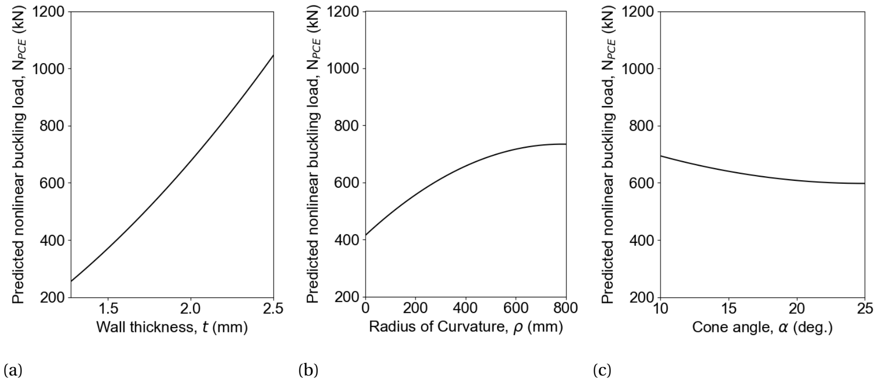

(a) (b) (c)

Figure 5.11: Predicted nonlinear buckling load as a function of each design variable around the reference design ($t = 1.91$ mm, $\rho = 400$ mm, $\alpha = 17.5°$) for (a) variable wall thickness, (b) variable radius of curvature and (c) variable cone angle.

It is interesting to compare the predictions from the expansions $L_{PCE}^{iso,1}$ and N_{PCE}^{iso} as given in equation 5.3 and equation 5.6 and fitted to, respectively, the linear and nonlinear buckling loads. Both expansions use the same number of data points for calibration. Upon numerical integration over the design space indicated in Table 5.1, the average nonlinear buckling load is approximately 30% less than the linear buckling load (about 900 kN for the linear buckling and about 650 kN for the nonlinear buckling averaged over the design space). However, the largest discrepancy between the linear and nonlinear buckling loads occurs for small values of the radius of curvature in the conical-to-cylindrical transition region. This indicates that in general the nonlinear analysis is important for the determination of the buckling load and is particularly critical when the conical-to-cylindrical transition is abrupt (i.e., close to $\rho = 0$ mm).

5.5. LINEAR AND NONLINEAR BUCKLING OF A COMPOSITE CONICAL-CYLINDRICAL SHELL

The geometry considered for the composite conical-cylindrical shells is similar to what was used in the isotropic analyses, Figure 5.1. The cylindrical radius is 400 mm and the overall height of the shell is 1200 mm. In the case of an isotropic shell, as shown in Sections 5.3 and 5.4, the cone angle had minimal influence for both the linear and nonlinear buckling loads; therefore, the cone angle for the study of composite conical cylindrical shells was fixed at 15°. This choice reduces the number of analyses required and, therefore, the overall computational cost. The thickness of the shell and the radius of curvature for the conical-to-cylindrical transition region are taken from the same design range as indicated in Table 5.1.

In this section, various composite layups are considered to study the influence of the composite material properties on the buckling load. For simplicity, only one ply-orientation family is considered (namely the $[-60,60,0]_s$ stacking sequence), but with variable volume fraction v_o of the 0° ply. In a manner similar to the other design variables (i.e., thickness and radius of curvature), the volume fraction is treated as a uniformly distributed random input variable. The design interval for the volume fraction v_o ranges from a minimum of 0.1 to a maximum of 0.9 of the total volume (i.e., 10% to 90% of the thickness). The remaining fraction (1-v_o) is evenly distributed among the -60° and +60° plies. Using this approach, the layups are parametrized with only one variable. The material properties assumed in the study are based on IM7/8551-1 with modulus of elasticity of 140.9 MPa in the fiber direction, a modulus of elasticity transverse to the fiber direction of 9.72 MPa, a shear modulus equal to 4.69 MPa, and an in-plane Poisson's ratio of 0.356.

The same process as used for the isotropic shells was repeated for the composite conical shells, but with input variables of t, ρ, and v_o. Since there are only three variables and a second order equation is considered, only 20 analyses are required to develop the resulting polynomial chaos expansion L_{PCE}^{comp} for the linear buckling load, i.e.,

$$\begin{aligned} L_{PCE}^{comp} &= 49.53t^2 - 116.759v_o t + 0.20\rho t - 543.855v_o^2 + 0.122\rho v_o \\ &\quad +1.93 \cdot 10^{-4}\rho^2 + 243.414t + 840.703v_o - 0.594\rho - 309.099 \end{aligned} \tag{5.8}$$

as well as the expansion N_{PCE}^{comp} for the nonlinear buckling load, i.e.,

$$\begin{aligned} N_{PCE}^{comp} &= 104.88t^2 - 217.657v_o t + 0.248\rho t - 328.430v_o^2 + 0.171\rho v_o \\ &\quad -1.50 \cdot 10^{-4}\rho^2 - 18.648t + 677.627v_o - 0.241\rho - 108.344 \end{aligned} \tag{5.9}$$

Visualizations for the goodness of fit for L^{comp}_{PCE} and N^{comp}_{PCE} for composite conical shells are presented in Figure 5.12a. The coefficients of determination R^2 are 0.993 and 0.991 for the linear and nonlinear buckling load representations, respectively. While still close to unity, the R^2 value are less than the R^2 values for the corresponding representations for the isotropic shells (0.9995 and 0.9992, respectively). The average error for the validation data for the composite shells was 12% for both the linear and nonlinear buckling loads. The maximum error was around 36% for the linear buckling load and 31% for the nonlinear buckling load. These values are larger than what was observed for the isotropic shells. The point with the largest error had input variables of 125 mm, 1.451 mm, with υ_o being at the edge of the design space at 0.9 (90% volume fraction of 0° plies). This is consistent with what was observed for the isotropic shells in that the models with the largest errors have input variables near the limits of the design space. The residual plots show a random pattern, which indicates that the PCE fits the data well. Nonetheless, the residuals are generally higher than the ones observed for the isotropic case (see Figure 5.3b for the linear buckling load and Figure 5.9b for the nonlinear buckling load).

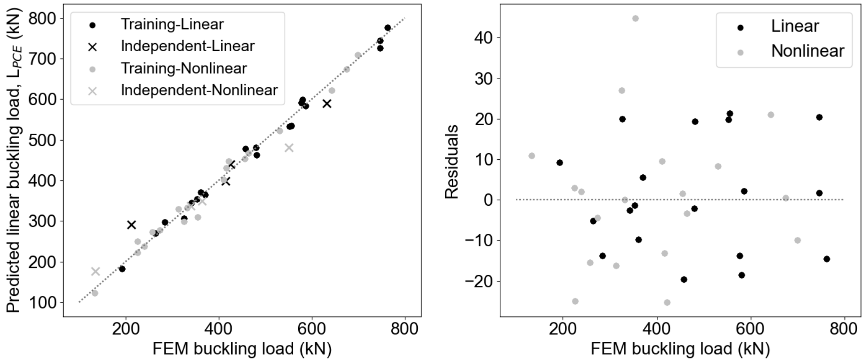

(a)

(b)

Figure 5.12: Goodness of fit metrics for composite conical-cylindrical shells: a) the estimated loads versus the FEM loads for the linear (L) and nonlinear buckling loads (N); b) plot of the residuals.

The difference between the quality of the fit for the isotropic and composite cases can be ascribed to the nature of the design variables used (i.e., t, ρ, and α for the isotropic case and t, ρ, and v_o for the composite case). The cone angle α used in the isotropic case has no significant influence on the buckling load. In contrast, the 0° ply-volume fraction, v_o, used in the composite case has a measurable influence on the buckling load, albeit small compared to the wall thickness, t. Consequently, the calibration data generated for the composite case has more variability than the data generated for the isotropic case. Correspondingly, since both PCE representations use the same number of data points for calibration and the same number of terms in the expansion, it is expected that the quality of the fit will be lower for the data set with higher variability.

Despite not being as accurate as for the isotropic case, the PCE representation of the buckling load for the composite case is reasonably accurate for variables not near the defined bounds and, more importantly, provides valuable information in terms of its sensitivity. The sensitivity indices are presented in Figure 5.13, where it can be observed that the shell thickness is the most relevant parameter to determine both the linear and the nonlinear buckling loads. As a secondary factor, v_o shows some influence on the linear buckling load, whereas the radius of curvature plays an even smaller role. However, this order is reversed for the nonlinear buckling load, for which the radius of curvature becomes more influential than v_o. Nonetheless, for both the linear and nonlinear buckling loads, the fact that the layup has a relatively small contribution to the buckling performance of a conical-cylindrical shell indicates that the buckling load is primarily driven by geometrical features (primarily the shell thickness).

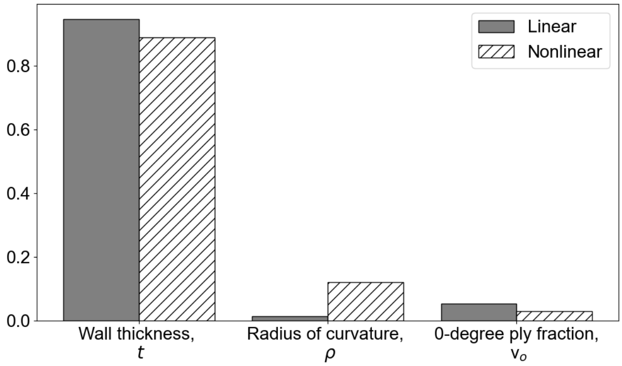

Figure 5.13: Total sensitivity index of the input variables on the linear eigenvalue and nonlinear buckling load for a composite conical-cylindrical shell.

To visualize the effect of the design variables on the linear and nonlinear buckling loads, the plots of their respective PCE representations (i.e., L_{PCE}^{comp} and N_{PCE}^{comp} respectively) are shown in Figure 5.14 as functions of the individual design variables around a reference design, namely a wall thickness of $t = 1.91$ mm, radius of curvature in the transition region of $\rho = 400$ mm and a 0°-ply volume fraction $v_o = 0.5$. As previously mentioned, the cone angle was fixed at $\alpha = 15°$. In Figure 5.14a, which shows the buckling load as a function of the wall thickness, it can be observed that, as in the isotropic case, the wall thickness is the most relevant parameter for determining the buckling load. Nonetheless, as shown in Figure 5.14b, the radius of curvature of the conical-to-cylindrical transition region also plays a relevant role, particularly for the nonlinear buckling load. Similar to the isotropic case, in the composite case, the largest difference between the linear and nonlinear buckling loads occurs for sharper transitions (i.e., lower values of ρ), in which the buckling load is also the smallest. It is also observed that the curve for the linear buckling load is relatively flat as a function of the radius of curvature, which is reflected on its low sensitivity index. The curves of the buckling loads as a function of the volume fraction of 0° plies, as shown in Figure 5.14c, are non-monotonic, but generally this reflects a tendency to remain constant, as confirmed with the low sensitivity indices for both the linear and nonlinear buckling loads shown in Figure 5.13. Furthermore, this result also confirms that geometrical features are generally more important in controlling the buckling load compared to material properties.

As with the isotropic shells, the nonlinear buckling load was generally less than the linear buckling load. On average, the nonlinear buckling load was approximately 20% less than the linear buckling load (approximately 380 kN for the nonlinear buckling load and 470 kN for the linear buckling load, as averaged over the entire design space). This is less than the 30% difference in averages calculated for the isotropic shells, but it still highlights the relevance of performing a nonlinear analysis for the determination of the buckling load. The total sensitivity index for the isotropic shells for thickness from the linear and nonlinear buckling load are 0.98 (Figure 5.6) and 0.86 (Figure 5.10), respectively. The total sensitivity index values for the composite shell are 0.95 and 0.89 for the linear and nonlinear buckling loads (Figure 5.13).

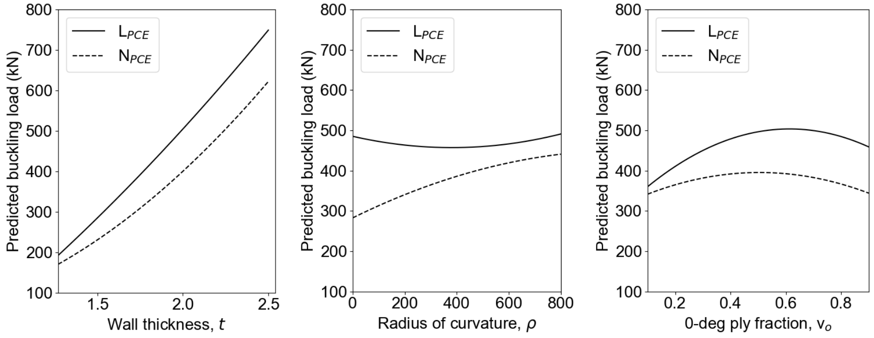

(a) (b) (c)

Figure 5.14: Predicted buckling loads as a function of each design variable around the reference design (t = 1.91 mm, ρ = 400 mm, v_o = 0.5) for (a) variable wall thickness, (b) variable radius of curvature and (c) variable 0° ply fraction.

5.6. CONCLUSION

Polynomial chaos expansion representations were developed to estimate the linear and nonlinear buckling loads of conical-cylindrical shells with isotropic and composite materials. The sensitivities with respect to those buckling loads due to wall thickness, radius of curvature, cone, and 0° ply fraction were investigated. Overall, the PCE representations were able to accurately predict the linear and nonlinear buckling loads. The largest percentage errors between the FEM results and the values from the PCE representation occurred near the bounds of the design space. Additionally, it was observed that the difference between the linear and nonlinear buckling loads is most critical due to geometrical factors, specifically for sharp transitions between the conical and cylindrical regions. The cone angle was found to have no significant effect on the buckling load. The buckling load also remained relatively insensitive to changes in composite layups.

Developing a simple functional expression to predict a given output is one benefit of using PCE. The polynomial expressions obtained in this study could be used to accurately estimate the linear and nonlinear buckling loads of isotropic and composite conical-cylindrical shells within the chosen design range, which is very beneficial during preliminary design studies. For example, if there is a change in the one of the variables within the predetermined design space, then the linear eigenvalue could be estimated without having to create a new finite element model. Depending on which variable changed, it may be concluded that a new assessment is not necessary based on a sensitivity analysis.

The framework used in the present work can be used as a template for further studies that can also quantify the effect of imperfections, and thus provide greater insights on knock-down factors for conical-cylindrical shells.

6

CONCLUSIONS

6.1. CONCLUSIONS

Traditionally, launch vehicles are constructed with a series of buckling-prone thin-walled cylindrical and conical shells, in which the buckling behavior of these shells has been well studied and buckling design guidance exists. Conical-cylindrical shell geometry is now being utilized for launch-vehicle stage adapters and payload adapters due to advances in manufacturing and numerical techniques, but there is no available buckling design guidance for this nontraditional combined geometry. In order to provide design recommendations, a validated modeling methodology is required, and the buckling behavior and imperfection sensitivity of conical-cylindrical shells and how it differs from the conical and cylindrical components needs to be better understood. To this end, a validated modeling methodology for a composite cylindrical shell was presented and its applicability to composite conical-cylindrical shells was shown. Additionally, the numerical investigations on the buckling behavior of conical-cylindrical shells highlight variables that influence the buckling response. Subsequently, the numerical methodology was confirmed through tests. From this, buckling design considerations can be put forward.

- In *Chapter 2*, a modeling methodology is developed, which successfully predicts the buckling behavior of a scaled launch-vehicle-like composite cylindrical shell, referred to as NDL-1. The design of NDL-1 was based on a scaling methodology that resulted in the non-traditional layup $[(23/0/\text{-}23)]_{4s}$ with a nominal diameter of 800 mm and height of 1200 mm. Prior to testing, the test article was scanned to measure the radial geometric imperfections and thickness variations, which could then be incorporated into the finite element model.

  A finite element study was completed prior to the test to assess any potential differences between the four-node reduced-integration shell element (S4R) and the eight-node reduced-integration continuum shell element (SC8R). The S4R element is commonly used to model the buckling behavior of shell structures, but the SC8R element was preferred because it facilitated the incorporation of thickness variations into the model using an in-house script. A mesh convergence study was also completed, and determined that while an element size of approximately 10 mm would be sufficient, a 5 mm mesh size was selected to model the thickness variations more accurately. A geometrically-nonlinear analysis was then performed to predict the buckling response.

The measured buckling load and stiffness were within 1% of the predicted buckling load. Additionally, the observed prebuckling, incipient buckling, and postbuckling behavior of NDL-1 correlated well with the pretest predictions. The predicted buckling load was within 0.04% of the measured load, and the predicted radial displacement shapes matched well with the measured data. The test data was analyzed after the test and findings, such as loading nonuniformity, were discovered. The loading imperfection was incorporated as input into a numerical analysis to highlight the sensitivity of the buckling location. Overall, the modeling methodology presented was successful in predicting the buckling behavior of a composite cylindrical shell with a nontraditional layup, and is therefore recommended for use with other large-scale composite shell structures, including those with complex geometries.

- *Chapter 3* highlighted the differences in buckling behavior between conical shell, cylindrical shell, and conical-cylindrical shell with a numerical study that was validated through experimental testing. It showed that the transition region has a significant influence on the resulting buckling behavior. It also highlighted the fact that the differences between an eigenvalue analysis (i.e., obtaining the buckling load as the lowest eigenvalue of the buckling equation) and obtaining a buckling load as a peak response load in a geometrically nonlinear analysis, could be significant. The geometrically nonlinear analysis could be as low as 50% of the buckling load predicted from an eigenvalue analysis, even for an ideal geometry without imperfections. It was also demonstrated that, depending on the design of the transition region, a conical-cylindrical shell may be less imperfection-sensitive than the individual components. The assumption that the knockdown factor is primarily attributed to radial imperfections, which is the case for conical and cylindrical shells, may not be true for conical-cylindrical shells. The knockdown factors presented in NASA-SP 8007 and NASA-SP-8109 may also not be conservative, which is what is largely assumed for conical and cylindrical shells. It was necessary to confirm the observations made by the numerical analyses experimentally, which led to the design, fabrication and testing of a composite conical-cylindrical shell with a toroidal transition, referred to as 3CHELL.

  Test article 3CHELL was also fabricated and tested to verify that the modeling methodology used to predict the buckling behavior of a composite cylindrical shell with a nontraditional layup can be also used to predict the buckling behavior of a composite conical-cylindrical shell. Test article 3CHELL nominally had a quasi-isotropic layup of $[45/\text{-}45/90/0]_S$. The overall height was 762 mm with a nominal cylindrical-end diameter of 639 mm. The cylindrical end transitioned to the conical section, which had a cone angle of 15 degrees, with a radius of curvature of 380 mm. A FEM that included radial imperfections and thickness variations was developed, and geometrically nonlinear analyses were conducted to predict the structural response. The four-node-reduced- integration shell element (S4R) was used instead of the SC8R element due to computational constraints. The other analysis parameters used to analyze 3CHELL were similar to those used in the NDL-1 analysis.

The test article buckled at a load 8.8% greater than what was predicted. The model also included a measured lateral displacement that was 20% of the total axial end shortening at buckling, but this did not significantly influence the results. The test article was predicted to buckle in the conical region, but it was confirmed with high-speed cameras that buckling initiated in the cylindrical region. Even with the discrepancy in the location of buckling initiation, the predicted and measured buckling responses had several similarities when radial displacements and patterns at incipient buckling and postbuckling were compared. Similar patterns were identified in the measured and predicted radial deformations and magnitudes. The differences between the observed and predicted behaviors of 3CHELL were most likely due to the assumptions made when incorporating the thickness variations into the model. In addition, the buckling test was repeated since 3CHELL buckled without perceptible inelastic failure, and in the second test 3CHELL buckled within 1% of the first buckling test.

- *Chapter 4* focused on how the transition region can change the buckling response and imperfection sensitivity of a composite conical-cylindrical shell. It was shown numerically that adding reinforcement to the transition region of a conical-cylindrical shell can increase the geometrically nonlinear buckling load since the reinforcement is stiffening the region. The chapter also presented results that showed there is a point of diminishing returns for adding reinforcement. Eventually, the buckling load predicted by the geometrically nonlinear analysis converges to the buckling load obtained from an eigenvalue analysis. More importantly, adding reinforcement may seemingly increase the nonlinear buckling load of the shell, but adding reinforcement also makes the structure more sensitive to imperfections. Mass is a critical design constraint for launch vehicles. It may be more beneficial to design a buckling-critical conical-cylindrical shell without reinforcement since the response will be more predictable as it will be less sensitive to geometrical imperfections, which are typically not known prior to manufacturing. This interesting conclusion from the numerical study was confirmed experimentally.

  By analyzing the test data and performing nondestructive evaluation of 3CHELL, it was confirmed that it had buckled elastically, meaning there was no damage or permanent deformation. It was decided to modify the design of 3CHELL by adding reinforcement to the transition region to confirm the observations made in the numerical studies. The reinforced 3CHELL test article was referred to as Re3CHELL. Prior to building the finite element model for Re3CHELL, new data was obtained to better correlate the 3CHELL model. The new data contained information related to the overlapped area of each ply that contributed to the thickness variations. Notably, the additional plies added to the updated 3CHELL model near the transition region to account for the additional thickness variations only increased the mass of the finite element model by less than 0.1%. The small increase in mass changed the predicted buckling behavior, and more closely matched the observed 3CHELL behavior with the predicted buckling load within 2% of the measured buckling load and predicting the buckling location. This highlights the sensitivity of the buckling behavior of a conical-cylindrical shell, and confirms the hypothesis related to the discrepancy between the test data and the original 3CHELL FEM presented in Chapter 3.

The updated 3CHELL model was then modified to account for the two fabric reinforcement plies added for Re3CHELL. The finite element modeling methodology was the same as the one used for 3CHELL, and experimental results correlated very well with the analysis. The experimentally-measured buckling load of Re3CHELL was within 2.5% of the predicted buckling load. Additionally, the predicted buckling location matched the observed buckling location of Re3CHELL. Buckling occurred in the conical section just above thickness discontinuity that was an artifact of the manufacturing process. This again highlights how the location where buckling initiates depends on manufacturing imperfections in conical-cylindrical shells.

A direct comparison could be made between 3CHELL and Re3CHELL since Re3CHELL was a modified version of 3CHELL, and because both of the finite element models for 3CHELL and Re3CHELL correlated well with the corresponding test data. The comparison confirmed that adding reinforcement does in fact increase the imperfection sensitivity to the point where it may not be beneficial to add reinforcement if the goal is to increase the buckling load. Adding reinforcement to Re3CHELL increased the load/unit weight by only 1.5%.

- The numerical studies and experimental results showcased some sensitivities related to the buckling behavior of a conical-cylindrical shell. *Chapter 5* demonstrates the applicability of using Polynomial Chaos Expansion (PCE) to help quantify the geometric and design features that influence the eigenvalue buckling load as well as the geometrically nonlinear buckling load of an isotropic and composite conical-cylindrical shell. PCE could also be a valuable tool to use for preliminary launch vehicle design of a conical-cylindrical shell. Important parameters in PCE, such as the order equation and oversampling ratio, were assessed to conclude a quadratic equation with an oversampling ratio of 2 was sufficient to develop an accurate polynomial expression that predicted the buckling load for the given set of input variables. The variables considered included thickness, cone angle, radius of curvature, and the ratio of the number of 0-degree plies to the total number of plies in a composite laminate. The thickness dominates the eigenvalue buckling load as well as the nonlinear buckling load. The cone angle had more influence to the eigenvalue buckling load than the nonlinear buckling load, but it was minimal compared to the thickness for the range of cone angles analyzed, namely between 10 and 25 degrees. For composite shells, the cone angle was not considered as an input variable in the corresponding PCE approximation since it was found to have a minimal influence in the isotropic case. In summary, the results generated from PCE assessment using the composite material cases suggests that the buckling behavior is more related to the geometric features such as the radius of curvature of the transition region than the ratio of 0-degree plies. The ratio of 0-degree plies compared to the total number of plies only had a small effect on the resultant buckling loads as compared to the radius of curvature and thickness. PCE is a versatile tool that can aid in the design of launch vehicle structures.

6.2. DESIGN RECOMMENDATIONS

The methodologies and findings of this thesis form the foundation of a framework for designing a conical-cylindrical shells to be used as a payload adapter or a launch vehicle stage adapter that is susceptible to buckling. The traditional approach of multiplying the eigenvalue buckling load by a recommend knockdown factor is not appropriate for conical-cylindrical shells, but fortunately it is possible to leverage the modeling approaches used to predict the buckling behavior for the individual components. These recommendations can be separated into two different: design and analysis.

Design

- Even though it may be computationally intensive, a geometrically nonlinear analysis is recommended to characterize the buckling behavior of a conical-cylindrical shell even in the early design phase.

- It is recommended to not reinforce the transition region if buckling is the only consideration. It may be possible to capitalize on the fact that the geometrical nonlinearity can be accurately modeled, and radial imperfections that are unknown may not significantly influence the buckling response.

- If reinforcement needs to be added, the trade-off between imperfection sensitivity and geometric nonlinearity should be well understood by completing an imperfection sensitivity study. It is recommended to use a variety of imperfection shapes that affect the conical and cylindrical regions.

Analysis

- The current finite element tools have the ability to predict the buckling response of a composite conical cylindrical shell using shell elements and including geometric and thickness variations.

- The thickness variations can influence the buckling response, specifically the buckling location, so it is recommended to incorporate as-built details for a numerical re-assessment of the buckling behavior.

- Validated finite elements may be used to develop design specific knockdown factors for conical-cylindrical shells.

6.3. FUTURE WORK

While comprehensive research related to the buckling of conical-cylindrical shells has been completed, there are aspects of the work that should be expanded upon for future work. First, it is of interest to study the buckling behavior of conical cylindrical shells with cone angles greater than 25 degrees. The current research demonstrated that cone angles less than 25 degrees do not significantly influence the buckling behavior, but there may be a limit in which the angle begins to dictate the buckling response, plus this angle range would encompass more payload adapter geometries. Additionally, the transition region was identified as a critical design feature in the buckling of conical-cylindrical shells. It would be interesting to determine how to optimize the design of the transition region, specifically using composite materials. Next, the successful demonstration of the PCE methodology to identify the important design variables that significantly contribute to the buckling of conical-cylindrical helped highlight the potential to use PCE for future studies related to buckling. For example, it would be interesting to use PCE to investigate imperfection sensitivity of conical-cylindrical shells. Finally, more test data is required to enhance the level of confidence of the conclusions reached in the present thesis. Expanding the design space to test different cone angles and radius of curvatures would be extremely valuable. There are many avenues to expand upon the research presented.

BIBLIOGRAPHY

[1] *NASA's Space Launch System Reference Guide 2022*. National Aeronautics and Space Administration. 2022.

[2] *Universal Stage Adapter*. National Aeronautics and Space Administration. 2022.

[3] *Deploying Multiple Satelites with Syla and Vespa*. European Space Agency. 2022.

[4] NASA. *SLS Rocket's Universal Stage Adapter Ready for Testing*. https://www.youtube.com/watch?v=ZjTS3yQumuo. Accessed: 2024-12-16. 2024.

[5] Hilburger M.W. "Buckling of Cylindrical Shells". In: *NASA SP-8007 Rev 2*. 2020.

[6] Wagner H.N.R., Hühne C., and Janssen M. "Buckling of cylindrical shells under axial compression with loading imperfections: An experimental and numerical campaign on low knockdown factors". In: *Thin-Walled Structures* 151 (2020), p. 106764. DOI: 10.1016/j.tws.2020.106764.

[7] Koiter W.T. *On the stability of elastic equilibrium*. National Aeronautics and Space Administration, 1967.

[8] Bert C.W., Crisman W.C., and Nordby G.M. "Buckling of cylindrical and conical sandwich shells with orthotropicfacings." In: *AIAA Journal* 7.2 (1969), pp. 250–257. DOI: 10.2514/3.55519.

[9] Card M.F. *The sensitivity of buckling of axially compressed fiber-reinforced cylindrical shells to small geometric imperfections*. Tech. rep. NASA TMX-61914. 1969.

[10] Tennyson R.C. and Muggeridge D.B. "Buckling of laminated anisotropic imperfect circular cylinders under axial compression". In: *Journal of Spacecraft and Rockets* 10.2 (1973), pp. 143–148. DOI: 10.2514/3.61860.

[11] Herakovich C.T. *Theoretical-experimental correlation for buckling of composite cylinders under combined compression and torsion*. Tech. rep. NASA Contract NAS1-13175. 1978. DOI: 10.2514/3.55519.

[12] Hilburger M.W. and Jr. Starnes J. "High-fidelity nonlinear analysis of compression-loaded composite shells". In: *19th AIAA Applied Aerodynamics Conference*. 2001, p. 1394. DOI: 10.2514/6.2001-1394.

[13] Khakimova R., Castro S.G.P., Wilckens D., Rohwer K., and Degenhardt R. "Buckling of axially compressed CFRP cylinders with and without additional lateral load: Experimental and numerical investigation". In: *Thin-Walled Structures* 119 (2017), pp. 178–189. DOI: 10.1016/j.tws.2017.06.002.

[14] Bisagni C. "Numerical analysis and experimental correlation of composite shell buckling and post-buckling". In: *Composites Part B: Engineering* 31.8 (2000), pp. 655–667. DOI: 10.1016/S1359-8368(00)00031-7.

[15] Priyadarsini R.S., Kalyanaraman V., and Srinivasan S.M. “Numerical and experimental study of buckling of advanced fiber composite cylinders under axial compression”. In: *International Journal of Structural Stability and Dynamics* 12.04 (2012), p. 1250028. DOI: `10.1142/S0219455412500289`.

[16] Ghalghachi R.N., Showkati H., and Firouzsalari S.E. “Buckling behaviour of GFRP cylindrical shells subjected to axial compression load”. In: *Composite Structures* 260 (2021), p. 113269. DOI: `10.1016/j.compstruct.2020.113269`.

[17] Hilburger M.W. “Buckling and failure of compression-loaded composite laminated shells with cutouts”. In: *48th AIAA/ASME/ASCE/AHS/ASC Structures, Structural Dynamics, and Materials Conference*. 2007, p. 2227. DOI: `10.2514/6.2007-2227`.

[18] White S.C., P.M. Weaver, and K.C. Wu. “Post-buckling analyses of variable-stiffness composite cylinders in axial compression”. In: *Composite Structures* 123 (2015), pp. 190–203. DOI: `10.1016/j.compstruct.2014.12.01`.

[19] Taheri-Behrooz F., Omidi M., and Shokrieh M.M. “Experimental and numerical investigation of buckling behavior of composite cylinders with cutout”. In: *Thin-Walled Structures* 116 (2017), pp. 136–144. DOI: `10.1016/j.tws.2017.03.009`.

[20] Labans E. and Bisagni C. “Buckling and free vibration study of variable and constant-stiffness cylindrical shells”. In: *Composite Structures* 210 (2019), pp. 446–457. DOI: `10.1016/j.compstruct.2018.11.061`.

[21] Labans E., Bisagni C., Celebi M., Tatting B., Gürdal Z., Blom-Schieber A., Rassaian M., and Wanthal S. “Bending of composite cylindrical shells with circular cutouts: Experimental validation”. In: *Journal of Aircraft* 56.4 (2019), pp. 1534–1550. DOI: `10.2514/1.C035247`.

[22] Degenhardt R., Kling A., Bethge A., Orf J., Kärger ., Zimmermann R., Rohwer K., and Calvi A. “Investigations on imperfection sensitivity and deduction of improved knock-down factors for unstiffened CFRP cylindrical shells”. In: *Composite Structures* 92.8 (2010), pp. 1939–1946. DOI: `10.1016/j.compstruct.2009.12.014`.

[23] Schillo C., Röstermundt D., and Krause D. “Experimental and numerical study on the influence of imperfections on the buckling load of unstiffened CFRP shells”. In: *Composite Structures* 131 (2015), pp. 128–138. DOI: `10.1016/j.compstruct.2015.04.032`.

[24] Hühne C., Rolfes R., Breitbach E., and Teßmer J. “Robust design of composite cylindrical shells under axial compression—simulation and validation”. In: *Thin-walled structures* 46.7-9 (2008), pp. 947–962. DOI: `10.1016/j.tws.2008.01.043`.

[25] Schultz M.R., Sleight D.W., Myers D.E., Waters Jr W.A., Chunchu P.B., Lovejoy A.W., and Hilburger M.W. “Buckling design and imperfection sensitivity of sandwich composite launch-vehicle shell structures”. In: *In the proceedings of the 31st American Society for Composites Technical Conference*. 2016.

[26] Schultz M.R., Sleight D.W., Gardner N.W., Rudd M.T., Hilburger M.W., Palm T., and Oldfield N.J. “Test and Analysis of a Buckling-Critical Large-Scale Sandwich Composite Cylinder”. In: *2018 AIAA/ASCE/AHS/ASC Structures, Structural Dynamics, and Materials Conference*. DOI: `10.2514/6.2018-1693`.

[27] Przekop A., Schultz M.R., Kosztowny C.J.R., Gardner N.W., Song K., and Rudd M.T. “Buckling test and analysis of the 8-foot-diameter sandwich composite cylinder test article CTA8. 2 as part of the Shell Buckling Knockdown Factor Project: Test dates 5-7 December 2017”. In: (2022).

[28] Song K., Schultz M.R, Kosztowny C.J.R., Przekop A., Gardner N.W., and Rudd M.T. “Buckling Test and Analysis of the 8-foot-diameter Sandwich Composite Cylinder Test Article CTA8. 3 as Part of the Shell Buckling Knockdown Factor Project: Test Dates 16-19 December 2019”. In: (2022).

[29] Uriol Balbin I., Bisagni C., Schultz M.R., and Hilburger M.W. “Scaling methodology applied to buckling of sandwich composite cylindrical shells”. In: *AIAA Journal* 58.8 (2020), pp. 3680–3689. DOI: `10.2514/1.J058999`.

[30] Alexander B.F. and Ng K.C. “3-D shape measurement by active triangulation using an array of coded light stripes”. In: *Optics, Illumination, and Image Sensing for Machine Vision II*. Vol. 850. SPIE. 1988, pp. 199–209. DOI: `10.1117/12.942878`.

[31] Hexcel Corporation. *HexPly® 8552 Epoxy Matrix (180° C/365° F) curing matrix product data sheet*. `https://www.hexcel.com/user_area/content_media/raw/HexPly_8552_eu_DataSheet.pdf`. last accessed May 2020.

[32] E. Clarkson. *Hexcel 8552 IM7 Unidirectional Prepreg 190 gsm & 35%RC Qualification Statistical Analysis Report*. Tech. rep. CAM-RP-2009-028 Rev B. Witchita State University: National Institute for Aviation Research, 2019.

[33] *ABAQUS/Standard User’s Manual, Version 2017*. Dassault Systèmes Simulia Corp. United States, 2017.

[34] Hilburger M.W. and Jr. Starnes J.H. “Effects of Imperfections of the Buckling Response of Composite Shells”. In: *Thin-Walled Structures* 42.3 (2004), pp. 369–397. DOI: `10.1016/j.tws.2003.09.001`.

[35] Takano A., Kitamura R., Masai T., and Bao J. “Buckling Test of Composite Cylindrical Shells with Large Radius Thickness Ratio”. In: *Applied Sciences* 11.2 (2021). DOI: `10.3390/app11020854`.

[36] Rudd M.T., Eberlein D.J., Waters W.A., Gardner N.W., Schultz M.R., and Bisagni C. “Analysis and validation of a scaled, launch-vehicle-like composite cylinder under axial compression”. In: *Composite Structures* 304 (2023), p. 116393. ISSN: 0263-8223. DOI: `10.1016/j.compstruct.2022.116393`.

[37] Hartwich T.S., Panek S., Wilckens D., Bock M., and Krause D. “The influence of the manufacturing process and test boundary conditions on the buckling load of thin-walled cylindrical CFRP shells”. In: *Composite Structures* 308 (2023), p. 116674. ISSN: 0263-8223. DOI: `10.1016/j.compstruct.2023.116674`.

[38] Wagner H.N.R., Hühne C., and Niemann S. “Robust knockdown factors for the design of axially loaded cylindrical and conical composite shells – Development and Validation”. In: *Composite Structures* 173 (2017), pp. 281–303. ISSN: 0263-8223. DOI: `10.1016/j.compstruct.2017.02.031`.

[39] European Commission. *Final Report Summary - DESICOS (New Robust DESIgn Guideline for Imperfection Sensitive Cmposite Launcher Structures)*. Tech. rep. FP&-SPACE-2011-282522. 2011.

[40] L. Tong. “Buckling of Filament-Wound Laminated Conical Shells Under Axial Compression”. In: *AIAA Journal* 37.6 (1999), pp. 778–781. DOI: `10.2514/2.792`.

[41] Y. Goldfeld and J. Arbocz. “Buckling of Laminated Conical Shells Given the Variations of the Stiffness Coefficients”. In: *AIAA Journal* 42.3 (2004), pp. 642–649. DOI: `10.2514/1.2765`.

[42] Khakimova R., Wilckens D., Reichardt J., Zimmermann R., and Degenhardt R. “Buckling of axially compressed CFRP truncated cones: Experimental and numerical investigation”. In: *Composite Structures* 146 (2016), pp. 232–247. DOI: `10.1016/j.compstruct.2016.02.023`.

[43] Khakimova R., Zimmermann R., Wilckens D., Rohwer K., and Degenhardt R. “Buckling of axially compressed CFRP truncated cones with additional lateral load: Experimental and numerical investigation”. In: *Composite Structures* 157 (2016), pp. 436–447. DOI: `10.1016/j.compstruct.2016.08.011`.

[44] H. Abramovich, K. Kalnins, and A. Wieder. “13 - Test results on the stability and vibrations of composite shells”. In: *Stability and Vibrations of Thin Walled Composite Structures*. Ed. by Haim A. Woodhead Publishing, 2017, pp. 619–691. ISBN: 978-0-08-100410-4. DOI: `10.1016/B978-0-08-100410-4.00013-2`.

[45] Sleight D.W., Satyanarayana A., Li Y., and Schultz M.R. “Buckling Imperfection Sensitivity of Conical Sandwich Composite Structures for Launch-Vehicles”. In: *2018 AIAA/ASCE/AHS/ASC Structures, Structural Dynamics, and Materials Conference*. DOI: `10.2514/6.2018-1696`.

[46] Wunderlich W., Obrecht H., Springer H., and Lu Z. “A semi-analytical approach to the nonlinear analysis of shells of revolution”. In: *Analytical and computational models for shells* 3 (1989), pp. 509–536. DOI: `10.1016/S0308-0161(98)00013-1`.

[47] Anwen W. “Stresses and stability for the cone-cylinder shells with toroidal transition”. In: *International Journal of Pressure Vessels and Piping* 75.1 (1998), pp. 49–56. ISSN: 0308-0161. DOI: `10.1016/S0308-0161(98)00013-1`.

[48] Patel B.P., Nath Y., and Shukla K.K. “Nonlinear thermo-elastic buckling characteristics of cross-ply laminated joined conical–cylindrical shells”. In: *International Journal of Solids and Structures* 43.16 (2006), pp. 4810–4829. DOI: `10.1016/j.ijsolstr.2005.07.025`.

[49] Singh S., Patel B.P., and Nath Y. “Postbuckling Behavior of Angle-Ply Laminated Joined Circular Conical-Cylindrical Shells”. In: *AIAA Journal* 45.4 (2007), pp. 942–949. DOI: `10.2514/1.28358`.

[50] Zarei M. and Rahimi G.H. “Buckling Resistance of Joined Composite Sandwich Conical-Cylindrical Shells with Lattice Core Under Lateral Pressure”. In: *Thin-Walled Structures* 174 (2022), p. 109027. DOI: `10.1016/j.tws.2022.109027`.

[51] Hu W.C. and Raney J.P. “Experimental and analytical study of vibrations of joined shells.” In: *Aiaa Journal* 5.5 (1967), pp. 976–980. DOI: `10.2514/3.4111`.

[52] Bushnell D. and Galletly G.D. “Comparisons of test and theory for nonsymmetric elastic-plastic buckling of shells of revolution”. In: *International Journal of Solids and Structures* 10.11 (1974), pp. 1271–1286. ISSN: 0020-7683. DOI: `10.1016/0020-7683(74)90072-9`.

[53] Zhao Y. “Buckling behaviour of imperfect ring-stiffened cone–cylinder intersections under internal pressure”. In: *International Journal of Pressure Vessels and Piping* 82.7 (2005), pp. 553–564. ISSN: 0308-0161. DOI: `10.1016/j.ijpvp.2005.01.008`.

[54] Chronopoulos D., Ichchou M., Troclet B., and Bareille O. “Predicting the broadband response of a layered cone-cylinder-cone shell”. In: *Composite Structures* 107 (2014), pp. 149–159. ISSN: 0263-8223. DOI: `10.1016/j.compstruct.2013.07.055`.

[55] Marguerre K. *Stability of the Cylindrical Shell of Variable Curvature*. Tech. rep. NACA TM-1302. 1951.

[56] Baker E.H., Cappelli A.P., Kovalevsky L., Rish F.L., and Verette R.M. *Shell Analysis Manual*. Tech. rep. NACA CR - 192. 1968.

[57] Almroth B.O., Bushnell D., and Sobel L.H. *Buckling of Shells of Revolution with Various Wall Constructions: Volume 1- Numerical Results*. Tech. rep. NACA CR - 1049. 1968.

[58] Bushnell D., Almroth B.O., and Sobel L.H. *Buckling of Shells of Revolution with Various Wall Constructions: Volume 2- Basic Equations and Method of Solution*. Tech. rep. NACA CR - 1050. 1968.

[59] Tornabene F. and Viola E. “Static Analysis of Functionally Graded Doubly-Curved Shells and Panels of Revolution”. In: *Meccanica* 48 (May 2013), pp. 901–930. DOI: `10.1007/s11012-012-9643-1`.

[60] Tornabene F., Fantuzzi N., and Bacciocchi M. “Free vibrations of free-form doubly-curved shells made of functionally graded materials using higher-order equivalent single layer theories”. In: *Composites Part B: Engineering* 67 (2014), pp. 490–509. ISSN: 1359-8368. DOI: `10.1016/j.compositesb.2014.08.012`.

[61] Zingoni A. and Enoma N. “Strength and stability of spherical-conical shell assemblies under external hydrostatic pressure”. In: *Thin-Walled Structures* 146 (2020), p. 106472. ISSN: 0263-8231. DOI: `10.1016/j.tws.2019.106472`.

[62] *ABAQUS/Standard User’s Manual, Version 2021*. Dassault Systèmes Simulia Corp. United States, 2021.

[63] *Metallic Materials Properties Development and Standardization (MMPDS)*. Tech. rep. 2015.

[64] *Micor Micorox® Standard Grout Data Sheet*. `https://www.micorco.com/wp-content/uploads/2014/03/Micorox-Standard-Grout-PDF-3-2014.pdf`. last accessed November 2022.

[65] Bomarito G.F., Hochhalter J.D., Ruggles T.J., and Cannon A.H. “Increasing accuracy and precision of digital image correlation through pattern optimization”. In: *Optics and Lasers in Engineering* 91 (2017), pp. 73–85. DOI: 10.1016/j.optlaseng.2016.11.005.

[66] Bomarito G.F., Hochhalter J.D., and Ruggles T.J. “Development of optimal multiscale patterns for digital image correlation via local grayscale variation”. In: *Experimental Mechanics* 58 (2018), pp. 1169–1180. DOI: 10.1117/12.942878.

[67] Song K., Schultz M.R., Kosztowny C.J.R., Gardner N.W., and Rudd M.T. *Buckling Test and Analysis of the 8-Foot-Diameter Sandwich Composite Cylinder Test Article CTA8.3 as part of the Shell Buckling Knockdown Factor Project: Test dates 16-19 December 2019*. Tech. rep. NASA-TM-20210024768. 2021.

[68] Blom A.W., Tatting B.F., Hol J.M.A.M., and Gürdal Z. “Fiber path definitions for elastically tailored conical shells”. In: *Composites part B: engineering* 40.1 (2009), pp. 77–84. DOI: 10.1016/j.compositesb.2008.03.011.

[69] Kosztowny C.J.R. “Implementing Geometric Surface Imperfections into Sandwich Composite Cylinder Finite Element Method Models”. In: *AIAA Scitech 2021 Forum*. 2021, p. 0439. DOI: 10.2514/6.2021-0439.

[70] Bisagni C. and Cordisco P. “Post-buckling and collapse experiments of stiffened composite cylindrical shells subjected to axial loading and torque”. In: *Composite structures* 73.2 (2006), pp. 138–149. DOI: 10.1016/j.compstruct.2005.11.055.

[71] Ning X. and Pellegrino S. “Imperfection-insensitive axially loaded cylindrical shells”. In: *Proceedings of the 54th AIAA/ASME/ASCE/AHS/ASC Structures, Structural Dynamics and Materials Conference, Boston, MA, US*. 2013, pp. 8–11. DOI: 10.1016/j.ijsolstr.2014.12.030.

[72] Ning X. and Pellegrino S. “Experiments on imperfection insensitive axially loaded cylindrical shells”. In: *International Journal of Solids and Structures* 115 (2017), pp. 73–86. DOI: 10.1016/j.ijsolstr.2017.02.028.

[73] Lincoln R.L., Weaver P.M., Pirrera A., and Groh R.M.J. “Imperfection-insensitive continuous tow-sheared cylinders”. In: *Composite Structures* 260 (2021), p. 113445. DOI: 10.1016/j.compstruct.2020.113445.

[74] Wagner H.N.R., Köke H., Dähne S., Niemann S., Hühne C., and Khakimova R. “Decision tree-based machine learning to optimize the laminate stacking of composite cylinders for maximum buckling load and minimum imperfection sensitivity”. In: *Composite Structures* 220 (2019), pp. 45–63. DOI: 10.1016/j.compstruct.2019.02.103.

[75] Rudd M.T., Schultz M.R., and Bisagni C. “Buckling Behavior of Conical-Cylindrical Shells and Design Considerations for Launch-Vehicle Applications”. In: *AIAA Scitech 2024 Forum*. 2024, p. 0034. DOI: 10.2514/6.2024-0034.

[76] Noevere A.T. and Collier C.S. “Mapping AFP manufacturing data from VCP to hypersizer for stress analysis and optimization”. In: *In AIAA/ASCE/AHS/ASC structures, structural dynamics, and materials conference*. 2018. DOI: 10.2514/6.2018-022.

[77] Noevere A., Collier C., Harik R., and Halbritter J. "Development of a design for manufacturing tool for automated fiber placement structures". In: *AIAA Scitech 2019 Forum*. 2019, p. 0520. DOI: 10.2514/6.2019-0520.

[78] Rudd M.T., Schultz M.R., Gardner N.W., Kosztowny C.J.R., and Bisagni C. "Analysis and Testing of a Launch-Vehicle-Like Composite Conical-Cylindrical Shell". In: *AIAA Journal* 62.9 (2024), pp. 3526–3543. DOI: 10.2514/1.J063617.

[79] *Toray 3960 Prepreg System Data Sheet*. https://www.toraycma.com/wp-content/uploads/3960-Prepreg-System.pdf. last accessed October 2023.

[80] *Technical Data Sheet FM 209-1 Film Adhesive*.

[81] Clarkson E. *Hexcel 8552S AS4 Plain Weave Fabric Qualification Statistical Analysis Report*. Tech. rep. NCP-RP-2010-011 Rev B. Witchita State University: National Institute for Aviation Research, 2018.

[82] Clarkson E. *Cytec Cycom 5320-1 T650 3k-PW Fabric Material Allowable Statistical Analysis Report*. Tech. rep. NCP-RP-2012-023 NC. Witchita State University: National Institute for Aviation Research, 2015.

[83] Clarkson E. *Solvay (Formerly ACG) MTM45-1/CF0525-36%RW 3K PW AS4 Fabric Qualification Statistical Analysis Report*. Tech. rep. NCP-RP-2009-037 NC. Witchita State University: National Institute for Aviation Research, 2019.

[84] *Vericut Composite Programming Software Package, Ver. 9.3*. CGTech. United States, 2023.

[85] Elishakoff I. and Arbocz J. "Reliability of axially compressed cylindrical shells with random axisymmetric imperfections". In: *International Journal of Solids and Structures* 18.7 (1982), pp. 563–585. DOI: https://doi.org/10.1016/j.engstruct.2011.05.009.

[86] Isaac Elishakoff and Johann Arbocz. "Reliability of axially compressed cylindrical shells with general nonsymmetric imperfections". In: *ASME Journal Applied Mechanics* (1985). DOI: https://doi.org/10.1115/1.3168980.

[87] Stefanou G. "Response variability of cylindrical shells with stochastic non-Gaussian material and geometric properties". In: *Engineering structures* 33.9 (2011), pp. 2621–2627. DOI: https://doi.org/10.1016/j.engstruct.2011.05.009.

[88] Broggi M.S.G.I. and Schuëller G.I. "Efficient modeling of imperfections for buckling analysis of composite cylindrical shells". In: *Engineering Structures* 33.5 (2011), pp. 1796–1806. DOI: https://doi.org/10.1016/j.engstruct.2011.02.019.

[89] Kepple J., Herath M., Pearce G., Prusty G., Thomson R., and Degenhardt R. "Improved stochastic methods for modelling imperfections for buckling analysis of composite cylindrical shells". In: *Engineering Structures* 100 (2015), pp. 385–398. DOI: 10.1016/j.engstruct.2015.06.013.

[90] Sadovskỳ Z., Kriváček J., and Sokol M. "A probabilistic identification of the buckling resistance of imperfect cylindrical shells in axial compression". In: *Engineering Structures* 307 (2024), p. 117934. DOI: 10.1016/j.engstruct.2024.117934.

[91] Arbocz J. and Hilburger M.W. “Toward a probabilistic preliminary design criterion for buckling critical composite shells”. In: *AIAA journal* 43.8 (2005), pp. 1823–1827. DOI: 10.2514/1.11368.

[92] Alfano M. and Bisagni C. “Probabilistic buckling analysis of composite and sandwich cylindrical shells”. In: *55th AIAA/ASMe/ASCE/AHS/SC Structures, Structural Dynamics, and Materials Conference*. 2014, p. 0166. DOI: 10.2514/6.2014-0166.

[93] Alfano M. and Bisagni C. “Probability-based methodology for buckling investigation of sandwich composite shells with and without cut-outs”. In: *International Journal for Computational Methods in Engineering Science and Mechanics* 18.1 (2017), pp. 77–90. DOI: 10.1080/15502287.2016.1276353.

[94] Schillo C., Kriegesmann B., and Krause D. “Reliability based calibration of safety factors for unstiffened cylindrical composite shells”. In: *Composite structures* 168 (2017), pp. 798–812. DOI: 10.1016/j.compstruct.2017.02.082.

[95] Yang S., Xiong F., and Wang F. “Polynomial chaos expansion for probabilistic uncertainty propagation”. In: *Uncertainty Quantification and Model Calibration* 13 (2017). DOI: 10.5772/intechopen.68484.

[96] Kumthekar A., Ponnusami S.A., van der Zwaag S., and Turteltaub S. “Uncertainty quantification of the lifetime of self-healing thermal barrier coatings based on surrogate modelling of thermal cyclic fracture and healing”. In: *Materials & Design* 221 (2022), p. 110973. DOI: 10.1016/j.matdes.2022.110973.

[97] Hamdia K.M., Silani M., Zhuang X., He P., and Rabczuk T. “Stochastic analysis of the fracture toughness of polymeric nanoparticle composites using polynomial chaos expansions”. In: *International Journal of Fracture* 206 (2017), pp. 215–227. DOI: 10.1007/s10704-017-0210-6.

[98] Xiu D. and Karniadakis G.E. “Modeling uncertainty in flow simulations via generalized polynomial chaos”. In: *Journal of computational physics* 187.1 (2003), pp. 137–167. DOI: 10.1016/S0021-9991(03)00092-5.

[99] Crestaux T., Le Maıtre O., and Martinez J. “Polynomial chaos expansion for sensitivity analysis”. In: *Reliability Engineering & System Safety* 94.7 (2009), pp. 1161–1172. DOI: 10.1016/j.ress.2008.10.008.

[100] Liang Ke., Sun Q., and Liu X. “Investigation on imperfection sensitivity of composite cylindrical shells using the nonlinearity reduction technique and the polynomial chaos method”. In: *Acta Astronautica* 146 (2018), pp. 349–358. DOI: 10.1016/S0021-9991(03)00092-5.

[101] Kumar D., Koutsawa Y., Rauchs G., Marchi M., Kavka C., and Belouettar S. “Efficient uncertainty quantification and management in the early stage design of composite applications”. In: *Composite Structures* 251 (2020), p. 112538. DOI: 10.1016/j.compstruct.2020.112538.

[102] Paudel A., Gupta S., Rowshan N., Thapa M., Mulani S.B., and Walters R.W. “Stochastic Buckling of Composite Cylinder with Geometric Imperfection and Global Sensitivity Analysis”. In: *AIAA SCITECH 2023 Forum*. 2023, p. 1093. DOI: 10.2514/6.2023-1093.

[103] Nguyen T.H. and Chang K. “Comparison of the Point-Collocation Non-Intrusive Polynomial (NIPC) and Non-Intrusive Spectral Projection (NISP) Methods for the γ- R θ Transition Model”. In: *Applied Sciences* 9.7 (2019), p. 1407. DOI: 10.3390/app9071407.

[104] Hosder S., Walters R., and Balch M. “Efficient sampling for non-intrusive polynomial chaos applications with multiple uncertain input variables”. In: *48th AIAA/ ASME/ ASCE/ AHS/ ASC Structures, Structural Dynamics, and Materials Conference*. 2007, p. 1939. DOI: 10.2514/6.2007-1939.

[105] Feinberg J. and Langtangen H.P. “Chaospy: An open source tool for designing methods of uncertainty quantification”. In: *Journal of Computational Science* 11 (2015), pp. 46–57. DOI: 10.1016/j.jocs.2015.08.008.

[106] Rudd M.T., Schultz M.R., and Bisagni C. “Buckling Behavior of Conical-Cylindrical Shells and Design Considerations for Launch-Vehicle Applications”. In: *AIAA Scitech 2024 Forum*. 2024, p. 0034. DOI: 10.2514/6.2024-0034.

ACKNOWLEDGEMENTS

It takes a village to complete a PhD. Pursing a PhD while working full-time and having two children along the way was not possible without the support of advisers, supervisors, coworkers, family, and friends.

I am grateful for my promoters, Chiara and Sergio. Chiara has always given me perspective of how my work fits into the broader body of knowledge. This has enabled me to be a better writer and communicator of my research. She has been a great mentor and role model. Her support and encouragement are an important reason for completing my PhD. I am thankful that she agreed to make me a graduate student. I appreciate Sergio's guidance on my PhD research. There was a time when I was stuck as to how to move forward with my research, and his suggestions helped me complete the story of my research. Even though Chiara and Sergio were an ocean away, I always knew they were available to help whenever I needed it.

I want to acknowledge Marc Schultz for his mentorship. His encouragement to pursue my PhD is a significant reason why I decided to go for it. He was my day-to-day advisor and there was a time that we actually spoke on a daily basis. He gave me great advice and feedback, but also let me vent and complain. Lastly, Virginia crab cakes are the best.

My supervisors and coworkers were immensely helpful during this time. I would not have been able to balance my work-life balance without their understanding and flexibility. They supported all of my research proposals at NASA, and without that support I would have never completed my PhD.

I also need to specifically mention Jeff Norris, to whom this dissertation is dedicated to. He is the reason for my career trajectory. He invited me to work on the Shell Buckling Knockdown Factor, which is where I met Marc and Marc introduced me to Chiara. During the COVID shutdown, Jeff managed to build the mandrel that was used to build the test article 3CHELL. He unfortunately passed away shortly after the mandrel was complete. I am so honored I had the privilege to know and work with him.

My family was my foundation through this whole process. Carl is the best partner, husband, and father. He never once questioned the pursuit of my PhD even when I had to set an alarm for 1:30 am to prepare for an online class at 8:00 am in the Netherlands or when he had to take off 2 weeks of work to go to the Netherlands with our son for my Go-No because I couldn't bear being away from my 10-month-old. I also need to acknowledge my parents. Both have their PhDs and are the ones who instilled my love of science and math from a young age. Growing up I thought everyone had a PhD, and was surprised when I learned that was far from the truth. They could empathize with my stress and frustration, and provide encouraging words when I needed it. I am so thankful they moved to Alabama to be close to Carl and our children.

BIOGRAPHICAL NOTE

Michelle Tillotson RUDD

Michelle Tillotson Rudd was born in Midland, Michigan, United States on April 29, 1988. Her parents, each with a PhD in Environmental Physics, were able to stoke her curiosity and love for math and science. At an early age she enjoyed watching shows such as "Extreme Engineering" on the Discovery Channel, and knew she wanted to become an engineer. She attend Lehigh University where she obtained her BSc in Civil Engineering (2010) and MEng in Structural Engineering (2011). Though she loved research, she wasn't ready for the level of effort required to pursue a PhD, and decided work in industry. During this time she also knew she did not want to work in the civil/structural field, contrary to her degrees, and wanted to migrate toward aerospace engineering. After Lehigh University, she worked for a nuclear power plant for 9 months when she received a message from an old classmate who told her about the position at NASA.

From the beginning of her career at NASA, she vowed to pursue her PhD through NASA if the opportunity presented itself. Thankfully, that opportunity arose in the summer of 2017. During that time she was working as the project manager for the NASA Engineering and Safety Center's Shell Buckling Knockdown Factor Project, and she traveled to Delft, The Netherlands, for a research project with Prof. Chiara Bisagni. After a brief discussion with Prof. Bisagni and the principal investigator, Dr. Marc Schultz, she decided to enroll. NASA at the time was developing the Universal Stage Adapter and questions about the buckling behavior of more complex geometry arose. This inspired her to focus her research on the buckling behavior of conical-cylindrical shells. With the support of her family, friends, work supervisors, PhD advisors, and NASA scholarships, she was able to work full time as a structural analyst and have two children (2018 and 2020) while pursing her PhD. She has been recognized for her research contributions by receiving the 2024 Lockheed Martin Student Paper Award at the AIAA SciTech Conference and the NASA Marshall Space Flight Center Innovation Award (2025). Her plans are to continue working for NASA and continue doing research and development.

LIST OF PUBLICATIONS

1. **Rudd M.T., Eberlein D.J., Waters W.A., Gardner N.W., Schultz M.R., Bisagni C.**, *Analysis and validation of a scaled, launch-vehicle-like composite cylinder under axial compression*, Composite Structures, vol. 304, pt.1, pp.116393, 2023.
2. **Rudd M.T., Schultz M.R., Gardner N.W., Kosztowny C.J.R., Bisagni C.**, *Analysis and testing of a launch-vehicle-like composite conical-cylindrical shell*, AIAA Scitech 2023 Forum, January 23 - 27, National Harbor, MD, paper no. 2023-1525, 2023.
3. **Rudd M.T., Schultz M.R., Bisagni, C.**, *Buckling behavior of conical-cylindrical shells and design considerations for launch-vehicle applications*, AIAA Scitech 2024 Forum, January 8 - 12, Orlando, FL, paper no. 0034, 2024.
4. **Rudd M.T., Schultz M.R., Gardner N.W., Kosztowny C.J.R., Bisagni C.**, *Analysis and testing of a launch-vehicle-like composite conical-cylindrical shell*, AIAA Journal, vol. 62, no.9, pp.3526-3543, 2024.
5. **Rudd M.T., Schultz M.R., Gardner N.W., Kosztowny C.J.R., Bisagni C.**, *Experimental validation of the buckling behavior of unreinforced and reinforced composite conical-cylindrical shells for launch-vehicles*, Composite Structures, Volumes 349–350, 2024.
6. **Rudd M.T., Turteltaub S., Schultz M.R., Bisagni C.**, *Design sensitivity analysis of buckling in conical-cylindrical shells using polynomial chaos expansion*, to be submitted.